Title
Novel Quantitative Analyses in Mouse Models of Neurological and Psychiatric Disorders

Author
Chen, Lingxuan

Publication Date
2017

Peer reviewed|Thesis/dissertation

UNIVERSITY OF CALIFORNIA

Los Angeles

Novel Quantitative Analyses in Mouse Models of Neurological and Psychiatric Disorders

A dissertation submitted in partial satisfaction of the requirements for the degree Doctor of Philosophy in Molecular, Cellular, and Integrative Physiology

by

Lingxuan Chen

2018

ABSTRACT OF THE DISSERTATION

Novel Quantitative Analyses in Mouse Models of
Neurological and Psychiatric Disorders

by

Lingxuan Chen

Doctor of Philosophy in Molecular, Cellular, and Integrative Physiology
University of California, Los Angeles, 2018
Professor Istvan Mody, Chair

Numerous efforts have been made to illuminate the mechanisms underlying neurological and psychiatric disorders, in order to develop treatments for these diseases. With the advantage of transgenic mouse models to recapitulate human pathological alterations and to support drug screening, promising discoveries have been made over the past century. In this dissertation, I am focusing on Alzheimer's disease (AD), which is a neurodegenerative disorder with significant public health concern. Using one of the newest mouse models of AD, the *App*$^{NL-F}$ mouse model, I have investigated synaptic, network, and cognitive alterations related to this disease, with techniques from *in vitro* and *in vivo* electrophysiology for examining abnormalities in the brain to behavior tests for assessing the cognitive functions of the animals. In the meantime, novel quantitative approaches have been developed and applied to objectively interpret the experimental data. In *App*$^{NL-F}$ homozygous mice, we have found synaptic alterations consistent

with deficits in parvalbumin-expressing interneurons (PV INs). Moreover, through long-term *in vivo* local field potential (LFP) recording, we have discovered perturbed network activities associated with disrupted sleep patterns, which happened during a critical period in the disease progression and may lead to further cognitive deficits in these animals.

Besides well-known cognitive dysfunctions such as loss of memory and reasoning as well as language difficulties, there is a second group of non-cognitive symptoms including psychiatric disorders and behavioral disturbances, such as depression, hallucination, delusions, and agitations(Burns et al., 1990; Burns and Iliffe, 2009). Therefore, I have also investigated into the mouse forced-swim test (FST), which is widely used in the screening of antidepressants. By quantitative analyses on this test, we have discovered a new confounding factor, and developed novel methods to determine the important parameters in the mouse FST, which could be applied to mouse AD models to study depression and the effect of antidepressants in AD.

In conclusion, the application of quantitative approaches in neuroscience studies have led to the discovery of intriguing results and provided ground for exciting future research.

The dissertation of Lingxuan Chen is approved.

Carolyn R. Houser

Felix Erich Schweizer

Alcino Jose Silva

Istvan Mody, Committee Chair

University of California, Los Angeles

2018

CONTENTS

ACKNOWLEDGEMENTS

Spending the past few years in UCLA has been an amazing adventure and extraordinary experience for me. There are many people that have helped and inspired me and I would like to thank them for making this journey so memorable and enjoyable.

My sincere gratitude goes to my mentor, Dr. Istvan Mody, for leading me into the world of neurology. Istvan has been inspiring me constantly with his curiosity and sharp mind in scientific research, and his rigorous attitude will keep reminding me to think critically and stay true to the data. I am also grateful for him always supporting my ideas while providing valuable insights and suggestions. He is always open-minded about new methods and techniques, which has brought intriguing projects into the lab. Moreover, Istvan is a person with a great passion for life, which has made me believe that one can enjoy every aspect in his life while making wonderful achievements in his career.

I would like to thank my fellow lab members with whom I have crossed path with over the years. Dr. Guido Faas, for his constant support from tackling technical issues to helpful discussions providing brilliant new ideas since I joined the lab. Dr. Isabella Ferando, for showing me so many techniques essential for my projects and selflessly sharing her opinions and insights on my experimental results. Dr. Ryan Jones, for his instructions and help in electrophysiology when I first started patching. Dr. Xiaofei Wei, for sharing her expertise in patch-clamp recording. Laurel Ormiston and Sophia Angelides, for helping me with mouse behavior tests. I would also like to thank Dr. Albert Barth, Dr. Scott Arno, Dr. Sophia Vrontou, and Dr. Nadia Cusini for being a valuable part of my graduate life in the lab. Last but not least, my gratitude and memories go

to Reyes Main Lazaro, whose expertise in mouse breeding has been a great help for my projects, and his optimistic spirit in work will always inspire me.

I would like to thank the Molecular, Cellular, and Integrative Physiology interdepartmental Ph.D. program in UCLA, in particular Dr. James Tidball and Dr. Mark Frye for organizing this wonderful graduate program and providing a supportive environment for the students. I also want to thank the student affairs officers Michael Carr and Yesenia Rayos for their excellent work in being there whenever we need assistance.

I would like to acknowledge the Cross-disciplinary Scholars in Science and Technology (CSST) exchange program. This is the program that first brought me to UCLA 7 years ago when I was an undergraduate student and made me fall in love with this university and this city. Especially I want to thank Dr. Ren Sun for initiating this amazing program and for his effort in keeping us as a big family through all these years.

I would like to thank my committee members Dr. Carolyn Houser, Dr. Felix Schweizer, and Dr. Alcino Silva for providing valuable inputs to this dissertation.

Lastly I would like to thank my friends and family, without whom none of this would be possible. My dear friends Shan Huang, Luyao Xu, Huan Yang, Lili Feng, Ying Wang, Tongzhou Xu, and so many others, we have shared every happy and sad moment in all parts of our life in UCLA, and we have encouraged each other through these years and you guys are like family to me already. My parents, you have always been my role models no matter in life or in work from my childhood to now. Your everlasting love, support, and encouragement have been so important for me to conquer every difficulty. And lastly, my husband Zhiping, you are my best friend and the perfect companion. Your wisdom and passion for neuroscience has been a constant

inspiration to me, and you are the one who always trust me in pursuing a career in academia. I am so glad that we have shared so many important moments in our life. I love you.

Chapter III is a version of a manuscript under review: Chen L, Saito T, Saido TC, Mody I. Synaptic alterations consistent with parvalbumin-expressing interneuron dysfunction in a knock-in mouse model of Alzheimer's disease.

Chapter V is a reprint of the publication: Chen L, Faas GC, Ferando I, Mody I (2015) Novel insights into the behavioral analysis of mice subjected to the forced-swim test. Thansl Psychiatry 5: e551.

VITA

2007	B.E., Biomedical Engineering Zhejiang University, Hangzhou, China
2011-2017	Graduate Student Researcher Molecular, Cellular, and Integrative Physiology Interdepartmental Ph.D. Program, UCLA
2011-2015	China Scholarship Council Scholarship for Overseas Graduate Students
2012/2013/2014	Graduate Division Award
2013/2014	Teaching Assistant Physiological Science, UCLA
2014	Superior poster presentation by an MCIP student
2015	Graduate Programs in Bioscience Fellowship Incentive Program

PUBLICATIONS AND PRESENTATIONS

1. Chen L, Faas GC, Ferando I, Mody I (2015) Novel insights into the behavioral analysis of mice subjected to the forced-swim test. Transl. Psychiatry 5, e551. https://www.nature.com/articles/tp201544

2. Chen L, Ferando I, Mody I, Faas GC. Ducks float, but are they depressed? Buoyancy as a confounding factor in the mouse forced swim (Porsolt) test. Program No. 781.02. 2013 Neuroscience Meeting Planner. San Diego, CA: Society for Neuroscience, 2013. Online.

3. Chen L, Saito T, Saido TC, Mody I. Synaptic alterations consistent with parvalbumin-expressing interneuron dysfunction in a novel mouse model of Alzheimer's disease. Program No. 412.12. 2016 Neuroscience Meeting Planner. San Diego, CA: Society for Neuroscience, 2016. Online.

Chapter I

Introduction

Alzheimer's disease was discovered over a century ago, and it has drawn the attention of numerous studies trying to illuminate the mechanisms underlying this disease and to develop treatments. Especially, with the advantage of different mouse models to recapitulate human pathology, promising discoveries have been made in our fundamental knowledge of alterations from molecular and cellular to network functions in the AD brain. In this dissertation, I have investigated into a newly generated mouse model of AD, the App^{NL-F} model. With techniques from *in vitro* and *in vivo* electrophysiology for examining abnormalities in the brain to behavior tests for assessing the cognitive functions of the animals, a number of quantitative approaches have been developed to objectively interpret the experimental data, which have uncovered intriguing results and provided ground for future research as well. Also, novel quantitative approaches have been applied to the mouse forced-swim test (FST), which is widely used in major depressive disorder (MDD) research. FST with rigorous quantitative analyses could be useful in AD research as well with depression being one of the non-cognitive symptoms in AD.

1.1 Synaptic, network, and cognitive deficits in a mouse model of Alzheimer's disease

Alzheimer's disease (AD) is a progressive chronic neurodegenerative disorder that has become a compelling global burden of disease with the gradually aging population. Since it was

described in 1907 by Dr. Alois Alzheimer, AD has attracted efforts in both fundamental research trying to elucidate the molecular and cellular mechanisms of the disease and clinical studies aiming to treat or even cure this disorder, especially after the 1960s(Blessed et al., 1968; Katzman, 1976). Various gene mutations in the amyloid precursor protein (APP)(Levy et al., 1990) and presenilin (PSEN1 and PSEN2)(Levy-lahad et al., 1995; Rogaev et al., 1995; Sherrington et al., 1995) have been associated with early-onset familial AD (fAD), while apolipoprotein E polymorphism ε4 (APOE4) has been identified as a risk factor for late-onset sporadic AD(Schmechel et al., 1993; Strittmatter et al., 1993). The discovery of various genetic mutations has shed light upon the development of various AD mouse models. Another huge improvement was the isolation of amyloid β (Aβ) protein as the main component of amyloid plaques(Glenner and Wong, 1984a, 1984b) and the identification of the microtubule-associated protein tau as the principal constituent of neurofibrillary tangles (NFTs)(Grundke-Iqbal et al., 1986; Kosik et al., 1986; Wood et al., 1986). Now it is well known that AD pathology can be characterized by the accumulation of extracellular Aβ plaques, intracellular NFTs, as well as reactive microgliosis, dystrophic neurites, and loss of neurons and synapses(Braak and Braak, 1991; Serrano-Pozo et al., 2011).

Among various mouse models available for AD research(LaFerla and Green, 2012; Sasaguri et al., 2017), we have chosen the *App*$^{NL-F}$ model(Nilsson et al., 2014; Saito et al., 2014), which belongs to the 2nd generation mouse models of AD. Both generations of models develop excessive amyloid plaque deposition due to enhanced Aβ production. The main difference between the two generations of mouse AD models is that the 1st generation was generated by overexpressing either wild-type or mutant human APP (hAPP) in the mouse brain, which may cause intrinsic problems because of the overproduction of hAPP and its various cleavage products as well as the expression of powerful exogenous promoters. On the contrary, the 2nd generation mouse models were generated by a gene knock in approach, in which there is no

hAPP overexpression, thus reducing artificial phenotypes(Saito et al., 2014; Sasaguri et al., 2017). Therefore, it is essential to examine the pathological changes in the new models in order to untangle the individual contribution of Aβ to the disease progression.

The first part (Chapters II-IV) of this dissertation is focused on investigations into synaptic, network, and cognitive alterations in the *App*$^{NL-F}$ mouse model of AD. Chapter II is a qualitative description of the plaque load in the AD brain, as well as a quantitative study on the behavioral alterations in the animals using a newly developed behavior test. Chapter III comprises the studies on the synaptic transmission in layer 2/3 parietal cortex by patch-clamp recordings in the pyramidal cells. With rigorous analyses on the postsynaptic currents and the excitation-inhibition balance, we have found potential deficits in the parvalbumin-expressing interneurons (PV INs), which could then lead to aberrant network activities and memory decline. Chapter IV describes the investigations into the network activities from long-term *in vivo* local field potential (LFP) recordings in hippocampal CA1 stratum pyramidale at different ages in the NL-F mice. We have discovered a possibly critical period in the disease progression, when sleep disturbances were observed and sharp wave ripples (SWRs) started to turn into spike discharges, which could lead to further clinical changes in AD such as seizures and cognitive impairment.

1.2 Quantitative analyses on the behavior of mice subjected to the forced-swim test

Major depressive disorder (MDD) is a key public health concern. From 1990 to 2010, the contribution of MDD to both disability-adjusted life years(Murray et al., 2012) and years lived with disability(Vos et al. 2012) had increased by 37%. MDD was predicted to become the second leading contributor to the burden of disease by 2020(Murray and Lopez, 1997).

Moreover, depression belongs to one of the non-cognitive symptoms in AD(Burns et al., 1990; Burns and Iliffe, 2009), making studies on MDD relevant to AD research as well.

Since clinical depression is a heterogeneous disease in humans, with symptoms at the psychological, behavioral, and physiological levels, it is difficult to model all aspects of this disease in rodents, especially the psychological ones(Cryan et al., 2002; Cryan and Mombereau, 2004). A review by McKinney and Bunney on animal models of depression has listed several minimum requirements for a model system, including that there should be observable behavioral changes that can be objectively evaluated, the changes in the animals should be reversible by the treatment effective in humans, and the results should be reproducible among different investigators(McKinney and Bunney, 1969). Therefore, a practical strategy in developing animal models for behavioral depression would be to model single changes with a clear cut output relevant to the disease state rather than recapitulating the entire syndrome. The forced-swim test (FST) was developed for rats by Porsolt et al. in 1977(Porsolt et al., 1977a, 1977b, 1978), and it is the most widely used rodent model to assess the effectiveness of antidepressants because of it's operational ease, reliability, and sensitivity to a broad spectrum of drugs. The output in FST is the immobility of the rat, which is defined as when a rat is floating and/or making only necessary movements to keep the balance of its body or to keep its head above the water. If treatment with a drug reduced behavioral immobility, which is thought of as a measure of behavioral despair, the drug could be considered as an effective antidepressant(Porsolt et al., 1977a, 1977b, 1978). Latency to the first immobility is also used as an output of the test(Castagné et al., 2009).

As the FST was originally developed for rats, a species ethologically different from mice, some technical issues remain in FST using mice, a species for which the test may not be adequately adapted(Cryan and Mombereau, 2004; Cryan and Holmes, 2005). The second part (Chapter V)

of this dissertation is on investigations into possible pitfalls in the measurements currently used for FST in mice, uncovering a previously neglected confounding factor, the buoyancy of the animals, and devising novel quantitative analyses on the behavior of the animals during the test. Our systematic analyses indicated the existence of an intrinsic biological clock influencing the swimming patterns of the animals, providing possibilities for future studies. Also, FST with rigorous analyses could be applied to AD research, such as evaluating the role of depression and antidepressants in AD pathology.

Bibliography

Blessed G, Tomlinson BE, Roth M (1968) The Association Between Quantitative Measures of Dementia and of Senile Change in the Cerebral Grey Matter of Elderly Subjects. Br J Psychiatry 114:797–811.

Braak H, Braak E (1991) Demonstration of Amyloid Deposits and Neurofibrillary Changes in Whole Brain Sections. Brain Pathol 1:213–216.

Castagné V, Porsolt RD, Moser P (2009) Use of latency to immobility improves detection of antidepressant-like activity in the behavioral despair test in the mouse. Eur J Pharmacol 616:128–133.

Cryan J, Markou A, Lucki I (2002) Assessing antidepressant activity in rodents: recent developments and future needs. Trends Pharmacol Sci 6147:238–245.

Cryan JF, Holmes A (2005) The ascent of mouse: advances in modelling human depression and anxiety. Nat Rev Drug Discov 4:775–790.

Cryan JF, Mombereau C (2004) In search of a depressed mouse: utility of models for studying depression-related behavior in genetically modified mice. Mol Psychiatry 9:326–357.

Glenner GG, Wong CW (1984a) Alzheimer's disease: Initial report of the purification and characterization of a novel cerebrovascular amyloid protein. Biochem Biophys Res Commun 120:885–890.

Glenner GG, Wong CW (1984b) Alzheimer's disease and Down's syndrome: Sharing of a unique cerebrovascular amyloid fibril protein. Biochem Biophys Res Commun 122:1131–1135.

Grundke-Iqbal I, Iqbal K, Quinlan M, Tung YC, Zaidi MS, Wisniewski HM (1986) Microtubule-associated protein tau. A component of Alzheimer paired helical filaments. J Biol Chem 261:6084–6089.

Katzman R (1976) The Prevalence and Malignancy of Alzheimer Disease. Arch Neurol 33:217.

Kosik KS, Joachim CL, Selkoe DJ (1986) Microtubule-associated protein tau (tau) is a major antigenic component of paired helical filaments in Alzheimer disease. Proc Natl Acad Sci U S A 83:4044–4048.

LaFerla FM, Green KN (2012) Animal models of Alzheimer disease. Cold Spring Harb Perspect Med 2:a006320-.

Levy-lahad E, Wasco W, Poorkaj P, Romano DM, Oshima J, Pettingell WH, Yu C, Jondro PD, Schmidt SD, Wang K, Crowley AC, Fu Y, Guenette SY, Galas D, Nemens E, Wijsman EM, Bird TD, Schellenberg GD, Tanzi RE (1995) Candidate Gene for the Chromosome 1 Familial Alzheimer's Disease Locus. Science (80-) 269:973–977.

Levy E, Carman MD, Fernandez-Madrid IJ, Power MD, Lieberburg I, van Duinen SG, Th M Bots GA, Luyendijk W (1990) Mutation of the Alzheimer's Disease Amyloid Gene in Hereditary Cerebral Hemorrhage, Dutch Type. Frangione Source Sci New Ser 248:1124–1126.

McKinney WT, Bunney WE (1969) Animal Model of Depression. Arch Gen Psychiatry 21:240–248.

Murray C, Lopez A (1997) Alternative projections of mortality and disability by cause 1990–2020: Global Burden of Disease Stud y. Lancet 349:1498–1504.

Murray CJL et al. (2012) Disability-adjusted life years (DALYs) for 291 diseases and injuries in 21 regions, 1990-2010: a systematic analysis for the Global Burden of Disease Study 2010. Lancet 380:2197–2223.

Nilsson P, Saito T, Saido TC (2014) New mouse model of Alzheimer's. ACS Chem Neurosci 5:499–502.

Porsolt RD, Anton G, Blavet N, Jalfre M (1978) Behavioural despair in rats: a new model sensitive to antidepressant treatments. Eur J Pharmacol 47:379–391.

Porsolt RD, Bertin A, Jalfre M (1977a) Behavioral despair in mice: a primary screening test for antidepressants. Arch Int Pharmacodyn Ther 229:327–336.

Porsolt RD, Le Pichon M, Jalfre M (1977b) Depression: a new animal model sensitive to

antidepressant treatments. Nature 266:730–732.

Rogaev EI et al. (1995) Familial Alzheimer's disease in kindreds with missense mutations in a gene on chromosome 1 related to the Alzheimer's disease type 3 gene. Nature 376:775–778.

Saito T, Matsuba Y, Mihira N, Takano J, Nilsson P, Itohara S, Iwata N, Saido TC (2014) Single App knock-in mouse models of Alzheimer's disease. Nat Neurosci 17:661–663.

Sasaguri H, Nilsson P, Hashimoto S, Nagata K, Saito T, De Strooper B, Hardy J, Vassar R, Winblad B, Saido TC (2017) APP mouse models for Alzheimer's disease preclinical studies. EMBO J 36:e201797397.

Schmechel DE, Saunders AM, Strittmatter WJ, CRAINtt BJ, HULETTEt CM, Joo SH, Pericaknvance MA, Goldgaberii D, Roses AD (1993) Increased amyloid β-peptide deposition in cerebral cortex as a consequence of apolipoprotein E genotype in late-onset Alzheimer disease. Neurobiology 90:9649–9653.

Serrano-Pozo A, Frosch MP, Masliah E, Hyman BT (2011) Neuropathological alterations in Alzheimer disease. Cold Spring Harb Perspect Med 1:a006189.

Sherrington R et al. (1995) Cloning of a gene bearing missense mutations in early-onset familial Alzheimer's disease. Nature 375:754–760.

Strittmatter WJ, Saunders AM, Schmechel D, Pericak-vance M, Enghild J, Salvesen GS, Roses AD (1993) Apolipoprotein E: High-avidity binding to ,B-amyloid and increased frequency of type 4 allele in late-onset familial Alzheimer disease. Med Sci Commun by William J Lennarz 90:1977–1981.

Vos T et al. (2012) Years lived with disability (YLDs) for 1160 sequelae of 289 diseases and injuries 1990-2010: a systematic analysis for the Global Burden of Disease Study 2010. Lancet 380:2163–2196.

Wood JG, Mirrat SS, Pollock NJ, Bindert LI, Krause RM (1986) Neurofibrillary tangles of Alzheimer disease share antigenic determinants with the axonal microtubule-associated

protein tau. Med Sci 83:4040–4043.

Chapter II

Amyloid Deposition and Behavioral Alterations in the *App*$^{NL-F}$ Mouse Model of AD

2.1 Summary

Alzheimer's disease (AD) is a neurodegenerative disease that has become a global public health concern in the gradually aging population. The pathological hallmarks of AD include amyloid-β peptide (Aβ) plaques, neurofibrillary tangles (NFTs), and neuronal loss. Specifically, various mouse models generated by known mutations causing the overproduction of Aβ in human familial AD have been generated, accelerating research in fundamental mechanisms leading to this disease and subsequent alterations in the brain causing pathologic phenotypes such as cognitive dysfunction. The *App*$^{NL-F}$ mouse model of AD is newly generated by a gene knock-in approach, and compared to other existing transgenic mouse models of AD it closely replicates several key pathologies found in human AD while having fewer physiological disturbances and artificial phenotypes. Here two of the key pathological hallmarks in the *App*$^{NL-F}$ model are presented, Aβ plaque deposition in the brain and cognitive deficits, using methods of tissue clearing and a novel behavior test combining novel object recognition (NOR), social interaction, and olfactory memory. Our studies on the level of amyloidosis provided guidance in choosing mice at appropriate ages to study synaptic transmission, network activities, as well as cognitive functions, and results from our novel behavior test revealed moderate yet previously neglected cognitive and perceptual deficits in the AD mice.

2.2 Introduction

2.2.1 Alzheimer's disease

Alzheimer's disease (AD) is a progressive chronic neurodegenerative disease that has become a compelling global burden of disease with the gradually aging population. According to the World Health Organization (WHO) fact sheet on dementia updated on September 2017, around 47 million people have dementia worldwide with 10 million new cases each year, and AD is the most common cause of dementia, contributing to about 60-70% of all dementia cases. According to epidemiological studies in many regions, there are 4.6 million of new AD cases each year, and the frequency is expected to double every 20 years until 2040(Ferri et al., 2005; Mayeux and Stern, 2012). Patients developing AD suffer from three major groups of symptoms(Burns and Iliffe, 2009). The first group is cognitive dysfunction, including loss of memory, reasoning and abstraction, as well as language difficulties. The second group consists of psychiatric disorders and behavioral disturbances, collectively termed as non-cognitive symptoms, such as depression, hallucination, delusions, agitations, etc.(Burns et al., 1990). The third group denotes compromises in performing daily activities.

AD was discovered in 1907 by Dr. Alois Alzheimer; however, for the first 60 years after its discovery, virtually no progress was made in our understanding of the causes and mechanisms of this disorder. After the 1960s, AD has attracted the attention of both fundamental research trying to elucidate the molecular and cellular mechanisms of the disease and clinical studies aiming to treat or even cure the disorder. A 1968 study by Blessed *et al*. supported the idea that AD occurred along an age continuum(Blessed et al., 1968). In 1976, Robert Katzman warned about an impending epidemic of cases with the aging population especially in developed countries(Katzman, 1976). In 1979, Jerome Stone and others with affected family members organized the Alzheimer's Association, providing a huge boost for the public recognition and

awareness of this disease as well its personal and social burden. In the area of biochemical research for the cause of AD, in 1984, amyloid-β protein was isolated and characterized post mortem from patients with AD or Down syndrome(Glenner and Wong, 1984a, 1984b). Then the microtubule-associated protein, tau, was identified by several groups as the principal constituent of neurofibrillary tangles (NFTs)(Grundke-Iqbal et al., 1986; Kosik et al., 1986; Wood et al., 1986). It is now well-known that AD pathology is characterized by extracellular neuritic amyloid plaques and intracellular neurofibrillary tangles (NFTs), as well as reactive microgliosis, dystrophic neurites, and loss of neurons and synapses(Braak and Braak, 1991; Serrano-Pozo et al., 2011).

Various efforts have been made to study the fundamental mechanisms leading to the pathology found in AD(Bateman et al., 2011; Selkoe et al., 2012), yet there is still no cure for this devastating disease. A key molecule in AD is amyloid-β (Aβ), which is a 40 (Aβ40) or 42 (Aβ42) amino acid peptide derived from the amyloid precursor protein (APP) after its sequential cleavage by β- and γ-secretases. In a normal brain, the majority of Aβ produced is the shorter version, Aβ40(Younkin, 1998). About 5-15% of total Aβ is Aβ42, and a small portion of other longer or shorter versions of Aβs may be observed(Findeis, 2007). Extracellular Aβ levels need to be regulated within a tight window to sustain normal synaptic functions(Puzzo et al., 2008); on the other hand, Aβ levels are likely to be regulated by synaptic activity(Kamenetz et al., 2003; Cirrito et al., 2005). In AD, Aβ can form intermediate soluble oligomers that are synaptotoxic, or insoluble β-sheet amyloid fibrils that are the main component of dense-core plaques(Serrano-Pozo et al., 2011). Particularly, Aβ42 is more prone to aggregation than Aβ40, leading to earlier and more severe cognitive impairment(Findeis, 2007). The excessive accumulation of pathological Aβ plaques seems to have a causal relationship with AD(Glenner and Wong, 1984b; Walsh and Selkoe, 2004; Tanzi and Bertram, 2005). Clinicopathological correlation studies have established that Aβ plaques accumulation occurs primarily before the

onset of cognitive deficits, while NFTs and neuronal/synapse loss parallel the progression of cognitive decline(Serrano-Pozo et al., 2011). Recent studies in mouse models of AD have also pointed out the possibility that Aβ may be part of the mechanism altering neuronal, synaptic, and network activity, leading to compromised cognitive functions in the animals(Palop et al., 2007, 2011; Palop and Mucke, 2010; Mucke and Selkoe, 2012; Yan et al., 2012).

2.2.2 Mouse models of AD

The vast majority (more than 99%) of AD cases are sporadic AD (sAD)(Campion et al., 1999); unfortunately the underlying causes of these cases remain largely unknown. On the contrary, several gene mutations have been linked to early-onset familial AD (fAD)(Tanzi and Bertram, 2005). In 1990, the first pathogenic mutation was discovered in the *APP* gene exons 16 and 17, encoding the Aβ domain(Levy et al., 1990). With additional mutations subsequently found in *APP*, researchers found that *APP* mutations only account for a small fraction of all fAD cases. Further efforts have been put to identifying other genes connected to fAD, and in 1995, presenilin 1 and 2 (*PSEN1* and *PSEN2*), crucial components of the γ-secretase, were reported as fAD genes on chromosomes 14 and 1, respectively(Levy-lahad et al., 1995; Rogaev et al., 1995; Sherrington et al., 1995). Together, *APP* and *PSEN1/2* mutations are responsible for 30 to 50% of autosomal-dominant AD cases, and about 0.5% of AD in general(Cruts et al., 2012). So far, a total of 51 autosomal-dominant mutations have been found in *APP*, 219 in *PSEN1*, and 16 in *PSEN2*(Cruts et al., 2012). In cases of late-onset sAD, a common polymorphism, ε4, in the apolipoprotein E gene (*APOE*) on chromosome 19 was identified to be a risk factor for sAD(Schmechel et al., 1993; Strittmatter et al., 1993) and contributing to about 20% of the cases(Cruts et al., 2012).

Although known mutations are a rare cause for AD, they are important for pre-symptomatic diagnostics of patients that might be affected by fAD, as well as for the progress in understanding the mechanisms of AD. Also, the neuropathology and clinical phenotypes are generally indistinguishable between the familial and sporadic form of AD, with the biggest difference being the age of onset(Selkoe and Podlisny, 2002; Bateman et al., 2011). Therefore, mouse models rely on genetic mutations associated with fAD because these mutations have known pathological consequences also believed to underlie the more prevalent sAD. Although no single mouse model recapitulates all aspects the disease, each one allows in-depth study of one or two components, which presently is not possible with human patients or samples. These various mouse models simulate several key aspects of human AD, including accumulation of Aβ plaques, synaptic and network alterations, gliosis, deficits in learning and memory, and other behavioral abnormalities(Games et al., 1995; Hsiao et al., 1996; Sturchler-Pierrat et al., 1997; Palop et al., 2003, 2005, 2007; Götz et al., 2004; Cheng et al., 2007; Cissé et al., 2011; Verret et al., 2012).

Most of the studies used transgenic mouse models that overproduce mutant or wild type human APP (hAPP). While they do develop pathology that is similar to that found in human brain, hAPP-overexpressing mice may contain intrinsic problems that may induce artificial phenotypes(Nilsson et al., 2014; Saito et al., 2014): in these animals, not only Aβ but also other APP fragments are overproduced, which may disrupt intrinsic biological functions. The utilization of artificial promoters results in transgene expression in cells not necessarily identical to those expressing endogenous APP. Another sign of perturbed physiology in the APP overexpressing models is the sudden death often observed in the hAPP transgenic mice(Nilsson et al., 2014; Saito et al., 2014). Endogenous APP regulates multiple stages of cortical development as well as electrical activity in the adult brain(Priller et al., 2006; Young-Pearse et al., 2007; Zheng and Koo, 2011; Hoe et al., 2012). APP knockout (KO) mice are viable and fertile, but they do exhibit

some differences from normal mice, including lower weight, reduced locomotor activity, decreased long-term potentiation (LTP), and eventually reactive gliosis in their brains(Zheng et al., 1995). APP metabolites need to be regulated within a tight window to sustain normal synaptic functions(Puzzo et al., 2008). For example, low picomolar concentrations of a preparation containing both Aβ42 monomers and oligomers led to an increase of hippocampal long-term potentiation (LTP), while high nanomolar concentrations resulted in the well established reduction of LTP(Puzzo et al., 2008). Also, APP overexpression in mice may interfere with transport machinery in the cell(Nilsson et al., 2014). Taken all together, these drawbacks of existing mouse models of AD make it essential to develop new models that can replicate the pathology in human AD while having less perturbed physiology and fewer artificial phenotypes.

We have obtained the *App*$^{NL-F}$ mice from the research group led by Dr. Takaomi C. Saido at the Laboratory for Proteolytic Neuroscience, RIKEN Brain Science Institute, Saitama, Japan(Nilsson et al., 2014; Saito et al., 2014). This 2nd generation mouse model of AD was generated by manipulating the mouse *APP* gene using a knock-in strategy with Swedish (KM670/671NL)(Citron et al., 1992) and Beyreuther/Iberian (I716F)(Lichtenthaler et al., 1999; Guardia-Laguarta et al., 2010) mutations. The Swedish mutation elevates the total amount of Aβ40 and Aβ42; while the Beyreuther/Iberian mutation increases the ratio of Aβ42 to Aβ40. In addition, the Aβ sequence within the mouse *APP* gene was humanized(Saito et al., 2014) (**Fig. 2.1**). As a consequence, in contrast to hAPP overexpressing mouse models, the *App*$^{NL-F}$ mice have normal levels of full length APP and its cleavage products. Meanwhile, with the knock-in mutations, the *App*$^{NL-F}$ mice produced significantly higher level of Aβ42 compared to wild-type (WT) and hAPP-overexpressing mice, and the ratio of Aβ42/ Aβ40 was also significantly higher(Saito et al., 2014). The initial Aβ deposition detected in homozygous *App*$^{NL-F/NL-F}$ mice was at 6 months (Saito et al., 2014). Also, neuroinflammation and synaptic alterations were

observed in *App*$^{NL-F/NL-F}$ mice(Saito et al., 2014). On the behavioral level, the *App*$^{NL-F/NL-F}$ mice showed memory impairment in Y-maze test as early as 18 months(Saito et al., 2014).

Over 3000 papers have been published using the 1st generation hAPP overexpressing mouse models of AD. With the introduction of the *App*$^{NL-F/NL-F}$ model, it has become clear that many of these findings on disrupted phenotypes could be artifacts and are worth reevaluation(Saito et al., 2016; Sasaguri et al., 2017). For example, the calpain activation in 5XFAD mice with APP and presenilin (PS) mutations(Oakley et al., 2006; Seo et al., 2014) was not observed in *App*$^{NL-F/NL-F}$ mice(Saito et al., 2016). In the same 2016 paper from Saito *et al*., Nav1.1 sodium channel downregulation in parvalbumin interneurons (PV INs) found in hAPPJ20 mice(Verret et al., 2012) was not observed in *App*$^{NL-F/NL-F}$ mice either, because Nav1.1 may be a substrate of calpain(Ebensperger et al., 2005). In conclusion, compared to the 1st generation mouse models of AD, the novel *App*$^{NL-F}$ model has no artificial phenotypes resulting from overloading the mouse brain with hAPP and the introduction of powerful exogenous promoters. Therefore, utilization of this new model will advance our understanding of AD pathology caused by mutations in the *App* gene.

2.2.3 Behavior tests for APP KI mouse models of AD models

So far, there are already several lines of 2nd generation models, including the *App*$^{NL-F/NL-F}$ model with Swedish and Beyreuther/Iberian mutations, as well as the APP$^{NL-G-F/NL-G-F}$ model with an extra Arctic mutation and the APP$^{NL/NL}$ model that only has the Swedish mutation. The APP$^{NL/NL}$ model was used as a control for the other two models in behavior tests, because with the Swedish mutation facilitating β cleavage of APP, there were higher levels of C-terminus fragment β (CTF-β) in both the *App*$^{NL-F/NL-F}$ and the *App*$^{NL-G-F/NL-G-F}$ models(Saito et al., 2014), and extremely high levels of CTF-β in hAPP-overexpressing mice may affect the cognitive

function(Mitani et al., 2012). The NL model has the same amount of CTF-β as the NL-F and the NL-G-F models, and mice were normal in a Y-maze test, while *App*$^{NL\text{-}F/NL\text{-}F}$ and *App*$^{NL\text{-}G\text{-}F/NL\text{-}G\text{-}F}$ mice showed impairment at 18 months and 6 months, respectively, meaning that the CTF-β level in these models did not disturb the cognitive phenotypes(Saito et al., 2014). Another limitation for behavioral studies in hAPP models is that the overexpression of APP might induce behavioral abnormalities prior to Aβ pathology, while in humans Aβ pathology arises much earlier than overt disease onset(Hsiao et al., 1996; Mucke et al., 2000).

Although dementia is the main clinical hallmark of AD, a broad spectrum of cognitive functions are also affected in AD patients, such as attention and executive functions(Perry and Hodges, 1999; Lindeboom and Weinstein, 2004; Ossenkoppele et al., 2015). Similarly, a range of behavior tests could be done in the NL-F mice. Besides the Y-maze test mentioned above, which monitored the spontaneous alteration behavior of mice as a measure of memory performance(Saito et al., 2014), there was also a battery of tests analyzed using an automated home-cage monitoring system in NL-F and NL-G-F mice of different ages(Masuda et al., 2016). While NL-G-F mice exhibited clear deficits in spatial memory, flexible learning, and attention performance as well as enhanced compulsive behavior, the NL-F mice only showed modest abnormalities, suggesting the role of the Arctic mutation in cognitive deficits. In the meantime, the NL-G-F mice had more rapid accumulation of Aβ deposits and glial responses(Masuda et al., 2016). Another study on the cognitive deficits in the NL-G-F model showed no abnormalities in the Y-maze, the novel object recognition (NOR), or the Morris water maze (MWM) tests compared to WT, yet there was a reduction in locomotion/exploratory activity in an open field (OF) test in these APP-KI mice(Whyte et al., 2018).

Since the number of studies characterizing the behavioral phenotypes in the *App*$^{NL\text{-}F}$ model is limited and the results are still ambiguous, we have decided to perform a behavior test on the

App^{NL-F} mice. We have designed a test that combines the NOR test, social interaction, and olfactory memory (see **Method** for details), in order to incorporate different cognitive functions into one test. The NOR test is used to assess recognition memory in mice that is based on the spontaneous tendency of rodents to explore a novel object longer than a familiar one(Antunes and Biala, 2012), and the hippocampus is important for recognition memory formation in both animals and humans(Barker and Warburton, 2011). It has been shown that the NOR test is a facile test for drug screening in APP/PS1 mice(Zhang et al., 2012). We have replaced the novel and familiar objects in the NOR test with novel and familiar mice, thus adding social interaction into consideration. The familiarity of experimental mice with the familiar mouse was established by olfactory memory using interconnected cages (see **Method**). Perceptual disorders are common in AD patients, including deficits in olfactory(Doty, 1991; Nordin et al., 1995; Murphy, 1999; McCaffrey et al., 2000), visual(Cronin-Golomb et al., 1991), and auditory(Cacace, 2007) perceptual abilities. Especially, the olfactory system has close associations with memory and emotion(Eichenbaum HB, Otto TA, Wible CG, 1991), and the olfactory bulb suffers from cell loss in AD, and the olfactory sensory pathway is pathologically affected in AD(Esiri and Wilcock, 1984). Therefore, adding olfactory recognition and related memory of the familiar mouse to this test may uncover cognitive and perceptual deficits in the *App*$^{NL-F}$ mice that were neglected before using traditional behavioral assays.

2.3 Materials and Methods

2.3.1 Animal use

All animal use was approved by the UCLA Chancellor's Committee on Animal Welfare. *App*$^{NL-F}$ mice were originally obtained from the research group led by Dr. Takaomi C. Saido at the Laboratory for Proteolytic Neuroscience, RIKEN Brain Science Institute, Saitama, Japan(Nilsson

et al., 2014; Saito et al., 2014). Wild type control mice (WT) were either aged littermates from the *App*$^{NL-F}$ mice breeding, or obtained from the National Institute on Aging. Mice were housed under the care of the Division of Laboratory Animal Medicine (DLAM) of University of California, Los Angeles (UCLA). Mice were maintained in a 12 h light/dark cycle with ad libitum access to food and water. All experiments were done during the light cycle.

2.3.2 Immunohistochemistry

Brain tissues were processed from 350 μm-thick acute brain slices used for electrophysiology recordings (see **Chapter III** for details) and then stored in 4% paraformaldehyde (PFA) overnight at 4°C. Brain slices were then cryoprotected in 30% sucrose solution in Millonig's modified PBS, frozen in optimal cutting temperature (O.C.T.) compound (Tissue-Tek, Sakura Finetek) and kept at -80°C. Thick slices were re-sectioned to 35 μm at -20°C by a cryostat, then kept in cyroprotectant solution (30% Ethylene Glycol, 30% Glycerol, 40% PBS) at -20°C until staining.

The steps and reagents used for diaminobenzidine (DAB) staining of Aβ are as follows: 30 min washing between steps with 1X Tris-buffered saline (TBS; pH 7.4); 30 min quenching of endogenous peroxidases with 1.5% H_2O_2 in TBS; 2 h blocking with 10% normal goat serum (NGS) with 0.3% Triton X-100 (Sigma) for permeabilization; overnight staining with 1:1000 primary antibody (Anti-human amyloid β Rabbit IgG, IBL 18584; or β-Amyloid D54D2 Rabbit mAb, Cell Signaling Technology #8243) in 1:50 NGS at room temperature; 2 h staining with 1:200 secondary antibody (biotinylated goat anti-rabbit IgG antibody, Vector Laboratories) in 1:30 NGS; 30 min signal amplification with VECTASTAIN Elite ABC-HRP kit (Vector Laboratories); Final signal development with the DAB Peroxidase (HRP) Substrate kit with Nickel (Vector Laboratories). Slices were then carefully mounted on Superfrost Plus microscope

slides (Fisher Scientific), completely dried and coverslipped with DPX Mountant for Histology (Sigma-Aldrich). Bright field imaging of DAB stains was done using a Leica DMLB microscope, and images were acquired with Stereo Investigator (MicroBrightField.Inc).

2.3.3 Tissue clearing and confocal microscopy

Tissue clearing was done following a previously published PACT protocol(Yang et al., 2014). Briefly, PFA-fixed tissues (350 μm brain slices) were incubated overnight at 4°C in A4P0 hydrogel monomer solution (4% acrylamide supplemented with 0.25% VA-044 in PBS). On the next day A4P0 infused samples were de-gassed with nitrogen in a 50 ml test tube and then incubated for 2-3 hours until the solution has fully polymerized. The samples were extracted from the embedding and washed briefly in PBS, then incubated in the clearing solution (8% SDS in PBS, pH 7.5) for 2-5 days in 37°C with shaking. They were then washed with 4-5 changes of PBS over 1 day. Immunofluorescence staining on Aβ plaques was done following tissue clearing, with steps similar to DAB staining described above with several adaptation for fluorescent staining: there was no quenching step, and 1:1000 secondary antibody (goat anti-rabbit IgG secondary antibody, Alexa Flour 488 or Alexa Flour 555, Invitrogen) was used for secondary staining. Lastly, after staining, the samples were incubated in RIMS(Yang et al., 2014) solution (RI 1.46) at room temperature until transparent, then mounted in WillCo-dish (WillCo Wells GWSB-5030) filled with RIMS right before imaging. Confocal SP5 Blue microscope in UCLA Advanced Light Microscopy & Spectroscopy (ALMS) was used for plaque imaging. 350 μm cleared coronal slices were imaged in the parietal cortex region. The thickness of confocal plane for the 10x dry objective used was 6.1 μm. The objective was moving with a specific step size (usually smaller than the thickness of confocal plane) from the upper surface of the slice to the other side, taking images at every step. Stacks of images were then loaded to and processed with ImageJ for z projections.

2.3.4 Behavior test

Four different groups of mice were subjected to the test: (1) Control male ($App^{wt/wt}$, N=14, age-matched with AD Male group); (2) AD male ($App^{NL\text{-}F/NL\text{-}F}$, N=14, age=11-21 m); (3) Control female ($App^{wt/wt}$, N=14, age-matched with AD Female group); (4) AD female ($App^{NL\text{-}F/NL\text{-}F}$, N=14, age=13-20 m). For all the statistical analysis, we only used data from WT mice as controls, excluding data from heterozygous mice. Therefore, the final number of animals for each group was N=13 for WT male, N=10 for WT female, and N=14 for AD male and female.

The general protocol for the behavior test we used is shown in **Figure 2.5a**. This test was designed based on a novel object recognition (NOR) test while combining social interaction and olfactory memory by using novel and familiar mice instead of objects (Ormiston et al., 2017).

Briefly, at day 1 each group of WT and AD mice (experimental mice) were odor paired with one mouse of the same gender, which was then referred to as the "familiar mouse". At day 2, the experimental mice were subjected to an open field test (5 min) in the same arena (0.9 m diameter) used for subsequent tests for habituation. On day 3-4 mice stayed odor-paired with the familiar mouse. Then on day 5 test 1 was performed, followed by day 6 in odor-paired cages. On day 7, all mice were unpaired, followed by test 2 on day 8. day 9-12 all mice stayed in unpaired cages, and lastly on day 13 test 3 was performed. All mice were brought into the behavior room with dim lighting at least 1 h before each test to familiarize with the room and reduce anxiety.

The olfactory pairing apparatus is shown in **Figure 2.5b**. Three customized cages were interconnected with tubes. In this way, only odor can pass through but animals in different cages could not physically interact with each other. The familiar mouse was housed in the middle cage while WT and AD mice were housed on the two side cages. The arena for the tests is shown in

Figure 2.5c. One “novel mouse” with the same gender was used for each test. The novel and familiar mice were placed inside two plastic cylindrical containers in the arena, and small openings on the containers enabled the interaction between the test animal and the novel/familiar mouse. There were also two different visual cues on the wall. Relative locations of the novel and familiar mouse as well as relative locations of the visual cues were randomized among tests. The test animals were allowed to freely explore the arena and interact with the novel and familiar mouse for 5 min. For the open field tests, no objects, novel/familiar mouse, or visual cues were placed into the arena except the experimental mouse, which was allowed to freely explore the environment for 5 min.

All tests were video recorded. The analysis on mouse behavior was done by using a customized program in Igor Pro 6 that automatically tracks the performance of the experimental mouse (Barth and Mody, 2014) (**Fig. 2.5d**). The program returns the instantaneous and average speed (mm/s), total distance traveled (m), percent time interacting with familiar and novel mouse, etc., with a time precision of 0.1 s. All statistical tests were done in Prism 6 using either non-parametric unaired t test (Mann-Whitney test) or non-parametric paired one-way ANOVA test (Friedman test). All the group statistics are presented as mean ± SEM (standard error of mean).

2.4 Results

2.4.1 Aβ plaques were abundant in aged App$^{NL\text{-}F/NL\text{-}F}$ mice only.

Since we want to examine the synaptic and network activity either before Aβ plaque deposition for early alterations or after for later pathological developments, using immunostaining we first established a qualitative description of the amount of plaques in *App$^{NL\text{-}F/NL\text{-}F}$* (AD Homo) and

App$^{NL-F/wt}$ (AD Het) mice. We were especially interested in the parietal cortex and the hippocampal CA1 region, because *in vitro* (patch-clamp) and *in vivo* (local field potential) electrophysiology was done in those areas (see Chapters III and IV), respectively.

From the DAB stains on Aβ plaques (**Fig. 2.2**), we found that in 8.3 m AD homo brain, there were still only few plaques in the cortex (**Fig. 2.2a**), and these plaques might still be diffuse plaques (**Fig. 2.2b, c** for enlarged images on plaques), but this finding needs further validation with Thioflavin-S or Congo Red stainings. Also, since the antibody we used (IBL 18584) reacts with the N-terminus of the Aβ peptide, we cannot tell which specific Aβ was the main component of these deposits. In 14 m AD homo brain, there was already very prominent plaque deposition in the cortex (where patch-clamp recordings were done on pyramidal cells to examine the synaptic transmission, see Chapter III) as well as the CA1 pyramidal cell layer (where in vivo recordings were performed to examine changes in network activities and sleep patterns, see Chapter IV) (**Fig. 2.2d**). Aβ deposits were also abundant in the stratum lacunosum/moleculare (str. lac/mol). Enlarged view on the plaques in the cortex (**Fig. 2.2e**) showed denser and larger plaque formation, which could be dense-core plaques, but again this should be further validated. In an *App*$^{NL-F/wt}$ mouse at 11.5 m of age, we did not observe any plaque deposition in 35 μm re-sectioned slices (**Fig. 2.2f**). We also did a side-by-side DAB staining on Aβ plaques in 31.5 m-old *App*$^{NL-F/NL-F}$ and age-matched (30 m) WT mice (**Fig. 2.3**), which further validated the specificity of the antibody performance since no staining was present in WT slices under the same staining procedure and condition. On the contrary, heavy deposition was observed in the cortex (**Fig. 2.3a**) and across different layers of the hippocampus (**Fig. 2.3c**) in the aged homozygous mouse brain, with fewer plaques seen in the hilus and granule cell layer while more in the outer strata.

In the DAB stains, re-sectioned slices were only 35 μm thick, which limited our visualization of the overall load of plaques in the brain. With the advantage of different tissue clearing techniques(Hama et al., 2011, 2015; Ertürk et al., 2012; Chung et al., 2013; Kuwajima et al., 2013; Susaki et al., 2014; Yang et al., 2014), one could transform intact tissue into an optically transparent and macromolecule-permeable state while preserving the cellular and subcellular structures within the tissue. Moreover, it is compatible with endogenous fluorescence protein expression as well as immunohistochemistry. The CLARITY technique in its original form(Chung et al., 2013) used electrophoretic tissue clearing (ETC) to extract lipids from large samples, which can be challenging to implement and can cause variability in final tissue quality (http://forum.claritytechniques.org). Here we cleared PFA-fixed 350 μm brain slices using the PACT protocol, which is a passive CLARITY technique with quicker passive lipid extraction and customized imaging reagents to reduce tissue damage caused by ETC(Yang et al., 2014).

After tissue clearing, we performed immunofluorescence staining on Aβ in 17 m-old *App*$^{NL\text{-}F/NL\text{-}F}$ (**Fig. 2.4a-d**) and 27 m-old *App*$^{NL\text{-}F/wt}$ (**Fig. 2.4e-h**) brain slices, and confocal imaging was done in the parietal cortex of the slices. All slices were used for *in vitro* electrophysiology recordings and post-fixed with 4% PFA. For each 350 μm slice, a z stack was taken with the objective moving in the z direction, acquiring images at different depth in the slice. Within a z stack, each image represents the fluorescence within the confocal plane (6.1 μm thick for the 10x dry objective; **Fig. 2.4a-c** and **e-g**), while the z projection image shows the overall fluorescence within the extent of the stack (**Fig. 2.4d, h**). The total depth of a stack was calculated as: $Step\ size \times (n-1) + confocal\ plane\ thickness$, in which *n* is the number of steps. Therefore, for the AD homo and het 350 μm slices, the depth of stacks were 371.5 μm (**Fig. 2.4d**) and 82.33 μm (**Fig. 2.4h**), respectively. The depth of stacks for the homozygous slice was thicker than 350 μm because of tissue swelling during the clearing process, while that for the heterozygous slice was thinner because only in that range did we see fluorescence. Also, a smaller step size was

chosen for the heterozygous slice in order to acquire more images from a limited depth of tissue with visible fluorescence. Similar to the DAB staining, 17 m AD homo brain exhibited excessive Aβ staining, while at 27 m of ages, AD het brain still only had little deposition in the cortical area, which is consistent with the original report on this model(Saito et al., 2014).

After qualitative studies with DAB and fluorescence stains in cleared slices, we have decided to use homozygous *App*$^{NL\text{-}F/NL\text{-}F}$ mice at least 12 m old to study synaptic transmission, network activities, and behavioral performance. Although undetectable soluble Aβ oligomers in the early phase of AD have been shown to be synaptotoxic(Serrano-Pozo et al., 2011), it is more difficult to determine a specific age to start with. Thus our approach was to look into a later stage with distinct pathological hallmarks in the brain, which is excessive detectable amyloidosis in our primary regions of interest, namely parietal cortex and hippocampal CA1.

2.4.2 Modest behavioral alterations were observed in App$^{NL\text{-}F/NL\text{-}F}$ *mice.*

In order to incorporate different cognitive functions into one behavior assay, we have designed a test that combines NOR, social interaction, and olfactory memory (**Fig. 2.5;** see **Method** for details). Using an automated program tracking the performance of mice in the behavior tests(Barth and Mody, 2014), we have compared the statistics from homozygous *App*$^{NL\text{-}F/NL\text{-}F}$ and age matched WT mice of both gender (Age of males: 11-21 m; Age of females: 13-20m). The data from heterozygous AD animals were not included because we were uncertain about the level of amyloidosis at the age of their tests.

Firstly, we have compared the percent time interacting with novel and familiar mouse across different test days in the WT and AD group (**Fig. 2.6a**). We plotted percent time interacting with the familiar mouse against that with the novel mouse. Then we did a linear regression on all

data points from each group (WT and AD). If the slope of the regression line was significantly different from 1, then the experimental mice were interacting more with the novel (if slope > 1) or the familiar (if slope < 1) mouse. We have also compared the slopes between groups for each day and each gender to see whether WT and AD mice behaved differently with the novel and familiar mice. The results showed that: (1) All the slopes of the regression lines, except for WT males at day 13 (**Fig. 2.6a**; "13D WT Male", black line, p=0.0163), WT and AD females at day 8 (**Fig. 2.6a**; "8D WT Female", black line, p=0.0377; "8D AD Female", red line, p=0.0229), and WT and AD females at day 13 (**Fig. 2.6a**; "13D WT Female", black line, p=0.0178; "13D AD Female", red line, p=0.0073), did not significantly deviate from 1. And only for AD males at day 13, the slope was significantly larger than 1, while all other significant groups had slopes smaller than 1. These results indicate that nearly all groups of mice spent either comparable amount of time interacting with the novel and familiar mouse or more time interacting with the familiar mouse. (2) When comparing the regression line slopes between WT and AD males/females at different test days, none of the groups showed significance, indicating that either for males or for females, the relative percent time interacting with novel and familiar did not differ between WT and AD mice..

Then, we have compared the total interaction time with novel and familiar mice between the WT and AD group (**Fig. 2.6b**). On day 5, there was no obvious difference between WT and AD mice of each gender. On day 8 and day 13, the WT males spent significantly higher percentage of time interacting than the AD males did (**Fig. 2.6b**; "8D total interaction" blue symbols, p=0.0377; "13D total interaction" blue symbols, p=0.0255; Mann-Whitney test). Although no significance was found in females, there was a trend of reduced interacting time in the AD females on day 8 and 13 as well (**Fig. 2.6b**). We have also examined the variance the interacting time across different days (**Fig. 2.6c**). The statistics showed no obvious variation in percent time interacting either with the novel/familiar mouse or the total interaction time (**Fig. 2.6c**; Two-way ANOVA

test for repeated measures), although there was a decreasing trend in the total interaction time across days. These results indicate that AD males specifically lost interest in interacting with other mice in the arena more than WT males did, while the reduction in percent time interacting was not specific to novel or familiar mouse. Also, on day 7 all experimental mice were unpaired with the familiar mouse, and it remains unclear whether this olfactory disassociation affected the behavior of AD males in the later 2 tests.

Finally, to examine the locomotion/exploratory activities of AD mice, we have compared distance traveled (m) of the WT and AD groups (**Fig. 2.6d, e**). Surprisingly, the distance of AD mice exceeded that of WT mice in tests on multiple days (**Fig. 2.6d**; "5D Distance" blue symbols, p=0.0332; "8D Distance" blue symbols, p=0.0291; "13D Distance" red symbols, p=0.0417; Mann-Whitney test). Although not significant, there was a trend of increasing distance in day 13 test in AD males as well (**Fig. 2.6d**; "13D Distance" blue symbols, p=0.2800). The fact that AD males were more active in the tests while having lower interaction time with other mice present in the arena may imply higher anxiety level and less interest in social interaction. Although not as significant as in males, AD females also had a trend in reduced total interaction time and increased travel distance compared to WT counterparts.

When compared across days, the distance traveled was significantly decreasing as more tests were done (**Fig. 2.6e**, left panel; p<0.0001; Two-way ANOVA test for repeated measures). Since both the novel and familiar mice were placed more close to the center of the arena, we were interested whether the reduction in the total interaction time in the AD group was related to them spending more time in the periphery of the environment and less time in the center. Previously, in order to assess the anxiety of the animals, we have separated the whole arena into "center" and "periphery" zones (**Fig. 2.5d**, yellow circle), and the two zones were set to have the same area. We have compared the percent time spent in the periphery in all groups

across different days, and there was a significant reduction there (**Fig. 2.6e**, right panel; p=0.0008; Two-way ANOVA for repeated measures). This reduction was present in both the WT (*p*=0.0271) and the AD (*p*=0.0352) group. Therefore, the reduction in the total interaction time in AD was not due to spending more time in the periphery of the arena.

We also checked whether there was gender difference within the WT and AD group, and found no significance in either WT or AD group (WT males vs. females and AD males vs. female; data not shown), meaning that different genders under the same genotype did not influence the behavior

2.5 Discussion

2.5.1 Delayed age of plaque deposition

In their original paper introducing the App^{NL-F} mouse model(Saito et al., 2014), Saito *et al.* claimed that they detected initial plaque deposition of Aβ at 6 months in homozygous mice. While our lack of plaque staining might be caused by technical differences, such as different antibodies used, a recent paper showed that in the NL/F mice the accumulation of Aβ in the cortex and hippocampus was barely detectable at 6 months and then progressively began accumulating detectable levels of deposition at 12-18 months of age(Masuda et al., 2016). Our DAB stains in AD homozygous slices showed limited deposition in the superficial layers of the cortex at the age of 8.3 m and extensive deposition in the cortex and hippocampus at the age of 16.5 m (**Fig. 2.2d, e**). For AD heterozygous mice, our DAB stains at 11.5 m showed no visible deposits (**Fig. 2.2f**), and the fluorescence stains in optically cleared 350 μm slice at 27 m still only exhibited very few deposits close to the edge of the cortex (**Fig. 2.4h**). Heterozygous NL-F mice were reported to exhibit cortical amyloidosis after 24 months(Saito et al., 2014). Studies in

the spatiotemporal pattern of amyloid plaque deposition in humans revealed that the deposits accumulate first in the isocortical areas, then moving to limbic and allocortical structures and in a later stage reaching subcortical structures(Thal et al., 2002; Serrano-Pozo et al., 2011). Our staining results from younger homozygous (8.3 m; **Fig. 2.2a-c**) and heterozygous mice (**Fig. 2.2f**; **Fig. 2.4h**) were consistent with these human and mouse studies, with amyloidosis starting from the cortex in both homozygous and heterozygous *App*$^{NL-F}$ mice.

2.5.2 Exploring novel techniques in studying Aβ deposition in AD mouse models

Various optical clearing techniques have enabled deep biological images in intact tissues, and each method has its own pros and cons. Here, we used the PACT (Passive CLARITY technique) protocol, which is adapted from the original CLARITY technique(Chung et al., 2013) with passive lipid extraction and customized imaging reagents to reduce tissue damage caused by electrophoretic tissue clearing (Yang et al., 2014). We have successfully transformed 350 μm slices (fixed in PFA after in vitro recordings) into optically transparent tissues, and performed immunofluorescence staining on Aβ plaques. By confocal z stack imaging, we could visualize plaques in the whole range of depth of the slice (**Fig. 2a-d**). However, we have noticed changing distribution patterns of the stains along the z direction, with more fluorescence either on the edge of the cortex or in the deeper cortical layers at each z step, while no stack image had an evenly distributed fluorescence across the confocal plane. Specifically, it seems that there was less staining deeper in the tissue, which are the images in the middle of the z stack. This could be caused by several reasons, but the most likely reason might be uneven penetration of the primary and/or secondary antibodies into the thick tissue.

Indeed, although several clearing reagents are compatible with immunofluorescence staining, there has been no comprehensive study on quantitative, depth-dependent fluorescent signals

indicating adequate tissue stability. Also, tissue penetration and fluorescence signal attenuation has always been a problem especially in the brain tissues aged mice because of they do not absorb solution as easily as tissues from developing mice and therefore can not be easily cleared. Recently the Sca*l*eS method was described, using a mild tissue-permeant sugar alchohol, sorbitol, applied to quantitative 3D-IHC imaging of Aβ plaques in the App^{NL-F} mouse model and in postmortem AD patient brain(Hama et al., 2015). With newly developed methods such as Sca*l*eS, which has a milder yet more effective tissue clearing ability and a higher compatibility with IHC staining in aged transgenic mouse brain, the 3D distribution and morphology of plaques in larger and thicker tissues may be addressed in the future.

2.5.3 Advancing the behavior test for a better diagnosis of AD in the early stage

Olfactory impairment is one of the earliest symptoms in AD, and it may be an important clinical marker and predictor that may help identify persons at increased risk(Wesson et al., 2010), and olfactory cues play a more important role for mice than for humans. Therefore, we wanted to examine whether the App^{NL-F} mice have olfactory impairments. We have designed a test that combines NOR and social interaction using a novel and a familiar mouse in the same arena with the experimental mouse (**Fig. 2.5c**), and the familiarity with the familiar mouse was established by olfactory pairing (**Fig. 2.5b**).

Our statistics showed no significant difference in the percent time interacting with the novel and familiar mice in the majority of groups, and some groups showed higher interacting time with the familiar mouse (**Fig. 2.6a**; see Results). The lack of distinguishing between a novel and a familiar mouse may indicate insufficient olfactory pairing, since the WT and AD mice could get the odor from each other as well as from the familiar mouse in our 3 interconnected cages (**Fig. 2.5b**). Also, all animals, including the novel mouse, were housed together during the test period

in our animal room, where the mixed smell from several different mice could interfere with their odor discrimination memory. Improvements could be done in future tests to ensure experimental mice could be effectively familiarized with the familiar mouse through odor memory. It is also possible memory deficits, especially odor-related memory, or impaired olfactory functions were existent in over 1 y-old WT and AD mice. Olfactory deficits are quite common in AD patients as well as normal elderly people but might have been overlooked(Nordin et al., 1995). Future improvements on this behavior test should enhance the efficacy of the olfactory pairing in young WT animals, and optimize the parameters to get a higher interaction level between the experimental mouse and the novel mouse, in order to get a clear-cut explanation on the behavior in aged and AD mice.

2.5.4 Moderate pathological phenotypes in the App^{NL-F} mice

As one of the 2nd generation mouse models of AD, the *App^{NL-F}* mice have been used to re-evaluate the disrupted phenotypes discovered in the 1st generation hAPP overexpressing models, since some of the phenotypes might be artifacts of hAPP overproduction(Masuda et al., 2016; Saito et al., 2016; Nakazono et al., 2017; Sasaguri et al., 2017). From our studies on the amyloidosis and cognitive function deficits in the NL-F mice, and various studies published, it now seems that this model has moderate pathological phenotypes compared to other existing models, such as the NL-G-F model. For example, Aβ plaque deposition becomes detectable from 12-18 m in homozygous NL-F mice, compared to 6 m in homozygous NL-G-F mice(Masuda et al., 2016). Also, the NL-F mice only had minor behavioral deficits while NL-G-F mice had clear deficits in several tests(Masuda et al., 2016). Similarly, our results showed only sparse deposition in 8 m-old homozygous and over 2 y-old heterozygous mice, and moderate behavioral alterations in our tests. Therefore, the NL-F model might be a perfect model to study minor pathological phenotypes in the early stages of AD and discover biomarkers for early

detection and diagnosis of the disease. Also, it might be useful to cross the NL-F mice with strains carrying other AD-related mutation, such as apolipoprotein E4 (APOE4)(Fryer et al., 2003), BACE1(Ohno et al., 2004), and TREM2(Jin et al., 2014; Song et al., 2017), for assessing the role of specific genetic mutations on the disease progression.

2.6 Acknowledgements

I want to give my sincere gratitude to Dr. Isabella Ferando for teaching me techniques on tissue fixation, immunostaining and imaging. I would like to thank Dr. Albert Barth for developing the automatic tracking software, and Sophia Angelides and Laurel Ormiston for setting up the behavior room and apparatus for the tests, especially Sophia who was helping with running the behavior tests as well as data collection and analysis on the WT and AD animals. I thank Dr. Thomas Carmichael for sharing the cryostat and Leica DMLB microscope, and UCLA ALMS for providing the SP5 Blue confocal microscope and related trainings. Last but not least, I want to give my many thanks to Reyes Main Lazaro, who was taking good care of our mice colonies and had been a great help in keeping the aged animals healthy for our AD studies.

Figures

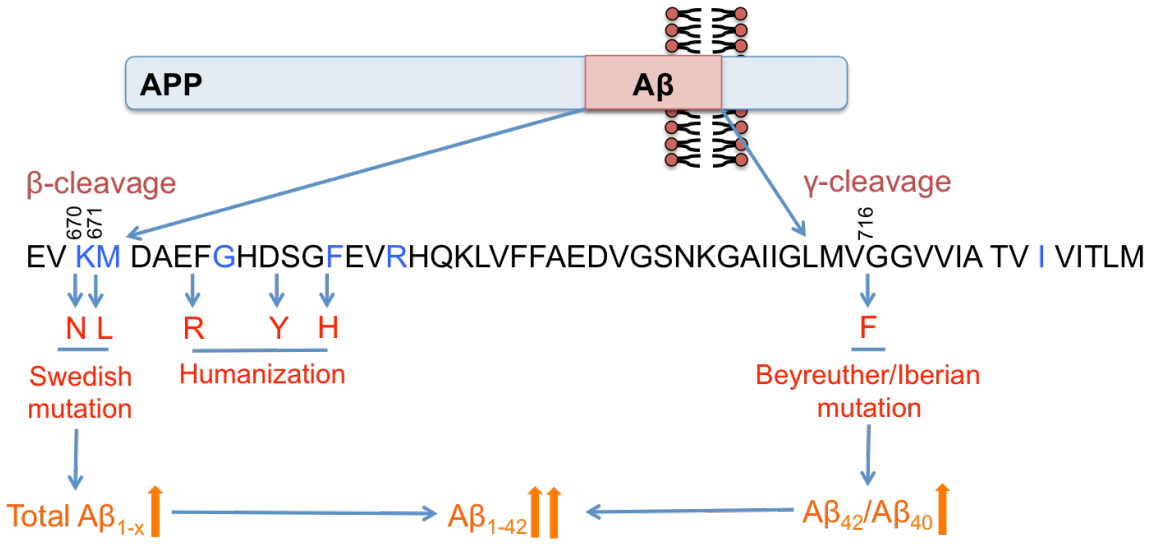

Figure 2.1: Mutations in the amyloid precursor protein (APP) of the *App*$^{NL-F}$ mouse model (adapted from Nilsson et al. 2014).

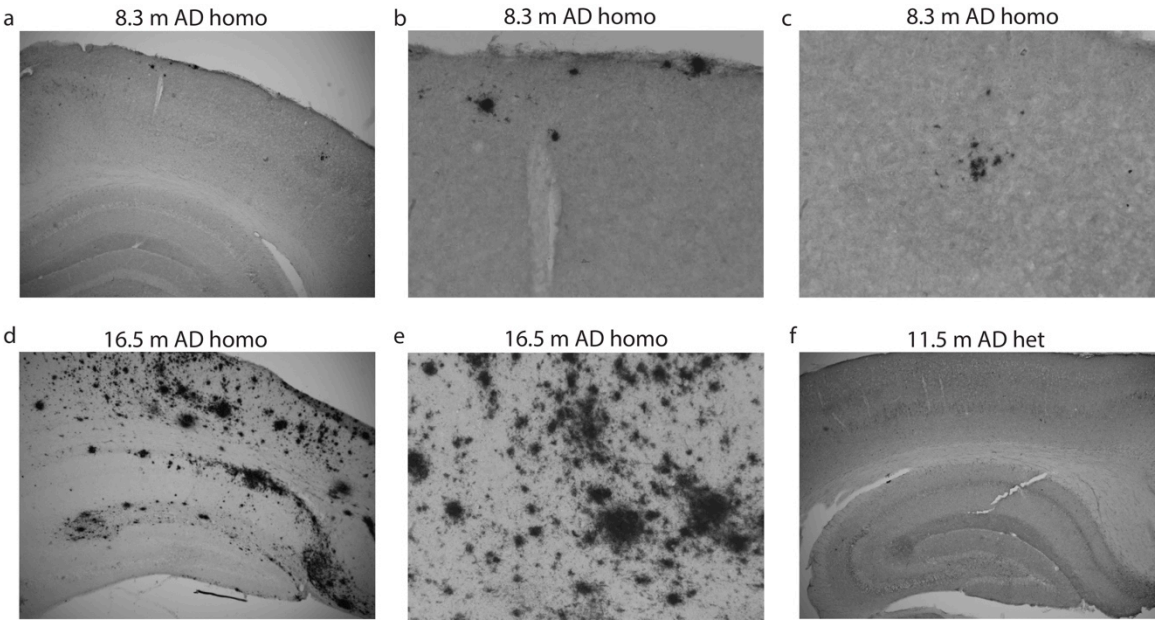

Figure 2.2: DAB stains on Aβ plaque (primary antibody IBL 18584) in *App*$^{NL\text{-}F/NL\text{-}F}$ (AD homo) and *App*$^{NL\text{-}F/wt}$ (AD het) 35 µm coronal slices.

(**a-c**) 5x (**a**) and 20x (**b, c**) objective imaging on the parietal cortex of 8.3 m AD homo. (**d, e**) 5x (**d**) and 20x (**e**) objective imaging on the plaques in 16.5 m AD homo mice. (**f**) 5x objective imaging on the plaques in 11.5 m AD het mouse.

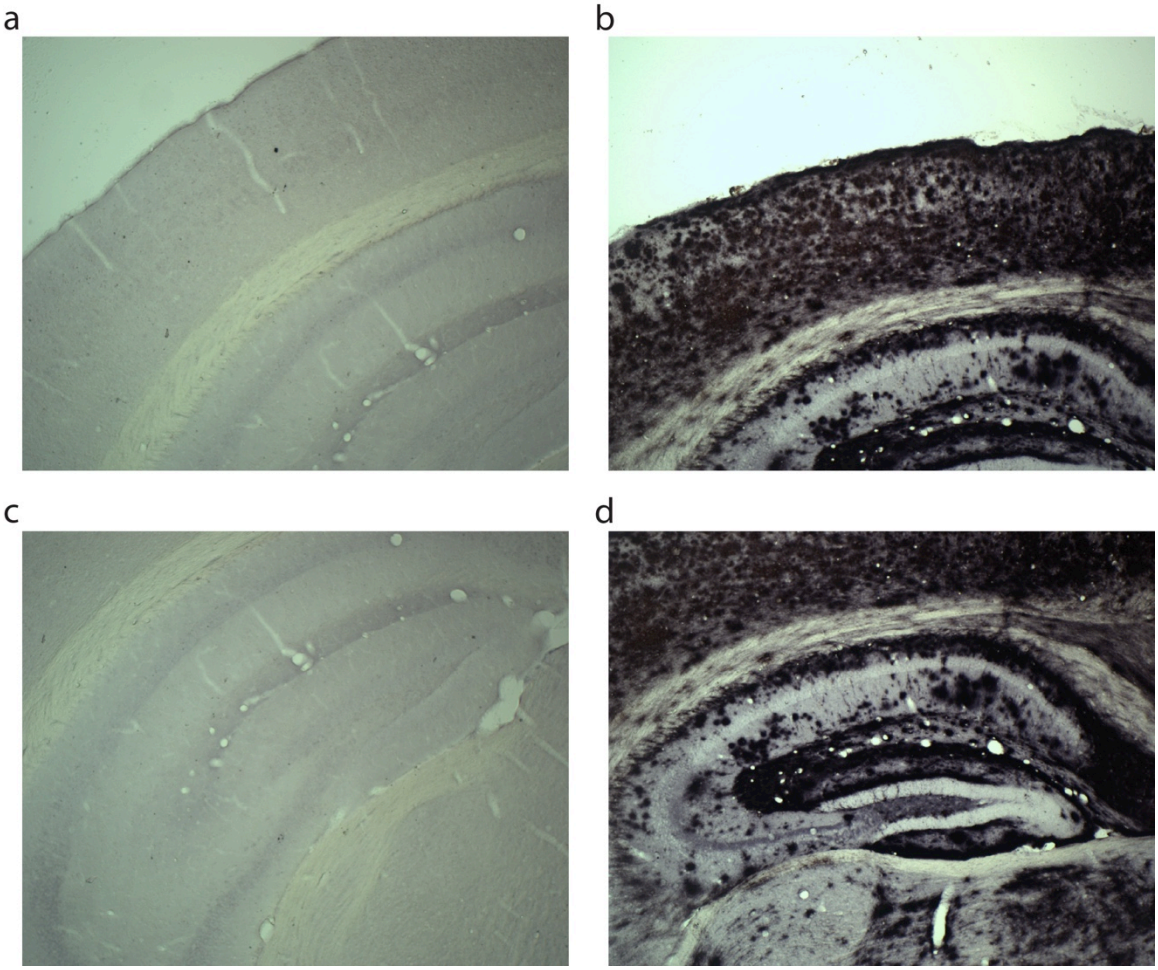

Figure 2.3: DAB stains on Aβ plaque (primary antibody CST 8243) in 30 m *App*$^{wt/wt}$ (WT) and 31.5 m *App*$^{NL\text{-}F/NL\text{-}F}$ (AD homo) 35 µm coronal slices.

(**a, b**) 5x objective imaging on the parietal cortex of WT and AD homo mice, respectively. (**c, d**) 5x objective imaging on the CA1 and DG of WT and AD homo mice, respectively.

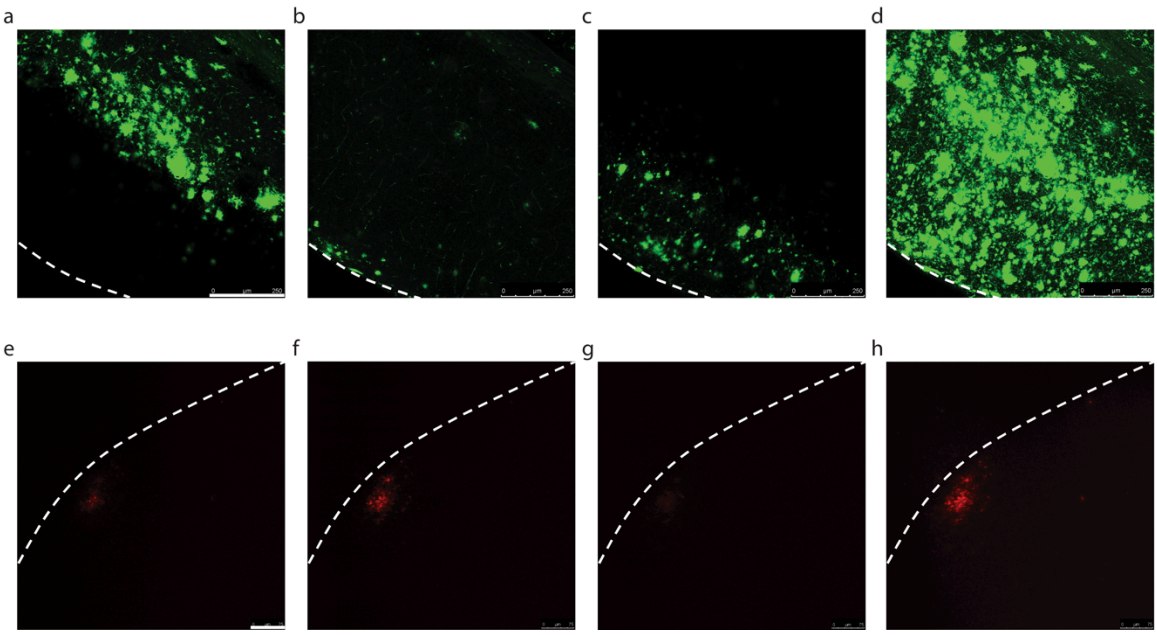

Figure 2.4: Immunofluorescence staining on Aβ plaque (primary antibody IBL 18584) in 17 m *App*$^{NL\text{-}F/NL\text{-}F}$ (AD homo) and 27 m *App*$^{NL\text{-}F/wt}$ (AD het) 350 μm coronal slices cleared with the PACT protocol. Green and red fluorescence both show plaque staining with different secondary antibodies. The white dashed lines indicate the edges of slices. A 10x dry objective was used, and the thickness of the confocal plane was 6.1 μm.

(**a-d**) Representative confocal z-stack images and z projection of the parietal cortex of 17m AD homo mouse. Number of images in the z stack = 64. Step size = 5.8 μm. Scale bar = 250 μm. Three representative images from the stack are shown in **a-c**: (**a**) Image No. 5 (29 μm from the top); (**b**) Image No. 30 (174 μm from the top); (**c**) Image No. 55 (319 μm from the top). The z projection of all images is shown in **d**. (**e-h**) Representative confocal z-stack images and z projection of the parietal cortex of 27 m AD het mouse. Number of images in the z stack = 78. Step size = 0.99 μm. Scale bar = 75 μm. Three representative images from the stack are shown in **e-g**: (**e**) Image No. 15 (14.85 μm from the top); (**f**) Image No. 40 (39.6 μm from the top); (**g**) Image No. 65 (64.35 μm from the top). The z projection of all images is shown in **h**.

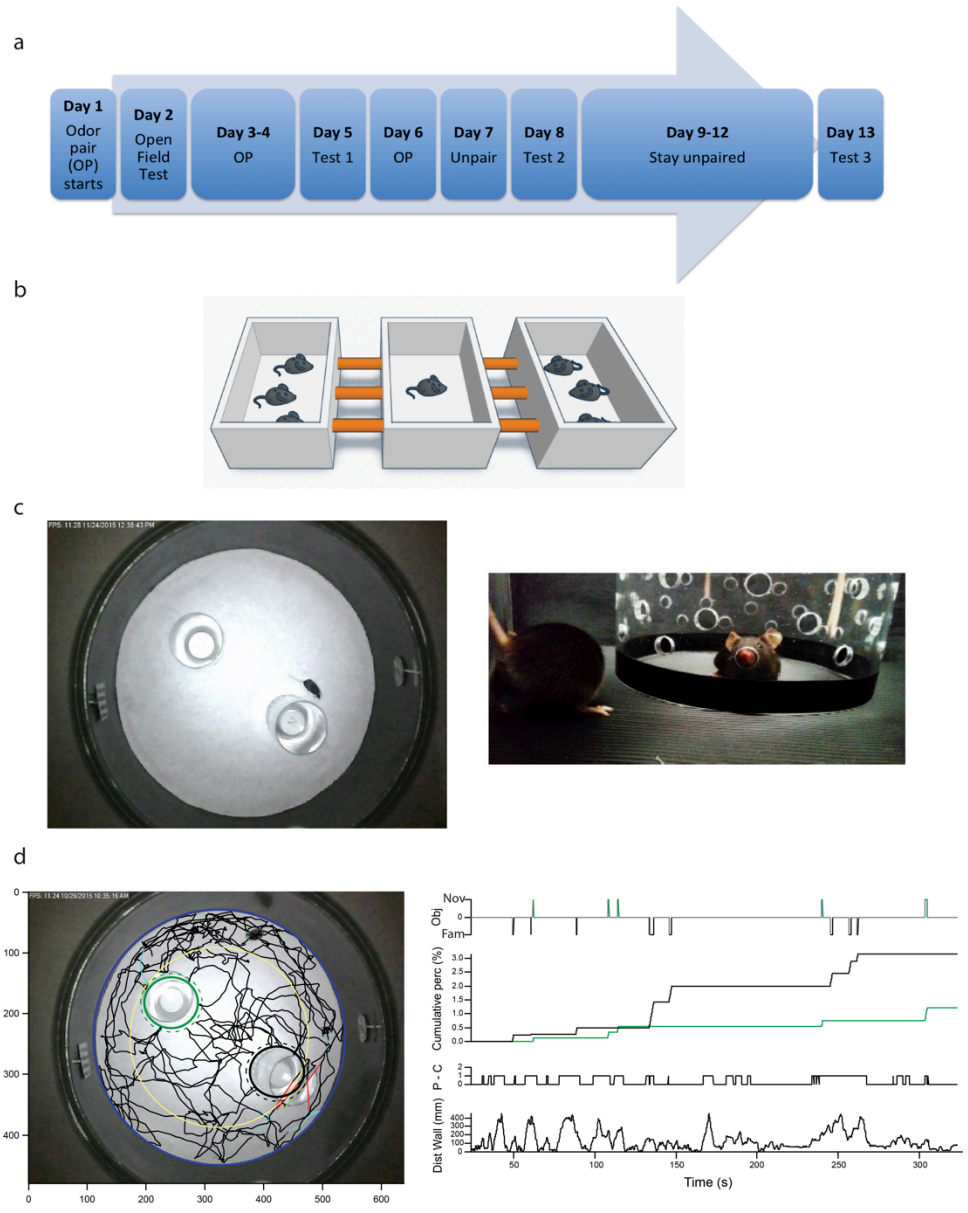

Figure 2.5: Behavior test protocol and setups, and automated software tracking the performance of mice.

(**a**) Behavior test protocol (See **Method** for details). Briefly, the procedure lasted for 13 days for each mouse. On day 1 the experimental mice were odor paired with a “familiar mouse”, and they stayed paired until day 7. On day 2 experimental mice were subjected to an open field test for habituation. A total of 3 tests were performed on day 5, 8, and 13, respectively. (**b**) The

olfactory pairing apparatus, in which 3 customized cages were interconnected with plastic tubes allowing odor exchange while preventing physical interaction between animals in different cages. For each group of tests, the familiar mouse was put in the middle cage, with age-matched control (WT) and AD homo (*App*$^{NL\text{-}F/NL\text{-}F}$) of the same gender in each side cage. (**c**) The arena used for the tests. The novel and familiar mice were placed inside of two plastic cylindrical containers in the arena, and small openings on the containers enabled the interaction between the test animal and the novel/familiar mouse (see the right panel). Two visual cues were taped on the wall. Relative locations of the novel and familiar mice as well as relative locations of the visual cues were randomized among tests. (**d**) An automated Igor program tracking the performance of the experimental mouse along the 5 min test with a time precision of 0.1 s. The left panel shows the manually set boarder of arena (blue circle) and the edges of the containers with the familiar (black circle) and novel (green circle) mice. An interaction with the novel or familiar mouse was detected if the nose of the experimental mouse was within the dashed black/green lines.

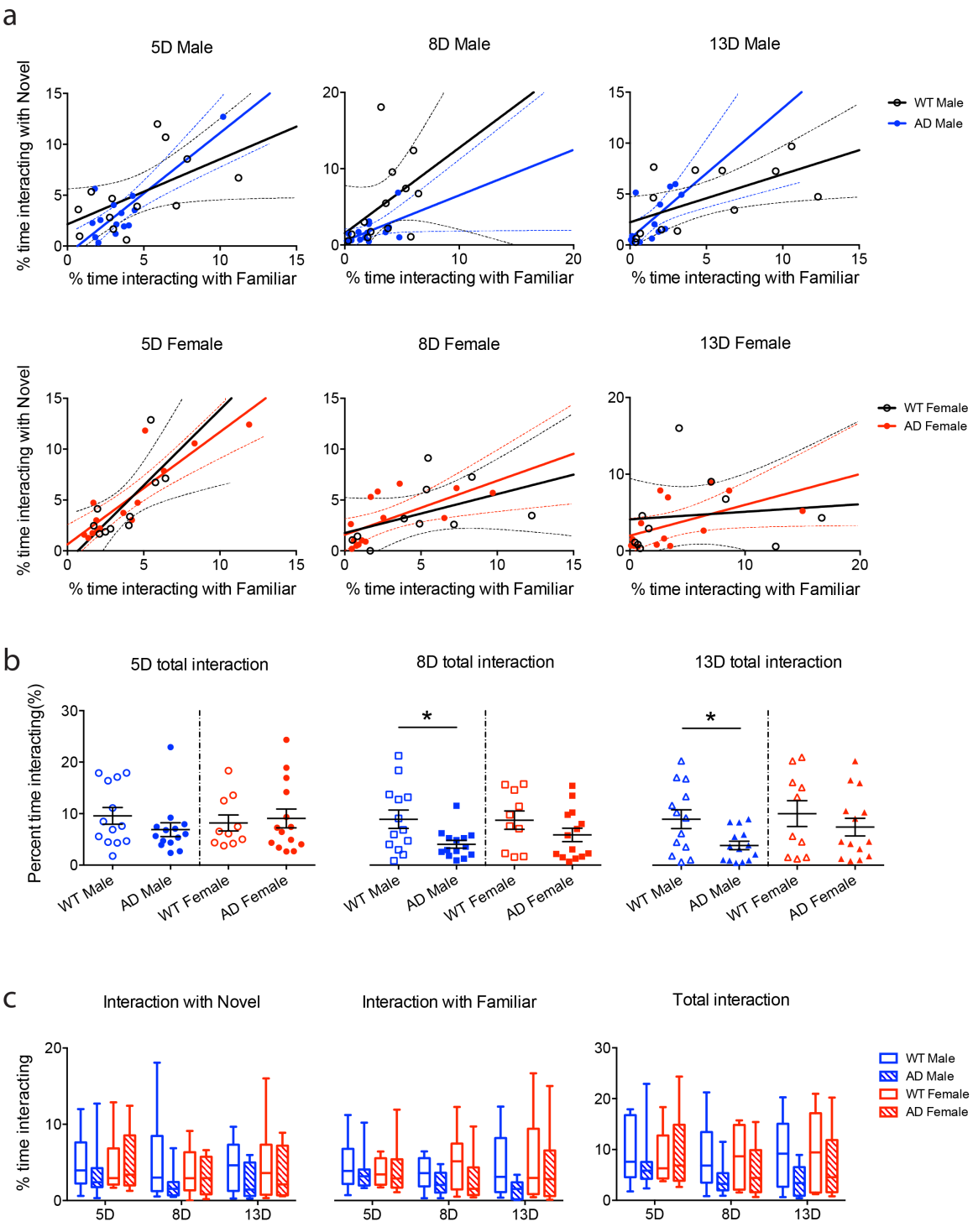
a
5D Male
8D Male
13D Male
% time interacting with Novel
% time interacting with Familiar
WT Male
AD Male
5D Female
8D Female
13D Female
WT Female
AD Female
b
5D total interaction
8D total interaction
13D total interaction
Percent time interacting(%)
*
WT Male
AD Male
WT Female
AD Female
c
Interaction with Novel
Interaction with Familiar
Total interaction
% time interacting
5D
8D
13D

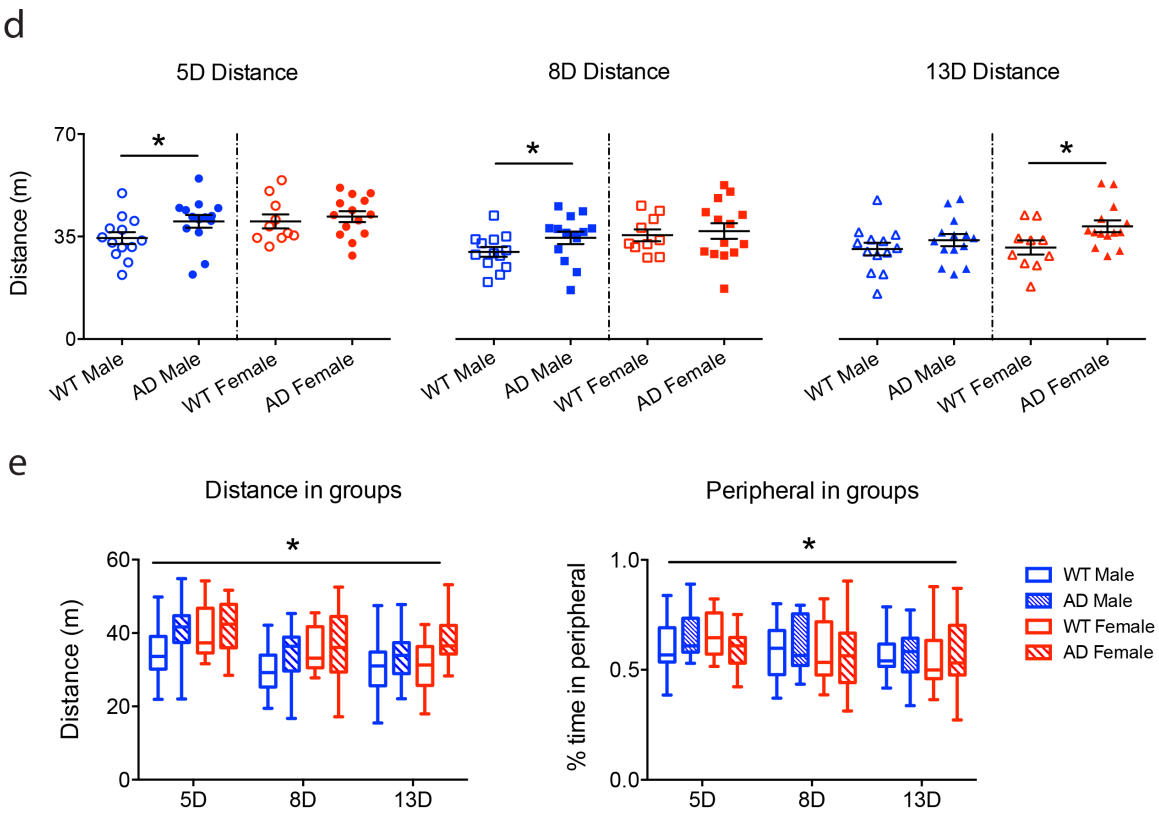

Figure 2.6: Performance of WT and AD (*App*$^{NL\text{-}F/NL\text{-}F}$) male and female mice in the behavior tests. blue: Males; Red: females. Number of animals: N = 13 vs. 14, WT vs. AD male; N=10 vs. 14, WT female vs. AD female. A $p<0.05$ is considered to be significant, and significance is denoted with asterisks.

(**a**) Comparisons on percent time interacting (%) with novel and familiar mice between WT and AD males (upper panel) and females (lower panel) on different test days. Each circle represents a mouse. The solid lines are linear regression of the circles within each group, with the dashed lines as 95% confidence interval. The slopes of the two regression lines within each graph were compared to a slope of 1 and to each other as well. (**b**) Comparisons on total percent time interacting (%) with novel and familiar mice between WT and AD animals on different test days. All group data is represented as mean ± SEM (standard error of mean), and significance was established with Mann-Whitney test. (**c**) Repeated measures on the percent time interacting

with the novel and familiar mice, respectively, and the total percent time interacting across different test days. Two-way ANOVA was used to test the variance across days and among different groups. (**d**) Comparisons on the distance (m) traveled between WT and AD mice during the test on different days. All group data is represented as mean ± SEM (standard error of mean), and significance was established with Mann-Whitney test. (**e**) Repeated measures on distance traveled (m) (left panel) and percent time spent in the peripheral of the arena across different test days. Two-way ANOVA was used to test the variance across days and among different groups. The asterisk denotes significant variance across days.

Bibliography

Antunes M, Biala G (2012) The novel object recognition memory: Neurobiology, test procedure, and its modifications. Cogn Process 13:93–110.

Barker GRI, Warburton EC (2011) When Is the Hippocampus Involved in Recognition Memory? J Neurosci 31:10721–10731.

Barth AMI, Mody I (2014) Novel test of motor and other dysfunctions in mouse neurological disease models. J Neurosci Methods 221:151–158.

Bateman RJ, Aisen PS, De Strooper B, Fox NC, Lemere CA, Ringman JM, Salloway S, Sperling RA, Windisch M, Xiong C (2011) Autosomal-dominant Alzheimer's disease: a review and proposal for the prevention of Alzheimer's disease. Alzheimers Res Ther 3:1.

Blessed G, Tomlinson BE, Roth M (1968) The Association Between Quantitative Measures of Dementia and of Senile Change in the Cerebral Grey Matter of Elderly Subjects. Br J Psychiatry 114:797–811.

Braak H, Braak E (1991) Demonstration of Amyloid Deposits and Neurofibrillary Changes in Whole Brain Sections. Brain Pathol 1:213–216.

Burns A, Iliffe S (2009) Alzheimer's disease. BMJ 338:b158.

Burns A, Jacoby R, Levy R (1990) Psychiatric phenomena in Alzheimer's disease. IV: Disorders of behaviour. Br J Psychiatry 157:86–94.

Cacace AT (2007) Aging, Alzheimer's Disease, and Hearing Impairment: Highlighting Relevant Issues and Calling for Additional Research. Am J Audiol 16:2–3.

Campion D, Dumanchin C, Hannequin D, Dubois B, Belliard S, Puel M, Thomas-Anterion C, Michon A, Martin C, Charbonnier F, Raux G, Camuzat A, Penet C, Mesnage V, Martinez M, Clerget-Darpoux F, Brice A, Frebourg T (1999) Early-Onset Autosomal Dominant Alzheimer Disease: Prevalence, Genetic Heterogeneity, and Mutation Spectrum. Am J Hum Genet 65:664–670.

Cheng IH, Scearce-Levie K, Legleiter J, Palop JJ, Gerstein H, Bien-Ly N, Puoliväli J, Lesné S,

Ashe KH, Muchowski PJ, Mucke L (2007) Accelerating amyloid-beta fibrillization reduces oligomer levels and functional deficits in Alzheimer disease mouse models. J Biol Chem 282:23818–23828.

Chung K, Wallace J, Kim S-Y, Kalyanasundaram S, Andalman AS, Davidson TJ, Mirzabekov JJ, Zalocusky KA, Mattis J, Denisin AK, Pak S, Bernstein H, Ramakrishnan C, Grosenick L, Gradinaru V, Deisseroth K (2013) Structural and molecular interrogation of intact biological systems. Nature 497:332–337.

Cirrito JR, Yamada KA, Finn MB, Sloviter RS, Bales KR, May PC, Schoepp DD, Paul SM, Mennerick S, Holtzman DM (2005) Synaptic Activity Regulates Interstitial Fluid Amyloid-β Levels In Vivo. Neuron 48:913–922.

Cissé M, Halabisky B, Harris J, Devidze N, Dubal DB, Sun B, Orr A, Lotz G, Kim DH, Hamto P, Ho K, Yu G-Q, Mucke L (2011) Reversing EphB2 depletion rescues cognitive functions in Alzheimer model. Nature 469:47–52.

Citron M, Oltersdorf T, Haass C, McConlogue L, Hung AY, Seubert P, Vigo-Pelfrey C, Lieberburg I, Selkoe DJ (1992) Mutation of the beta-amyloid precursor protein in familial Alzheimer's disease increases beta-protein production. Nature 360:672–674.

Cronin-Golomb A, Rizzo JF, Corkin S, Growdon JH (1991) Visual function in Alzheimer's disease and normal aging. AnnNYAcadSci 640:28–35.

Cruts M, Theuns J, Van Broeckhoven C (2012) Locus-specific mutation databases for neurodegenerative brain diseases. Hum Mutat 33:1340–1344.

Doty RL (1991) Olfactory capacities in aging and Alzheimer's disease. Psychophysical and anatomic considerations. Ann N Y Acad Sci 640:20–27.

Ebensperger G, Ebensperger R, Herrera EA, Riquelme RA, Sanhueza EM, Lesage F, Marengo JJ, Tejo RI, Llanos AJ, Reyes R V (2005) Fetal brain hypometabolism during prolonged hypoxaemia in the llama. J Physiol 567:963–975.

Eichenbaum HB, Otto TA, Wible CG PJ (1991) Building a model of the hippocampus in olfaction

and memory. In: Building a model of the hippocampus in olfaction and memory., pp 167–210. The MIT Press, MA, USA.

Ertürk A, Becker K, Jährling N, Mauch CP, Hojer CD, Egen JG, Hellal F, Bradke F, Sheng M, Dodt HU (2012) Three-dimensional imaging of solvent-cleared organs using 3DISCO. Nat Protoc 7:1983–1995.

Esiri MM, Wilcock GK (1984) The olfactory bulbs in Alzheimer's disease. J Neurol Neurosurgery, Psychiatry 47:56–60.

Ferri CP, Prince M, Brayne C, Brodaty H, Fratiglioni L, Ganguli M, Hall K, Hasegawa K, Hendrie H, Huang Y, Jorm A, Mathers C, Menezes PR, Rimmer E, Scazufca M (2005) Global prevalence of dementia: a Delphi consensus study. Lancet 366:2112–2117.

Findeis MA (2007) The role of amyloid beta peptide 42 in Alzheimer's disease. Pharmacol Ther 116:266–286.

Fryer JD, Taylor JW, DeMattos RB, Bales KR, Paul SM, Parsadanian M, Holtzman DM (2003) Apolipoprotein E markedly facilitates age-dependent cerebral amyloid angiopathy and spontaneous hemorrhage in amyloid precursor protein transgenic mice. J Neurosci 23:7889–7896.

Games D, Adams D, Alessandrini R, Barbour R, Berthelette P, Blackwell C, Carr T, Clemens J, Donaldson T, Gillespie F (1995) Alzheimer-type neuropathology in transgenic mice overexpressing V717F beta-amyloid precursor protein. Nature 373:523–527.

Glenner GG, Wong CW (1984a) Alzheimer's disease and Down's syndrome: Sharing of a unique cerebrovascular amyloid fibril protein. Biochem Biophys Res Commun 122:1131–1135.

Glenner GG, Wong CW (1984b) Alzheimer's disease: Initial report of the purification and characterization of a novel cerebrovascular amyloid protein. Biochem Biophys Res Commun 120:885–890.

Götz J, Streffer JR, David D, Schild A, Hoerndli F, Pennanen L, Kurosinski P, Chen F (2004)

Transgenic animal models of Alzheimer's disease and related disorders: histopathology, behavior and therapy. Mol Psychiatry 9:664–683.

Grundke-Iqbal I, Iqbal K, Quinlan M, Tung YC, Zaidi MS, Wisniewski HM (1986) Microtubule-associated protein tau. A component of Alzheimer paired helical filaments. J Biol Chem 261:6084–6089.

Guardia-Laguarta C, Pera M, Clarimón J, Molinuevo JL, Sánchez-Valle R, Lladó A, Coma M, Gómez-Isla T, Blesa R, Ferrer I, Lleó A (2010) Clinical, neuropathologic, and biochemical profile of the amyloid precursor protein I716F mutation. J Neuropathol Exp Neurol 69:53–59.

Hama H, Hioki H, Namiki K, Hoshida T, Kurokawa H, Ishidate F, Kaneko T, Akagi T, Saito T, Saido T, Miyawaki A (2015) ScaleS: an optical clearing palette for biological imaging. Nat Neurosci 18:1518–1529.

Hama H, Kurokawa H, Kawano H, Ando R, Shimogori T, Noda H, Fukami K, Sakaue-Sawano A, Miyawaki A (2011) Scale: A chemical approach for fluorescence imaging and reconstruction of transparent mouse brain. Nat Neurosci 14:1481–1488.

Hoe HS, Lee HK, Pak DTS (2012) The upside of APP at synapses. CNS Neurosci Ther 18:47–56.

Hsiao K, Chapman P, Nilsen S, Eckman C, Harigaya Y, Younkin S, Yang F, Cole G (1996) Correlative Memory Deficits, Abeta Elevation, and Amyloid Plaques in Transgenic Mice. Science (80-) 274:99–103.

Jin SC, Benitez BA, Karch CM, Cooper B, Skorupa T, Carrell D, Norton JB, Hsu S, Harari O, Cai Y, Bertelsen S, Goate AM, Cruchaga C (2014) Coding variants in TREM2 increase risk for Alzheimer's disease. Hum Mol Genet 23:5838–5846.

Kamenetz F, Tomita T, Hsieh H, Seabrook G, Borchelt D, Iwatsubo T, Sisodia S, Malinow R (2003) APP Processing and Synaptic Function. Neuron 37:925–937.

Katzman R (1976) The Prevalence and Malignancy of Alzheimer Disease. Arch Neurol 33:217.

Kosik KS, Joachim CL, Selkoe DJ (1986) Microtubule-associated protein tau (tau) is a major antigenic component of paired helical filaments in Alzheimer disease. Proc Natl Acad Sci U S A 83:4044–4048.

Kuwajima T, Sitko AA, Bhansali P, Jurgens C, Guido W, Mason C (2013) ClearT: a detergent- and solvent-free clearing method for neuronal and non-neuronal tissue. Development 140:1364–1368.

Levy-lahad E, Wasco W, Poorkaj P, Romano DM, Oshima J, Pettingell WH, Yu C, Jondro PD, Schmidt SD, Wang K, Crowley AC, Fu Y, Guenette SY, Galas D, Nemens E, Wijsman EM, Bird TD, Schellenberg GD, Tanzi RE (1995) Candidate Gene for the Chromosome 1 Familial Alzheimer's Disease Locus. Science (80-) 269:973–977.

Levy E, Carman MD, Fernandez-Madrid IJ, Power MD, Lieberburg I, van Duinen SG, Th M Bots GA, Luyendijk W (1990) Mutation of the Alzheimer's Disease Amyloid Gene in Hereditary Cerebral Hemorrhage, Dutch Type. Frangione Source Sci New Ser 248:1124–1126.

Lichtenthaler SF, Wang R, Grimm H, Uljon SN, Masters CL, Beyreuther K (1999) Mechanism of the cleavage specificity of Alzheimer's disease gamma-secretase identified by phenylalanine-scanning mutagenesis of the transmembrane domain of the amyloid precursor protein. Proc Natl Acad Sci U S A 96:3053–3058.

Lindeboom J, Weinstein H (2004) Neuropsychology of cognitive ageing, minimal cognitive impairment, Alzheimer's disease, and vascular cognitive impairment. Eur J Pharmacol 490:83–86.

Masuda A, Kobayashi Y, Kogo N, Saito T, Saido TC, Itohara S (2016) Cognitive deficits in single App knock-in mouse models. Neurobiol Learn Mem 135:73–82.

Mayeux R, Stern Y (2012) Epidemiology of Alzheimer disease. Cold Spring Harb Perspect Med 2:a006239-.

McCaffrey RJ, Duff K, Gary Solomon MS (2000) Olfactory Dysfunction Discriminates Probable Alzheimer's Dementia From Major Depression: A Cross- Validation and Extension. J

Neuropsychiatry Clin Neurosci 12.

Mitani Y, Yarimizu J, Saita K, Uchino H, Akashiba H, Shitaka Y, Ni K, Matsuoka N (2012) Differential effects between γ-secretase inhibitors and modulators on cognitive function in amyloid precursor protein-transgenic and nontransgenic mice. J Neurosci 32:2037–2050.

Mucke L, Masliah E, Yu G-Q, Mallory M, Rockenstein EM, Tatsuno G, Hu K, Kholodenko D, Johnson-Wood K, Mcconlogue L (2000) High-Level Neuronal Expression of Aβ 1–42 in Wild-Type Human Amyloid Protein Precursor Transgenic Mice: Synaptotoxicity without Plaque Formation. J Neurosci 20:4050–4058.

Mucke L, Selkoe DJ (2012) Neurotoxicity of amyloid β-protein: synaptic and network dysfunction. Cold Spring Harb Perspect Med 2:a006338.

Murphy C (1999) Loss of Olfactory Function in Dementing Disease. Physiol Behav 66:177–182.

Nakazono T, Lam TN, Patel AY, Kitazawa M, Saito T, Saido TC, Igarashi KM (2017) Impaired In Vivo Gamma Oscillations in the Medial Entorhinal Cortex of Knock-in Alzheimer Model. Front Syst Neurosci 11:1–13.

Nilsson P, Saito T, Saido TC (2014) New mouse model of Alzheimer's. ACS Chem Neurosci 5:499–502.

Nordin S, Monsch AU, Murphy C (1995) Unawareness of Smell Loss in Normal Aging and Alzheimer's Disease: Discrepancy between Self-Reported and Diagnosed Smell Sensitivity. Journals Gerontol Ser B Psychol Sci Soc Sci 50B:P187–P192.

Oakley H, Cole SL, Logan S, Maus E, Shao P, Craft J, Guillozet-Bongaarts A, Ohno M, Disterhoft J, Eldik L Van, Berry R, Vassar R (2006) Intraneuronal β-Amyloid Aggregates, Neurodegeneration, and Neuron Loss in Transgenic Mice with Five Familial Alzheimer's Disease Mutations: Potential Factors in Amyloid Plaque Formation. J Neurosci 26:10129–10140.

Ohno M, Sametsky EA, Younkin LH, Oakley H, Younkin SG, Citron M, Vassar R, Disterhoft JF (2004) BACE1 Deficiency Rescues Memory Deficits and Cholinergic Dysfunction in a

Mouse Model of Alzheimer's Disease. Neuron 41:27–33.

Ormiston LD, Angelides S, Barth A, Mody I. A novel behavior approach to examining spatial learning and social interaction in a mouse model of temporal lobe epilepsy. Program No. 588.13. 2015 Neuroscience Meeting Planner. Washington, DC: Society for Neuroscience, 2015. Online.

Ossenkoppele R et al. (2015) The behavioural/dysexecutive variant of Alzheimer's disease: clinical, neuroimaging and pathological features. Brain 138:2732–2749.

Palop JJ, Chin J, Bien-Ly N, Massaro C, Yeung BZ, Yu G-Q, Mucke L (2005) Vulnerability of dentate granule cells to disruption of arc expression in human amyloid precursor protein transgenic mice. J Neurosci 25:9686–9693.

Palop JJ, Chin J, Roberson ED, Wang J, Thwin MT, Bien-Ly N, Yoo J, Ho KO, Yu G-Q, Kreitzer A, Finkbeiner S, Noebels JL, Mucke L (2007) Aberrant excitatory neuronal activity and compensatory remodeling of inhibitory hippocampal circuits in mouse models of Alzheimer's disease. Neuron 55:697–711.

Palop JJ, Jones B, Kekonius L, Chin J, Yu G-Q, Raber J, Masliah E, Mucke L (2003) Neuronal depletion of calcium-dependent proteins in the dentate gyrus is tightly linked to Alzheimer's disease-related cognitive deficits. Proc Natl Acad Sci U S A 100:9572–9577.

Palop JJ, Mucke L (2010) Amyloid-beta-induced neuronal dysfunction in Alzheimer's disease: from synapses toward neural networks. Nat Neurosci 13:812–818.

Palop JJ, Mucke L, Roberson ED (2011) Quantifying biomarkers of cognitive dysfunction and neuronal network hyperexcitability in mouse models of Alzheimer's disease: depletion of calcium-dependent proteins and inhibitory hippocampal remodeling. Methods Mol Biol 670:245–262.

Perry RJ, Hodges JR (1999) Attention and executive deficits in Alzheimer's disease: A critical review. Brain 122:383–404.

Priller C, Thomas B, Gerda M, Krebs B, Kretzschmar HA, Herms J (2006) Synapse Formation

and Function Is Modulated by the Amyloid Precursor Protein. J Neurosci 26:7212–7221.

Puzzo D, Privitera L, Leznik E, Fà M, Staniszewski A, Palmeri A, Arancio O (2008) Picomolar Amyloid-β Positively Modulates Synaptic Plasticity and Memory in Hippocampus. J Neurosci 28:14537–14545.

Rogaev EI et al. (1995) Familial Alzheimer's disease in kindreds with missense mutations in a gene on chromosome 1 related to the Alzheimer's disease type 3 gene. Nature 376:775–778.

Saito T, Matsuba Y, Mihira N, Takano J, Nilsson P, Itohara S, Iwata N, Saido TC (2014) Single App knock-in mouse models of Alzheimer's disease. Nat Neurosci 17:661–663.

Saito T, Matsuba Y, Yamazaki N, Hashimoto S, Saido TC (2016) Calpain Activation in Alzheimer's Model Mice Is an Artifact of APP and Presenilin Overexpression. J Neurosci 36:9933–9936.

Sasaguri H, Nilsson P, Hashimoto S, Nagata K, Saito T, De Strooper B, Hardy J, Vassar R, Winblad B, Saido TC (2017) APP mouse models for Alzheimer's disease preclinical studies. EMBO J 36:e201797397.

Schmechel DE, Saunders AM, Strittmatter WJ, CRAINtt BJ, HULETTEt CM, Joo SH, Pericaknvance MA, Goldgaberii D, Roses AD (1993) Increased amyloid β-peptide deposition in cerebral cortex as a consequence of apolipoprotein E genotype in late-onset Alzheimer disease. Neurobiology 90:9649–9653.

Selkoe D, Mandelkow E, Holtzman D (2012) Deciphering Alzheimer disease. Cold Spring Harb Perspect Med 2:a011460.

Selkoe DJ, Podlisny MB (2002) Deciphering the Genetic Basis of Alzheimer's Disease. Annu Rev Genomics Hum Genet 3:67–99.

Seo J, Giusti-Rodríguez P, Zhou Y, Rudenko A, Cho S, Ota KT, Park C, Patzke H, Madabhushi R, Pan L, Mungenast AE, Guan JS, Delalle I, Tsai LH (2014) Activity-dependent p25 generation regulates synaptic plasticity and aβ-induced cognitive impairment. Cell

157:486–498.

Serrano-Pozo A, Frosch MP, Masliah E, Hyman BT (2011) Neuropathological alterations in Alzheimer disease. Cold Spring Harb Perspect Med 1:a006189.

Sherrington R et al. (1995) Cloning of a gene bearing missense mutations in early-onset familial Alzheimer's disease. Nature 375:754–760.

Song W, Hooli B, Mullin K, Jin SC, Cella M, Ulland TK, Wang Y, Tanzi RE, Colonna M (2017) Alzheimer's disease-associated TREM2 variants exhibit either decreased or increased ligand-dependent activation.

Strittmatter WJ, Saunders AM, Schmechel D, Pericak-vance M, Enghild J, Salvesen GS, Roses AD (1993) Apolipoprotein E: High-avidity binding to ,B-amyloid and increased frequency of type 4 allele in late-onset familial Alzheimer disease. Med Sci Commun by William J Lennarz 90:1977–1981.

Sturchler-Pierrat C, Abramowski D, Duke M, Wiederhold K-H, Mistl C, Rothacher S, Ledermann B, Burki K, Frey P, Paganetti PA, Waridel C, Calhoun ME, Jucker M, Probst A, Staufenbiel M, Sommer B (1997) Two amyloid precursor protein transgenic mouse models with Alzheimer disease-like pathology. Proc Natl Acad Sci 94:13287–13292.

Susaki EA, Tainaka K, Perrin D, Kishino F, Tawara T, Watanabe TM, Yokoyama C, Onoe H, Eguchi M, Yamaguchi S, Abe T, Kiyonari H, Shimizu Y, Miyawaki A, Yokota H, Ueda HR (2014) Whole-brain imaging with single-cell resolution using chemical cocktails and computational analysis. Cell 157:726–739.

Tanzi RE, Bertram L (2005) Twenty years of the Alzheimer's disease amyloid hypothesis: a genetic perspective. Cell 120:545–555.

Thal DR, Rüb U, Orantes M, Braak H (2002) Phases of A beta-deposition in the human brain and its relevance for the development of AD. Neurology 58:1791–1800.

Verret L, Mann EO, Hang GB, Barth AMI, Cobos I, Ho K, Devidze N, Masliah E, Kreitzer AC, Mody I, Mucke L, Palop JJ (2012) Inhibitory interneuron deficit links altered network activity

and cognitive dysfunction in Alzheimer model. Cell 149:708–721.

Walsh DM, Selkoe DJ (2004) Deciphering the molecular basis of memory failure in Alzheimer's disease. Neuron 44:181–193.

Wesson DW, Wilson D a, Nixon R a (2010) Should olfactory dysfunction be used as a biomarker of Alzheimer's disease? Expert Rev Neurother 10:633–635.

Whyte LS, Hemsley KM, Lau AA, Hassiotis S, Saito T, Saido TC, Hopwood JJ, Sargeant TJ (2018) Reduction in open field activity in the absence of memory deficits in the AppNL−G−F knock-in mouse model of Alzheimer's disease. Behav Brain Res 336:177–181.

Wood JG, Mirrat SS, Pollock NJ, Bindert LI, Krause RM (1986) Neurofibrillary tangles of Alzheimer disease share antigenic determinants with the axonal microtubule-associated protein tau. Med Sci 83:4040–4043.

Yan X-X, Cai Y, Shelton J, Deng S-H, Luo X-G, Oddo S, Laferla FM, Cai H, Rose GM, Patrylo PR (2012) Chronic temporal lobe epilepsy is associated with enhanced Alzheimer-like neuropathology in 3×Tg-AD mice. PLoS One 7:e48782.

Yang B, Treweek JB, Kulkarni RP, Deverman BE, Chen C-K, Lubeck E, Shah S, Cai L, Gradinaru V (2014) Single-Cell Phenotyping within Transparent Intact Tissue through Whole-Body Clearing. Cell 158:945–958.

Young-Pearse TL, Bai J, Chang R, Zheng JB, Loturco JJ, Selkoe DJ (2007) A Critical Function for β-Amyloid Precursor Protein in Neuronal Migration Revealed by In Utero RNA Interference. J Neurosci 27:14459–14469.

Younkin SG (1998) The role of Aβ in Alzheimer's disease. J Physiol 92:289–292.

Zar JH (1998) Biostatistical Analysis, 4th Eition. Prentice Hall.

Zhang R, Xue G, Wang S, Zhang L, Shi C, Xie X (2012) Novel object recognition as a facile behavior test for evaluating drug effects in APP/PS1 Alzheimer's disease mouse model. J Alzheimer's Dis 31:801–812.

Zheng H, Jiang M, Trumbauer ME, Sirinathsinghji DJS, Hopkins R, Smith DW, Heavens RP, Dawson GF, Boyce S, Conner MW, Stevens KA, Slunt HH, Sisodia SS, Chen HY, Van Der Ploeg ' LHT (1995) p-Amyloid Precursor Protein-Deficient Mice Show Reactive Gliosis and Decreased Locomotor Activity. Cell 81:525–531.

Zheng H, Koo EH (2011) Biology and pathophysiology of the amyloid precursor protein. Mol Neurodegener 6:27.

Chapter III

Synaptic Alterations Consistent with Parvalbumin-expressing Interneuron Dysfunction in a Knock-in Mouse Model of Alzheimer's disease

Synaptic alterations consistent with parvalbumin-expressing interneuron dysfunction in a knock-in mouse model of Alzheimer's disease

Lingxuan Chen[1], Takashi Saito[3], Takaomi C. Saido[3], Istvan Mody[1,2]

[1]MCIP Interdepartmental Ph.D. Program and [2]Department of Neurology, The David Geffen School of Medicine at UCLA, Los Angeles, CA, 90095, USA, and [3]Laboratory for Proteolytic Neuroscience, RIKEN Brain Science Institute, Wako, Saitama, 3510198, Japan

Abstract

Alzheimer's disease (AD) is a neurodegenerative disorder that has become a compelling global public health concern. Besides pathological hallmarks such as extracellular amyloid plaques, intracellular neurofibrillary tangles, and loss of neurons and synapses, clinical reports have shown that epileptiform activity, even seizures, can occur early in the disease. In the hAPPJ20 mouse model of AD, dysfunction in parvalbumin-expressing interneurons (PV INs) and subsequent network hyperactivity were reported, yet it could be an artifact caused by the intrinsic properties of this specific model. Here we used the *App*$^{NL-F}$ mouse model generated by a gene knock-in approach, which could reduce the artificial phenotypes possibly existent in previous models. Our studies on the excitatory and inhibitory synaptic transmission in parietal cortex layer 2/3 pyramidal cells revealed significantly decreased amplitudes of spontaneous inhibitory postsynaptic currents (sIPSCs) in aged AD mice, while the amplitudes of spontaneous excitatory postsynaptic currents (sEPSCs) remained comparable to age-matched wild type controls. Further statistical analysis demonstrated that the reduction in sIPSC amplitudes was caused by the large-amplitude sIPSCs with fast rates of rise, which are characteristic of PV INs. We have also applied a novel approach to determine the E/I ratio, and no change was found in the APP-KI mice. All together, these results could indicate deficits in PV INs, and homeostatic

mechanisms may play a role in maintaining the overall balance of excitation and inhibition in the *App*$^{NL-F}$ mouse model of AD.

Significance statement

Parvalbumin-expressing interneurons (PV INs) play an important role in maintaining normal network activity. In Alzheimer's disease (AD) PV IN dysfunction may lead to epileptiform activity, which is observed both in AD patients and mouse models. With the advantage of the new *App*$^{NL-F}$ mouse model of AD, by analyzing synaptic currents in the pyramidal cells, we have revealed potential PV IN deficits in aged AD mice. Since the *App*$^{NL-F}$ model is generated by an approach that reduces artificial phenotypes possibly existent in previous models, studies on synaptic transmission in this model could further our understanding in the real pathological alterations in AD.

Introduction

Alzheimer's disease (AD) is a neurodegenerative disease that has become a global public health concern with the gradually aging population(Ferri et al., 2005; Mayeux and Stern, 2012). The pathological hallmarks of AD include amyloid β (Aβ) plaques, neurofibrillary tangles (NFTs), and neuronal degeneration (Serrano-Pozo et al., 2011). Among these, a key molecule is Aβ, which is a 40 or 42 amino acid peptide derived from the amyloid precursor protein (APP) after sequential cleavage by β- and γ-secretase. In AD, Aβ can form intermediate soluble oligomers that are synaptotoxic, or insoluble β-sheet amyloid fibrils that are the main component of dense-core plaques(Serrano-Pozo et al., 2011). Pathological levels of Aβ have been shown to

enhance synaptic depression and impair synaptic plasticity at glutamatergic synapses in AD(Walsh et al., 2002; Kamenetz et al., 2003; Hsieh et al., 2006; Roberson et al., 2011; Verret et al., 2012). On the other hand, neuronal hyperactivity, network hyperexcitability, and spontaneous epileptiform activity have been observed in human APP (hAPP) transgenic mouse models with high levels of Aβ(Palop et al., 2007, 2011; Busche et al., 2008; Palop and Mucke, 2009; Harris et al., 2010; Roberson et al., 2011; Yan et al., 2012; Busche and Konnerth, 2016). Moreover, hypersynchronous network activity may contribute to the emergence of AD symptoms such as cognitive impairment in early stages of the disease(Noebels, 2011; Bakker et al., 2012; Scharfman, 2012; Lam et al., 2017). Specifically, electrophysiology studies in hAPPJ20 mice have revealed impaired action potential-driven GABAergic activities resulting from less intrinsic excitability of the GABAergic parvalbumin-expressing interneurons (PV INs)(Verret et al., 2012).

Most of the studies on pathological Aβ and subsequent alterations in synaptic and network activities have been using transgenic mouse models that overproduce mutant hAPP. Although these mouse models simulate several key aspects in human AD(Games et al., 1995; Hsiao et al., 1996; Sturchler-Pierrat et al., 1997; Götz et al., 2004; Cheng et al., 2007; Cissé et al., 2011; Verret et al., 2012), they contain intrinsic problems that may induce artificial phenotypes(Nilsson et al., 2014; Saito et al., 2014; Sasaguri et al., 2017): in these animals, not only Aβ but also other APP fragments are overproduced, which may disrupt intrinsic biological functions; also, utilization of artificial promoters results in transgene expression in cells not necessarily identical to endogenous APP expression. In our studies, we have utilized the App^{NL-F} mouse model of AD, which was generated by manipulating the mouse *App* gene using a knock-in strategy(Nilsson et al., 2014; Saito et al., 2014). Compared to existing hAPP mouse lines, while reliably recapitulating the pathology of human AD, no powerful promoters were introduced to

drive exogenous APP production in the *App*$^{NL-F}$ model, reducing any artificial phenotypes. Therefore, utilization of this new mouse model will advance our understanding of AD pathology.

Here, we have studied potential alterations in synaptic transmission in parietal cortex layer 2/3 pyramidal cells in the *App*$^{NL-F}$ mouse model of AD. The results showed a significant reduction in the average amplitude and average rate of rise of spontaneous inhibitory postsynaptic currents (sIPSCs) in old *App*$^{NL-F/NL-F}$ mice compared to age-matched controls. Moreover, through amplitude distribution analysis, we found that the changes in the amplitude and rate of rise were confined to fast-rising large amplitude sIPSCs but not small ones, indicating potential impairment in perisomatic-targeting PV INs. We have also applied novel quantitative approaches to obtain the memory and burstiness of spontaneous postsynaptic currents (sPSCs) and to calculate an excitation/inhibition (E/I) ratio with higher accuracy that incorporates all properties of sPSCs. All together, these new approaches can further our understanding on the nature of synaptic events, and provide quantitative tools to study synaptic transmission in AD and other disease models.

Materials & Methods

Animal

All animal use was approved by the UCLA Chancellor's Committee on Animal Welfare. *App*$^{NL-F}$ mice (AD) were originally obtained from the research group led by Dr. Takaomi C. Saido at the Laboratory for Proteolytic Neuroscience, RIKEN Brain Science Institute, Saitama, Japan(Nilsson et al., 2014; Saito et al., 2014). Wild-type control mice (WT) were either aged littermates from the *App*$^{NL-F}$ mice breeding, or obtained from the National Institute on Aging. Mice were held in the vivarium on a 12-hour light/dark cycle with free access to water and food.

Electrophysiology

Slice preparation

Mice were anesthetized by isoflurane through inhalation, followed by rapid decapitation. Coronal acute brain slices were prepared on a Vibratome at 350 µm thickness in ice-cold cutting solution (in mM: 135 NMDG, 10 D-glucose, 4 $MgCl_2$, 0.5 $CaCl_2$, 1 KCl, 1.2 KH_2PO_4, 20 HEPES, 3 kynurenic acid; ~20 sucrose to adjust the osmolality; 305-310 mmol/kg; pH = 7.35; bubbled with 100% O_2). Then, slices were kept on a floating mesh platform in a recovery chamber filled with sucrose-based artificial cerebrospinal fluid (sACSF) (in mM: 55 sucrose, 85 NaCl, 25 D-glucose, 2.5 KCl, 1.25 NaH_2PO_4, 0.5 $CaCl_2$, 4 $MgCl_2$, 26 NaHCO3; 300-305 mmol/kg; bubbled with 95%O_2/5% CO_2). The recovery chamber was kept in 34°C water bath for 30 min and then moved to room temperature.

Whole-cell recording

For whole-cell recording, artificial cerebrospinal fluid (ACSF) was used (in mM: 126 NaCl, 10 D-glucose, 2 MgCl2, 2 CaCl2, 2.5 KCl, 1.25 NaH2PO4, 1.5 sodium pyruvate, 1 L-glutamine; 295-300 mmol/kg; bubbled with 95%O_2/5% CO_2). Acute brain slices were placed in a submerged chamber filled with ACSF at a flow rate of 6-7 ml/min and a temperature of 32-34 °C. An intracellular solution (in mM: 140 Cesium Methanesulfonate, 5 CsCl, 2 $MgCl_2$, 2 Na-ATP, 2 Na-GTP, 200 µM EGTA, 10 HEPES; 275-280 mmol/kg; pH = 7.35) was used for the recording of spontaneous synaptic events.

Data acquisition and analysis

Spontaneous excitatory and inhibitory postsynaptic currents (sEPSCs and sIPSCs) were recorded at a holding voltage of -60 mV and 0 mV, respectively, using an Axopatch 200B amplifier (Axon Instruments, Inc.). All recordings were low-pass filtered at 1.5 kHz and digitized at a sampling frequency of 10 kHz, then recorded using a custom-written LabVIEW-based software (EVAN). Spontaneous events were detected with EVAN for the analysis of frequency and amplitude. The measurement of phasic discharge for the E/I ratio calculation was done using Igor Pro 6 (WaveMetrix, Inc.). Other analyses on the synaptic events were done in Excel 2011 (Microsoft Corporation) with customized and built-in functions. Nested one-way ANOVA test was used to analyze E/I ratio differences, and it was done with an Excel spreadsheet from an online source (http://www.biostathandbook.com/nestedanova.html). All other statistical tests were done in Prism 6 (GraphPad Software, Inc.) by using non-parametric Mann-Whitney test or paired Wilcoxon test, and $p<0.05$ was considered to be statistically significant. All the group statistics are presented as mean ± SEM (standard error of mean).

Separating small and large events

In order to identify the large amplitude sEPSC and sIPSC events from all detected synaptic events, we used an approach that could objectively calculate a threshold for large events based on the amplitude distribution of all events from a cell. The cumulative distribution of all amplitudes was plotted and fitted with either one or two cumulative normal distributions using the NORM.DIST function in Excel (**Fig. 2a**).

The goodness of the two fits was compared with an F-test. The F value was calculated as:

$$\frac{\frac{(RSS_1 - RSS_2)}{(p_2 - p_1)}}{\frac{RSS_2}{(n - p_2)}} \qquad \text{(Eq. 1)}$$

In Eq. 1, RSS_1 and RSS_2 are the residual sum of squares when fitting with one and two distributions, respectively; p_1 and p_2 are the number of parameters used for fitting with one and two distributions, respectively; and n is the number of data points used for fitting. Then, a *p*-value was calculated using the F.DIST function in Excel. For all the recordings in both groups, the *p*-values approached 0, indicating that two distributions always fit the cumulative curves significantly better than one distribution. Next, a threshold for detecting large PSCs was chosen as the x-value (amplitude) that corresponds to the y-value (cumulative distribution) where the first distribution ends (**Fig. 2a**; y-value indicated on the y-axis by the horizontal dashed line; x-value, which is the threshold, indicated on the x-axis by the vertical dashed line).

Burstiness and memory calculation

The inter-event intervals (IEIs) of synaptic events were measured as the time difference between two adjacent PSCs. Then, burstiness and memory of these events were calculated with equations in previous published papers(Goh and Barabási, 2008; Schleiss et al., 2016):

$$B = \frac{\sigma - \mu}{\sigma + \mu} \qquad \text{(Eq. 2)}$$

$$M = \rho_{IEI}(1) \qquad \text{(Eq. 3)}$$

In Eq. 2, B is burstiness; and σ and μ are the standard deviation and mean of the IEIs, respectively, of each cell. In Eq. 3, M is memory; and $\rho_{\mathrm{IEI}}(1)$ is the Spearman rank auto-correlation of the IEI array at a lag of 1.

Calculation of E/I ratio

Measurement of phasic charge

We have previously described an approach to objectively measure the tonic and phasic components of inhibitory or excitatory events(Glykys and Mody, 2007). This method does not

rely on subjective thresholds to detect spontaneous events. For the analysis of E/I ratio based on this approach, the raw recording traces of certain durations was analyzed. Using a custom Igor written procedure, an all-point histogram (Bin width=1 pA) was plotted for segments of 15 s from either sEPSC or sIPSC recording and smoothed by Savitzky-Golay algorithm (2^{nd} order 17 points smoothing) to obtain the peak value. This histogram was always skewed to one side by the presence of spontaneous synaptic events. The non-skewed side of the histogram was fitted with a Gaussian distribution from the end of the non-skewed side to 95% of the peak value over the peak to the skewed side. The mean of this fitted Gaussian distribution was considered to be the mean holding current. Then, this Gaussian curve was mirror-imaged to the skewed side, and the area between the Gaussian distribution and the all-point histogram divided by the total number of points in this area was considered to be the mean phasic charge (in pC). The E/I was determined as the ratio between the excitatory and the inhibitory phasic charges over 15 s recordings. For each cell, we have randomly selected 10 segments from sEPSC and sIPSC recording (see below for details), and obtained 100 E/I values.

Driving forces for sEPSCs and sIPSCs

To get a more accurate measurement of the E/I ratios, we have also taken the driving force for sEPSCs and sIPSCs into account. The holding voltages for recording sEPSCs and sIPSCs were -60 mV and 0 mV, respectively. The reversal potentials of the currents activated by AMPA and NMDA are close to 0 mV, and that calculated for the GABA receptors is approximately -70mV. Therefore, at V_h=-60 mV, the driving forces for sEPSCs and sIPSCs were about 60 mV and 10 mV, respectively; whereas at V_h=0 mV, the driving forces for sEPSCs and sIPSCs were about 0 mV and 70 mV, respectively. At V_h=-60 mV where sEPSCs were recorded, it is possible that the recordings were contaminated with small outward sIPSCs. Because this contamination should be absent in picrotoxin (PTX), for some recordings at V_h=-60 mV, we plotted the all-point histograms of one randomly chosen 15 s segment before and one after washing in 50 μM PTX.

We then compared the standard deviation (σ) of the Gaussian fits of the outward currents (non-skewed sides, as described above) of the two histograms. A significant amount of small contaminating sIPSCs in the sEPSC recording would significantly decrease the σ after PTX. In total, we've got 3 WT and 7 AD cells with PTX wash in at -60 mV, and the variance before and after PTX were not significantly different in these 10 cells (WT: σ=3.92 vs. 3.79; p=0.75; AD: σ= 2.54 vs. 3.06; p=0.22; before vs. after PTX; Wilcoxon paired test). Therefore, there was no detectable contamination of small outward sIPSCs in our sEPSC recordings at V_h=-60 mV.

Determination of sample size

With the approach above, we can get the phasic charge by randomly choosing *m* segments from sEPSC recording and *n* segments from sIPSC recording for each cell, and then get *m* × *n* E/I ratios. To determine the minimum *m* and *n* value needed to get the best estimation of the real population E/I value, we used the equation described in a previously published paper(Eckblad, 1991) for estimating the fractional deviation of the sample mean from the real population mean:

$$Fractional\ deviation = \frac{t \times \sigma}{\mu \times \sqrt{N}} \qquad \text{(Eq. 4)}$$

In Eq. 4, *t* is the value from a Student's *t*-distribution with a degree of freedom equal to one less than the sample size and with a 95% confidence interval; σ is the sample standard deviation; *μ* is the sample mean; and *N* is the sample size.

Firstly, we have determined a way to randomly select segments of recording from a trace. Random integer numbers between the start and end time (in s) of the recording were generated successively using the RNADBETWEEN function in Excel, and the random numbers will be used as the start time of different segments. If two segments had an overlap, then the start time

of the latter-generated segment was regenerated. If one segment ran into the seal test period, the start time was also regenerated. In this way, we have randomly selected 10 segments of 15 s from sEPSC and sIPSC recording for each cell, yielding 100 E/I ratios (N=100). We then randomly selected different number of values (N=10, 20, 30, …, 90) from these 100 values for calculating the σ and μ of different sample sizes. With Eq. 4 we calculated the fractional deviation of different sample sizes (N=10, 20, …, 100) for each cell (sample cell in **Fig. 6a**, dots). We also calculated the fractional deviation using the σ and μ of N=100 for all sample sizes and estimated the fractional deviation of more sample sizes (sample cell in **Fig. 6a**, line, N=2-150, and N is integer). With this approach applied to every cell, we found that when N=100, the fractional deviation of the sample mean from the real population mean reached a sufficiently low level (~12%; see **Results** and **Fig. 6b**). Therefore considering the accuracy of estimating the real E/I ratio and the convenience of choosing samples, we decided to choose 10 segments from sEPSC recording and 10 from sIPSC recording, thus obtaining all possible 100 E/I values for each cell.

Statistical test for phasic charges and E/I ratios

Since we have recordings from different animals, and for each animal we had recording(s) from one or multiple cells, we want to take all variables into account when we compare the Es and Is as well as the E/I ratios between groups. Therefore, we decided to use a nested one-way ANOVA to determine the difference between the WT and AD group. The test was done using an Excel spreadsheet from an online source (http://www.biostathandbook.com/nestedanova.html). Briefly, there were groups (WT and AD), subgroups (for a 2-level nested ANOVA), and sub subgroups (for a 3-level nested ANOVA) in this test. The phasic E and I charges of WT and AD cells were compared by a 2-level nested one-way ANOVA, in which each animal was treated as a subgroup, and the average of the 10 Es and 10 Is of each cell from this animal was listed as values within the subgroup. Then, the *p*-

values of the difference between groups (WT and AD) as well as among subgroups within each group (6 and 8 mice in the WT and group, respectively) were calculated. The E/I ratios of WT and AD cells were compared by a 3-level nested one-way ANOVA, because we did not want to use the average of 100 E/I ratios as a single value for each cell and lose the accuracy (see the determination of sample size). Therefore, besides groups (WT and AD) and subgroups (different animals), there were also sub subgroups, which are different cells from each animal, and then the 100 E/I ratios were listed as values within the sub subgroups. Similarly, the *p*-values of the difference between groups (WT and AD), among subgroups within each group (6 mice in the WT group; 8 mice in the AD group), as well as among sub subgroups within each subgroup (9 and 12 cells in the WT and AD group, respectively) were calculated.

Results

Reduced sIPSC amplitudes in App^{NL-F} mice.

Previous studies have shown altered glutamatergic and GABAergic transmission in parietal cortex in various mouse models of AD(Busche et al., 2008; Roberson et al., 2011; Verret et al., 2012; Hazra et al., 2013; Perez et al., 2016). We wanted to investigate whether there are alterations in excitatory and inhibitory synaptic transmission in the *App^{NL-F}* mouse model of AD. We have recorded sEPSCs and sIPSCs (See **Method**; **Fig. 1a**) in parietal cortex layer 2/3 pyramidal cells in both wild-type control (WT) and *App^{NL-F}* homozygous (AD) mice. The average ages were comparable between the two groups (20.5±3.2 vs. 18.3±2.2 months; n=6 vs. 8 mice; WT vs. AD; p=0.5088; Mann-Whitney test). For each cell we analyzed the same number of consecutively occurring sEPSCs or sIPSCs. The events were randomly chosen from all detected events throughout the whole recording period (12 cells for each group; 161 sEPSCs and 626 sIPSCs for each cell). The average frequencies of both sEPSCs and sIPSCs remained unchanged in the AD mice (sEPSC frequency=7.42±0.97 vs. 5.79±1.08 Hz, p=0.2415; sIPSC

frequency=11.10±0.99 vs. 9.91±0.98 Hz, p=0.2415; WT vs. AD; Mann-Whitney test, **Fig. 1b**). The average amplitude of sIPSCs was significantly reduced while that of sEPSCs remained constant in the AD animals (sEPSC amplitude=25.97±1.52 vs. 23.39±1.07 pA, p=0.1432; sIPSC amplitude=51.55±5.16 vs. 37.06±2.50 pA, p=0.0145; WT vs. AD; Mann-Whitney test, **Fig. 1c**).

The reduction of sIPSC amplitudes in App^{NL-F} mice was caused by a decrease in large amplitude events

The presence of large amplitude events during sIPSC recording led us to further investigate whether small and large events contributed differently to the overall changes in the amplitudes of sPSCs. We were specifically interested in analyzing the large sIPSCs because they potentially originate from perisomatic-targeting PV INs which generate strong inhibition on postsynaptic neurons(Freund and Katona, 2007). Since previous research has shown a deficiency in the intrinsic excitability of GABAergic PV INs in hAPPJ20 mouse model of AD(Verret et al., 2012), we wanted to examine whether the reduction in the sIPSC amplitudes we observed could be related to PV IN dysfunction in the novel *App^{NL-F}* AD model.

In order to study the small and large sPSCs separately, we first tested whether the events could be objectively divided into two groups (see **Method**). We found that the cumulative amplitude distributions of all sPSCs for each individual cell could be significantly better fitted by two cumulative normal distributions rather than one, as indicated by an F-test (see **Method**; data not shown), thus sPSCs in all cells could be separated into two groups according to their amplitudes (**Fig. 2a**). Based on the fitted curve, we chose to use the value on the X-axis (amplitudes) corresponding to the end of the first distribution on the Y-axis (cumulative probability) as the threshold for large events (A_{th}, **Fig. 2a**). Then, sPSCs larger than A_{th} were classified as large events, while those smaller than A_{th} were considered as small events. The averaged A_{th} for sEPSCs was comparable between WT and AD, while for sIPSCs the averaged A_{th} was

significantly decreased in AD mice (sEPSC A_{th}=23.75±0.96 vs. 22.18±0.75 pA, p=0.1735; sIPSC A_{th}=41.64±3.14 vs. 33.24±1.64 pA, p=0.0332; WT vs. AD; Mann-Whitney test; **Fig. 2b**), which is consistent with the reduced amplitude of sIPSCs (**Fig. 1c**).

From the cumulative distribution curves of all sPSCs detected from all cells in WT and AD mice, qualitatively the amplitude distribution of sEPSCs were close between WT and AD group, while the distribution curve of sIPSCs of AD mice were significantly left-shifted compared to that of WT mice (**Fig. 3a**), which is consistent with a decreased average sIPSC amplitude in AD animals (**Fig. 1c**). Moreover, the two curves of sIPSC amplitudes became further separated when the events were larger than A_{th} (arrow heads, **Fig. 3a**), revealing a more significant reduction in large sIPSCs than in small sIPSCs. When small and large events were analyzed separately, the amplitudes of both large and small sEPSCs remained constant (small sEPSC amplitude=17.80±0.48 vs. 17.60±0.41 pA, p=0.7987; large sEPSC amplitude=37.90±3.52 vs. 30.81±1.43 pA, p=0.1135; WT vs. AD; Mann-Whitney test; **Fig. 3b, c**), which is consistent with the unchanged overall sEPSC amplitude (**Fig. 1c**). For sIPSCs, the amplitude of large sIPSCs was decreased in AD mice while that of the small sIPSCs remained unchanged (small sIPSC amplitude=28.35±1.54 vs. 24.07±1.00 pA, p=0.0519; large sIPSC amplitude=95.36±13.81 vs. 57.31±7.27 pA, p=0.0284; WT vs. AD; Mann-Whitney test; **Fig. 3b, c**), consistent with a decrease in the overall sIPSC amplitude (**Fig. 1c**) and the trend in the distribution curves (**Fig. 3a**).

Therefore, we have revealed that there are two populations in all sPSCs, and that they can be separated by an objectively calculated amplitude threshold. Further, we have demonstrated that the decrease in the overall sIPSC average amplitude was primarily contributed by the large events rather than the small ones, which is consistent with our PV IN dysfunction hypothesis in the *App*$^{NL-F}$ mice.

Rates of rise of sIPSCs were decreased in App^{NL-F} mice.

The decreased amplitudes of large sIPSCs in *App^{NL-F}* mice is consistent with a PV-IN dysfunction. However, the origin of the large sIPSCs needs to be further analyzed, since they may be a summation of multiple events(Williams et al., 1998), or they could be generated by other types of perisomatic-targeting interneuron(Freund and Katona, 2007). Since PV-INs target the α1 subunit-containing $GABA_A$ receptors, they mainly generate fast-rising postsynaptic currents(Thomson et al., 2000; Nyíri et al., 2001; Klausberger et al., 2002). In order to further elucidate the origination of the large sIPSCs, we also examined the rate of rise of the synaptic currents. We defined the rate of rise (RR) of an event as the ratio between 80% of the peak amplitude and RT 10-90%, which is the time it takes for the current to rise from 10% to 90% of the peak amplitude (**Fig. 4a**). Thus, the rate of rise of an event is the slope of the main rising phase, and indicates how fast an event rises to its peak. We found that the RRs of sEPSCs was unchanged in the AD group, while those of sIPSCs was significantly decreased in AD animals (sEPSC RR=24.92±1.41 vs. 29.33±3.37 pA/ms, p=0.5137; sIPSC RR=49.82±3.62 vs. 33.63±5.06 pA/ms, p=0.0100; WT vs. AD; Mann-Whitney test; **Fig. 4b**).

When we separated the events based on their amplitudes into small and large ones, the results showed that the RRs of small sEPSCs were comparable to those of the large ones for both WT and AD mice (p=0.6707, WT; p=1432, AD; Mann-Whitney test). Whereas for sIPSCs, the RRs of large events were significantly higher than those of the small ones in both groups (p<0.0001, WT; p=0.0029, AD; Mann-Whitney test). These results are consistent with the idea that large amplitude sIPSCs comprise events originating from soma-innervating PV INs that synapse onto α1 subunit-containing $GABA_A$ receptors. Furthermore, the RRs of both small and large sEPSCs were comparable between WT and AD group (small sEPSC RR=24.07±1.63 vs. 24.47±2.56 pA/ms, p=0.7987; large sEPSC RR=25.76±1.64 vs. 34.18±4.49 pA/ms, p=0.3474; WT vs. AD;

Mann-Whitney test; **Fig. 4c, d**). For sIPSCs, while the RRs of the small events were similar, those of the large events were significantly decreased in AD mice (small sIPSC RR=24.97±2.55 vs. 22.21±1.33 pA/ms, p=0.6707; large sIPSC RR=74.67±7.47 vs. 45.06±9.27 pA/ms, p=0.0083; Mann-Whitney test; **Fig. 4c, d**), indicating again that the changes in large amplitude and fast-rising sIPSCs led to the overall reduction of RRs in AD mice.

In conclusion, our results from analyzing the RR further indicated that the large sIPSCs could be generated by soma-targeting PV INs according to their fast rising phase. Moreover, the reduction in the overall rates of rise in AD cells is contributed by large events but not the small ones, which is again consistent with a PV IN dysfunction.

Burstiness and memory of spontaneous postsynaptic currents

Besides analyzing the frequency and amplitude of sEPSCs and sIPSCs, we also wanted to investigate whether there are specific firing patterns within those events, such as bursts. In order to examine the burstiness of sPSCs on pyramidal cells in WT and AD mice, we first determined the inter-event intervals (IEIs) of all sPSCs as well as those of the large sPSCs. Then, we used previously described methods to quantitatively determine the burstiness (B) and memory (M) in the firing of a single cell(Goh and Barabási, 2008; Schleiss et al., 2016) (See **Method**). By default, the values of both burstiness and memory will be within the range (-1, 1). For burstiness, a value closer to 1 (i.e., when STD is very large) means the firing pattern is more "bursty", while a value closer to -1 (i.e. when STD → very low) indicates a more regular firing pattern. In between, a Poisson process will result in a burstiness value of 0. For memory, a positive value means that short IEIs tend to be followed by short IEIs and long IEIs by long IEIs, whereas a negative value means that short IEIs tend to be followed by long IEIs or vice versa. A value near 0 indicates no memory in the system.

The results from burstiness analysis showed that for sEPSCs and sIPSCs in both WT and AD cells, the average values were all negative (B_{EPSC_WT}=-0.19±0.04; B_{IPSC_WT}=-0.35±0.04; B_{EPSC_AD}=-0.13±0.04; B_{IPSC_AD}=-0.31±0.04), indicating that the occurrence of sPSCs was more regular than bursty. Also, there was no significant difference in burstiness either for sEPSCs or for sIPSCs between WT and AD cells (data not shown). However, when we compared the burstiness of small events versus that of large events, we found that in general, small sPSCs had more negative B values than large sPSCs for both WT ($B_{Small\ EPSC}$ =-0.06±0.03 vs. $B_{Large\ EPSC}$=-0.01±0.03; $B_{Small\ IPSC}$=-0.14±0.02 vs. $B_{Large\ IPSC}$=-0.08±0.02; **Fig. 5a**) and AD ($B_{Small\ EPSC}$ =-0.05±0.02 vs. $B_{Large\ EPSC}$=-0.01±0.02; $B_{Small\ IPSC}$=-0.12±0.02 vs. $B_{Large\ IPSC}$=-0.07±0.02; **Fig. 5a**) mice, and that difference was significant for sEPSCs of both WT and AD cells (p=0.0425 for WT; p=0.0425 for AD; Wilcoxon paired test; **Fig. 5a**) and for sIPSCs of AD cells only (p=0.0522 for WT; p=0.0122 for AD; Wilcoxon paired test; **Fig. 5a**). These results indicate that for both sEPSCs and sIPSCs, the small events occurred regularly throughout the recordings, while the large events were generated in a more random pattern. For memory, the averaged memory for all sEPSCs and all sIPSCs was close to 0 (M_{EPSC_WT}=0.07±0.02; M_{IPSC_WT}=0.03±0.01; M_{EPSC_AD}=0.08±0.02; M_{IPSC_AD}=0.06±0.02), indicating that there is little memory in the system. Also, there was no significant difference in memory either between small and large events or between WT and AD groups (data not shown).

According to the original study (Goh and Barabási, 2008), the “burstiness” of a system can have two qualitatively different origins, which are presented by parameters B and M described above. Therefore, it is helpful to place B and M values in a *(B, M)* space which can give an intuitive presentation of certain properties of a system, which, in our case, is the pattern of incidence of sPSCs (**Fig. 5b**). From the *(B, M)* plots of cell averaged memory and burstiness of sEPSCs and sIPSCs in WT and AD group, it is evident that both currents lack memory and are not “bursty”. On the contrary, the sPSCs appeared to emerge in a rather regular pattern.

A novel approach for determining the synaptic E/I ratio

A proper balance between excitation (E) and inhibition (I) is difficult to define consistently under all circumstances(Isaacson and Scanziani, 2011), but it is considered to be crucial for a normal circuit function. Studies have shown that a disrupted E/I balance can cause network dysfunction and various diseases(Fernandez et al., 2007; Kehrer et al., 2008; Gogolla et al., 2009), including AD(Schmitt, 2005; Rissman and Mobley, 2011; Busche and Konnerth, 2016). Therefore, after examining the excitatory and inhibitory currents separately in pyramidal cells, we also wanted to check whether the E/I balance is altered in the App^{NL-F} mice. Previous methods have been using multiple indices to calculate the E/I ratio, such as the peaks, charges(Bartley and Dobrunz, 2015) and conductance(Wehr and Zador, 2003; Cruikshank et al., 2007) of postsynaptic currents. These existing methods usually use only one averaged property of the events, and they usually acquire the E and I value over a short period of recording. Here, we introduce a new approach, which can incorporate all properties of sPSCs into a single index and is calculated multiple times over a long duration of recording to determine the E/I ratio.

Our previous work has described a method to objectively separate the tonic and phasic components from raw electrophysiological recordings(Glykys and Mody, 2007) (See **Method**). There are several advantages of using this method to determine the phasic E and I exerted onto a cell: firstly, no subjective thresholds are needed to detect spontaneous events, and tonic and phasic activities are separated objectively according to the all-point histograms of raw recording traces; secondly, the values of E and I depend on all properties of the phasic currents, such as frequency, amplitude, charge, etc.; and thirdly, it allows the selection of multiple segments from the entire recording and acquire a vast number of E/I values.

We decided to randomly choose *m* segments from sEPSC recordings (E) and *n* segments from sIPSC recordings (I) for each cell, and each segment with a duration of 15 s. Then, we will have *m* E and *n* I values, resulting in *m* × *n* E/I ratios. In order to determine the proper values for *m* and *n*, we did a sample size analysis using a previously described method(Eckblad, 1991) (See **Method**). The fractional deviation of the sample mean from the real population mean is negatively correlated with the sample size (**Fig. 6a**). For the cell shown in **Fig. 6a**, when the number of E/I ratios reached 100, the fractional deviation decreased to 0.09, which means that the sample mean is ±9% within the real population mean. Next we did the same analysis for each cell in the WT and AD groups. The results showed that when calculating 100 E/I ratios, the accuracy in predicting the real population mean would be sufficiently low (F_{WT}=0.12±0.02 vs. F_{AD}=0.12±0.01, p>0.9999; n=9 vs. n=12; WT vs. AD; Mann-Whitney test; **Fig. 6b**). Therefore, for each cell, we decided to randomly select 10 segments of 15 s from both the E and I raw recording traces, thus obtaining 10 E and 10 I values and 100 E/I ratios for one cell (**Fig. 6c**).

We first examined the phasic E and I values in WT and AD cells. As described above, each group there will be *N* × *10* values of E and I, in which *N* is the number of cells in each group (N_{WT} = 9; N_{AD}=12). Considering that these values were collected from different animals (6 and 8 mice in the WT and group, respectively) and different cells (9 and 12 cells in the WT and AD group, respectively), besides comparing the average of all values in each group, we also included the variance among different animals and cells into the analysis. Therefore, we decided to use a 2-level nested one-way ANOVA test (see **Method**). The results showed that there was no significant difference either between groups (p_{Es}=0.1276; p_{Is}=0.2602; WT vs. AD), or among subgroups within each group (p_{Es}=0.2080; p_{Is}=0.0973; among animals). The results from analyzing detected PSCs indicated a significant difference in the average sIPSC amplitude but not the average sEPSC amplitude between groups (**Fig. 1c**). The absence of significance in the phasic I charge analysis may be caused by the large variance among subgroups, i.e. among

different animals (31.98% and 52.83% of total variance, Es and Is, respectively), as well as within subgroups, i.e. among different cells (53.15% and 44.70% of total variance, Es and Is, respectively). In comparison, the variance between the WT and AD group was smaller (14.87% and 2.47% of total variance, Es and Is, respectively). Moreover, in the phasic charge analysis, when there were no subjective detection thresholds chosen, many more very small events (below detection threshold) contributed to the phasic component of a recording. As we have shown above, the large events but not the small ones contributed to the overall difference in amplitudes (**Fig. 3b, c**) as well as rates of rise (**Fig. 4c, d**) between groups. Therefore, the considerably more small events below detection threshold contributing to the phasic charge resulted in the overall unchanged phasic E and I; however in the histograms of all the values we could see a left-shift in both Es and Is in the AD group (**Fig. 7a**).

For the calculation of the E/I ratio, firstly we've taken into account the driving forces for sEPSCs and sIPSCs. In our recording scenario, the driving forces for sEPSCs and sIPSCs were about 60 mV and 70 mV, respectively (See **Method**). Therefore to counterbalance the difference in driving forces, the E/I ratio was determined as $(7\times E)/(6\times I)$. To compare the E/I ratio between WT and AD animals, we chose to use a 3-level nested one-way ANOVA test (see **Method**), because now we want to use all the 100 E/I ratios for a higher accuracy, there was an extra level, sub subgroups, which were different cells from each animal. Then, the 100 values from each cell were listed under each sub subgroup. As a result of the unchanged phasic E and I values, the E/I ratio remained constant in the AD group as well (E/I=0.54±0.02 vs. 0.47±0.02, p=0.3882), although there was a left-shift in the histogram of all E/I ratios in the AD group (**Fig. 7b**). Another reason that might result in the unchanged E/I ratio might be the large variance among different animals and cells. As an example, in the AD group, the E/I ratios varied a lot from animal to animal as well as among different cells in the same animal (**Fig. 7c**).

Discussion

We investigated synaptic alterations by analyzing spontaneous postsynaptic currents in parietal cortex layer 2/3 pyramidal cells in the *App*$^{NL-F}$ mouse model of AD. We found that while the properties of small sIPSCs and all sEPSCs remained constant, the amplitudes of large and fast-rising sIPSCs were reduced in AD mice, which is consistent with a PV IN dysfunction hypothesis. We have also used a novel method to determine the E/I ratio with a high accuracy. Owing to the large variance among different animals and cells, we found no significant alteration in the overall E/I ratio in AD mice. It remains to be determined whether homeostatic mechanisms or experimental conditions are responsible for the unchanged E/I ratio in *App*$^{NL-F}$ mice.

hAPP mouse lines are widely used experimental models of AD to study cerebral Aβ amyloidosis as well as synaptic, network and behavioral dysfunctions(Götz and Ittner, 2008; LaFerla and Green, 2012). However, the overexpression of hAPP may introduce physiological and behavioral artifacts due to the production of various APP fragments and the use of exogenous promoters to drive the expression of hAPP(Sasaguri et al., 2017). In our study we used the *App*$^{NL-F}$ mouse model, which was generated by a gene knock-in approach(Nilsson et al., 2014; Saito et al., 2014) with no hAPP overexpression. While having excessive production of Aβ, especially aggregation-prone Aβ_{42}, these mice do not express either exogenous promoters or hAPP, which could reduce the artificial phenotypes observed in hAPP-overexpressing mice(Saito et al., 2016; Sasaguri et al., 2017). In this knock-in AD model, we investigated the postsynaptic currents in parietal cortex, in which region altered synaptic transmission and aberrant network activities were observed in hAPP mice(Roberson et al., 2011; Verret et al., 2012) and atrophies and hypoperfusion were observed in AD patients(Jacobs et al., 2011, 2012).

The reduction in the overall average amplitude of the sIPSCs in the AD mice, but not that of the sEPSCs, was caused by a decrease in the average amplitude of the large sIPSCs but not the small amplitude ones. Moreover, large sIPSCs had significantly faster rates of rise than small ones, and this high rate of rise of the large sIPSCs was reduced in AD mice. These alterations are consistent with a possible PV IN dysfunction in these *App*$^{NL-F}$ mice, because PV INs target α1 subunit-containing $GABA_A$ receptors on the somatic and perisomatic compartments of their postsynaptic targets, thus generating fast-rising sIPSCs with large amplitudes(Thomson et al., 2000; Nyíri et al., 2001; Klausberger et al., 2002; Freund and Katona, 2007).

Altered PV IN inhibition on pyramidal cells is closely linked to network oscillations and cognitive functions. Network hyperexcitability and epileptiform events have been observed in most mouse models of AD(Palop et al., 2007, 2011; Busche et al., 2008; Palop and Mucke, 2009; Harris et al., 2010; Roberson et al., 2011; Yan et al., 2012; Busche and Konnerth, 2016) and in AD patients using high resolution recordings(Lam et al., 2017). Hypersynchronous network activities have been shown to emerge during reduced gamma oscillation, which is a high frequency rhythm that depends on the activities of fast-spiking PV INs and contributes to cognitive functions(Cardin et al., 2009; Sohal et al., 2009; Buzsáki and Wang, 2012; Sohal, 2012; Cho et al., 2015). Specifically, PV IN defects due to a reduced expression of voltage-gated sodium channels Nav1.1 were found in hAPPJ20 mice, and reversing the Nav1.1 reduction by Nav1.1-BAC bacterial rescued PV IN synaptic currents and gamma oscillations and reduced network hypersynchrony and memory deficits in these mice(Verret et al., 2012). A recent study showed that there was no change in the overall Nav1.1 level in either APP-overexpressing or *App*$^{NL-F}$ mice brain homogenates, suggesting that Nav1.1 downregulation may be a phenotype unique to the hAPPJ20 mice(Saito et al., 2016). However, the fraction of PV IN in brain homogenates may be too small to detect changes in this specific population of interneurons. Therefore, a PV IN

specific reduction of Nav1.1 may still be present in *App*$^{NL-F}$ mice. Our results based on rigorous sIPSC analyses are consistent with this possibility. Further studies on the functioning of PV INs in this model are needed, and research on network activities and related cognitive functions could reveal new phenotypes beyond those observed in the hAPP mice.

In our endeavor to thoroughly study synaptic changes in the cortices of *App*$^{NL-F}$ mice we developed reliable and objective methods to analyze spontaneous synaptic events. One key element of our approach was to avoid using subjective and randomly chosen thresholds. For the separation of small and large synaptic events, we used the cumulative distribution of all of the event amplitudes to determine the threshold of separation between small and large amplitude events. For obtaining the E/I ratio, we used the all-point histogram and Gaussian fits to calculate the phasic charges, where no subjective thresholds were needed for the detection of synaptic currents. While it is considered to be crucial for a normal circuit function, the E/I ratio remains difficult to define consistently under all circumstances(Isaacson and Scanziani, 2011). Existing methods have used one or multiple parameters of mainly stimulus-evoked postsynaptic currents, such as peak amplitudes and charges, over short periods of recording to determine the E/I ratio(Wehr and Zador, 2003; Cruikshank et al., 2007; Bartley and Dobrunz, 2015). Considering potential drawbacks of these methods, we developed an approach which could (1) incorporate all properties of the postsynaptic currents such as frequency, amplitude, charge, etc., and (2) increase the accuracy of E/I calculation by including multiple segments over a relatively long period recording (4-6 min) since the E/I balance is constantly changing in the brain. In the *App*$^{NL-F}$ mice, using our new approach, the E/I ratios were not significantly altered compared to controls, neither were the phasic E and I charges. The main reason for the phasic I charge being unchanged while detected sIPSC amplitudes being reduced could be that the former was actually incorporating very small currents that remained undetected with traditional thresholding. Inclusion of these events may have weakened the effect of large sIPSCs on reducing the overall

sIPSC amplitudes in AD mice. Thus, the unchanged phasic E and I charges resulted in an unchanged E/I ratio. It is also possible that there were compensatory mechanisms taking place in the AD brain to counterbalance the outcomes of decreased inhibition. This possibility will require further investigation. The large variance among different animals and cells when measuring the E/I ratios with our method has to be noted. This could be a result of us choosing multiple segments over long recording durations and the dynamic nature of the E/I balance in the brain. Our E and I recordings were done at different time points at distinct holding voltages. Although we have corrected for the different driving forces, other conditions might be varied when recording E and I. Future analysis using this method should measure E and I at an intermediate voltage (between E_{gaba} and $E_{glutamate}$) at the same time in order to control these variations.

Studying abnormal synaptic transmission and related aberrant network activities and cognitive deficits in mouse models of AD have valuable translational implications for human AD research. Epilepsy with clinical seizures are particularly more prevalent in sporadic and familial AD patients at younger ages, while overt seizures are not reported in most AD cases(Scarmeas et al., 2009). Therefore, it remains difficult to study potential epileptiform activities in patients with conventional EEG electrodes because the abberant activity takes place in deep temporal structures. A recent study using foramen ovale electrodes positioned adjacent to the mesial temporal lobe revealed clinically silent hippocampal seizures and epileptiform spikes during sleep, a period especially important for memory consolidation(Lam et al., 2017). In urethane-anesthetized App^{NL-F} mice, abnormal gamma oscillations were observed in the entorhinal cortex, including reduced theta-gamma coupling and impaired phase-locking of layer 2/3 pyramidal cell spiking activities(Nakazono et al., 2017). Since PV INs are essential for generating gamma oscillations and for suppressing hypersynchronous network activity, an impairment in PV IN function shared among different mouse models of AD and present during

the initial stages of the disease, may have highly relevant clinical and therapeutic consequences. The development of specific Na^+ channel modulators is an obvious start in this direction(Anderson et al., 2017; Frederiksen et al., 2017).

Figures

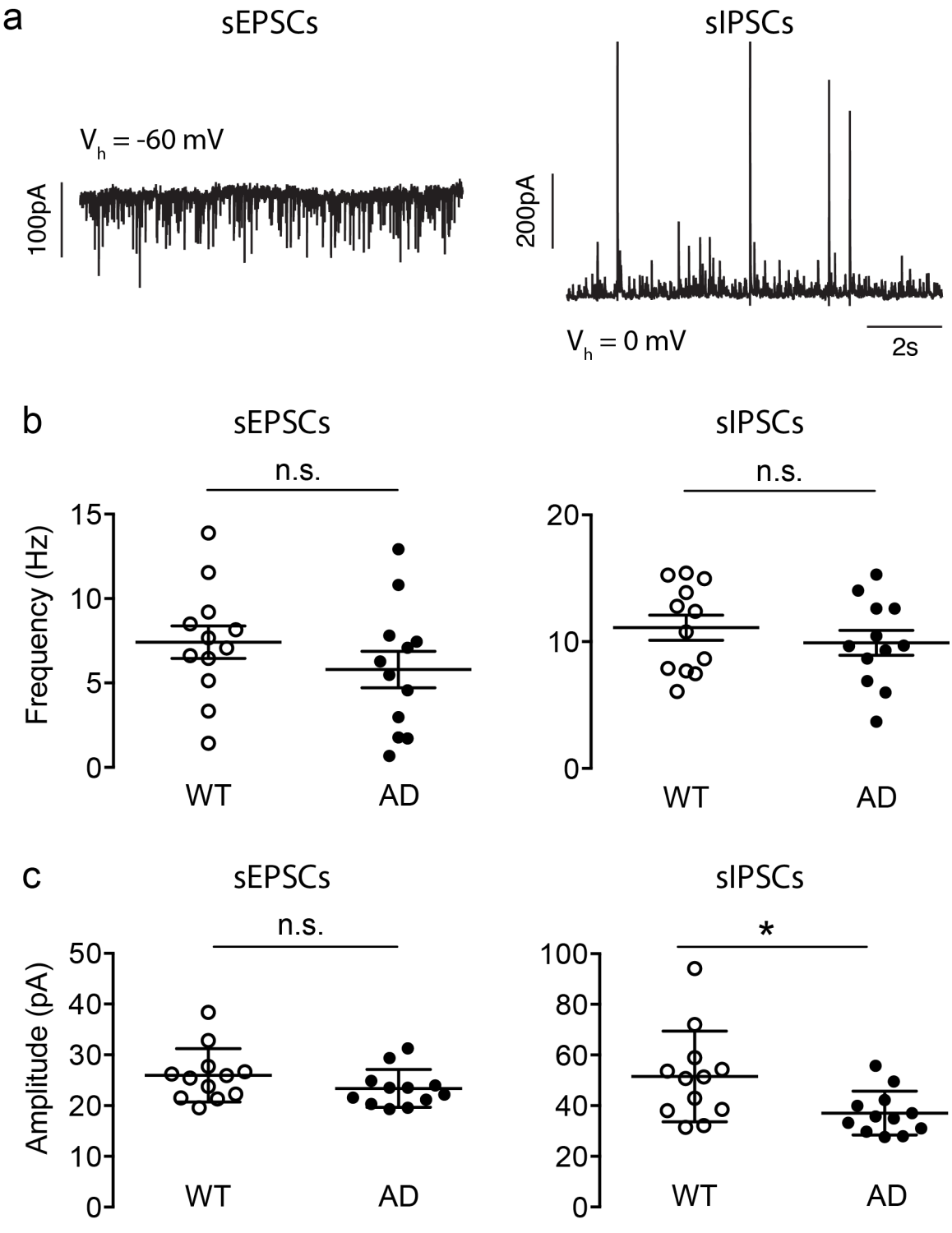
a
sEPSCs
sIPSCs
V_h = -60 mV
100pA
200pA
V_h = 0 mV
2s
b
sEPSCs
sIPSCs
n.s.
n.s.
Frequency (Hz)
15
10
5
0
20
10
0
WT
AD
WT
AD
c
sEPSCs
sIPSCs
n.s.
*
Amplitude (pA)
50
40
30
20
10
0
100
80
60
40
20
0
WT
AD
WT
AD

Figure 1. The average amplitude of sIPSCs was reduced in AD pyramidal cells. (**a**) Example raw recording traces of sEPSCs (left) and sIPSCs (right), with a holding voltage (V_h) of -60mV and 0mV, respectively. (**b**) The average frequency of either sEPSCs (left) or sIPSCs (right) remained unchanged in the AD group. (**c**) The average amplitude of sEPSCs remained constant (left), while that of sIPSCs was significantly decreased (right) in the AD group.

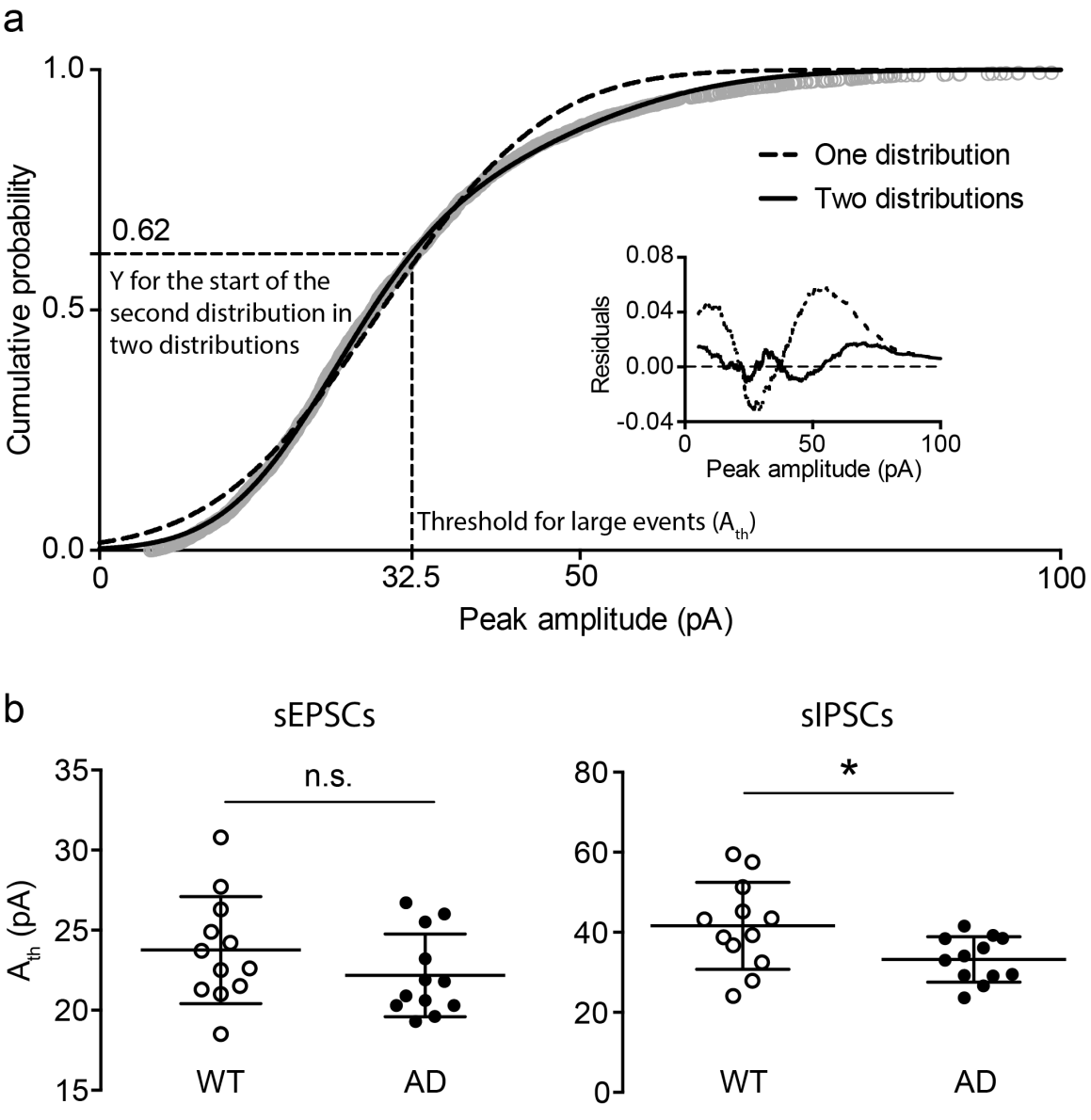

Figure 2. The sEPSCs and sIPSCs from each cell can be divided into two groups according to the bimodal distribution of their amplitudes. (**a**) Example of choosing an objective amplitude threshold (A_{th}) to divide the sIPSCs into small and large groups. The cumulative distribution of all sIPSC amplitudes was fitted with either one (dashed line) or two (solid line) cumulative normal distributions. When fitting with two distributions, the amplitude threshold (A_{th}) is the corresponding X value on the fitted curve at the start of the second distribution. Inset, the difference between the predicted and the actual amplitude values (residuals) when fitting with one (dashed line) or two (solid line) cumulative normal distributions. (**b**) The A_{th} of sEPSCs and sIPSCs in WT and AD cells. The A_{th} of sEPSCs remained constant (left), while that of sIPSCs was reduced (right) in AD cells.

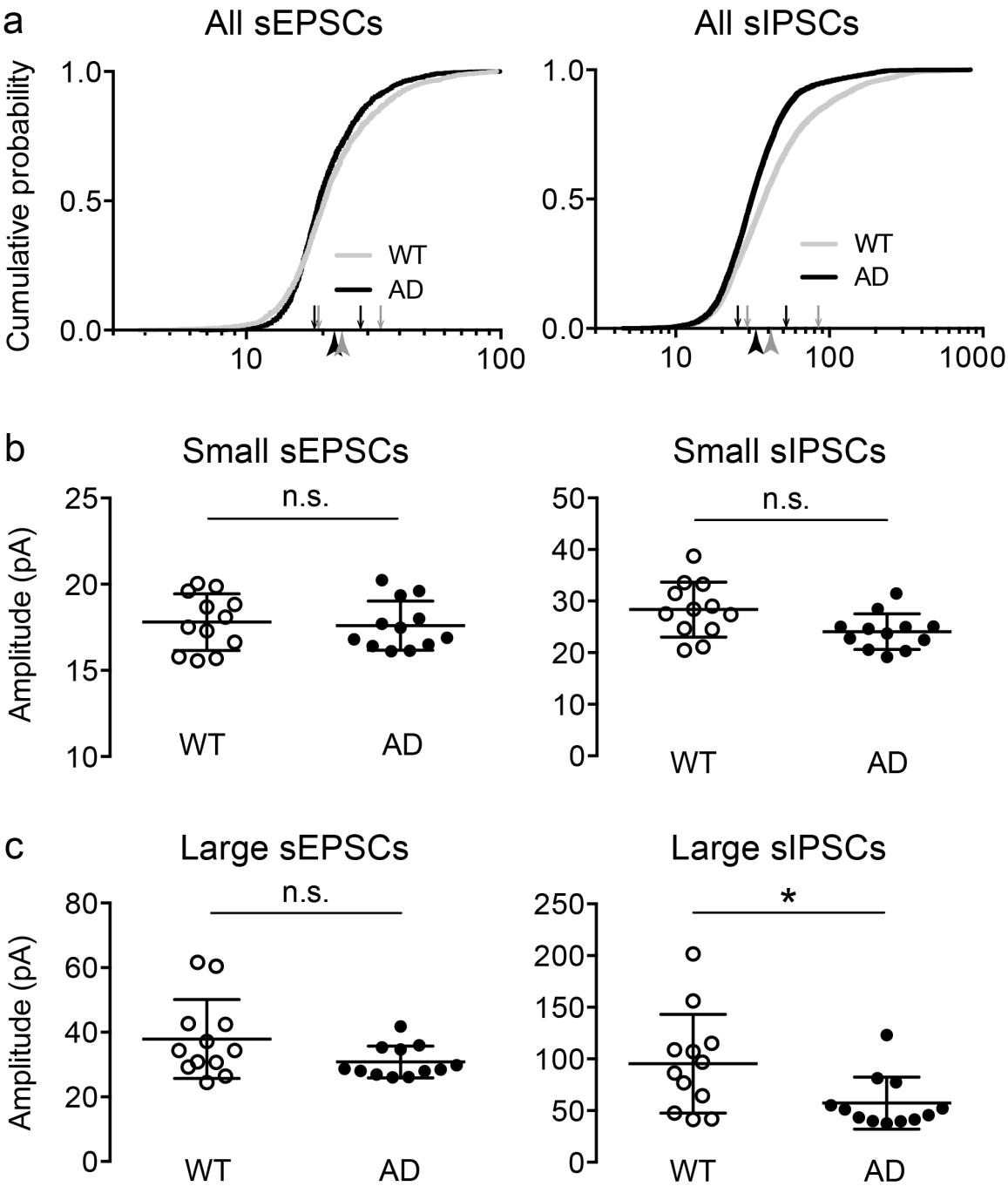

Figure 3. The average amplitude of large sIPSCs was significantly reduced in AD pyramidal cells. (**a**) The cumulative distributions of sEPSC (left) and sIPSC (right) amplitudes of all cells recorded in WT (grey curve) and AD (black curve) mice. The arrows are showing the mean of the first and second distribution when fitting with two cumulative normal distributions for WT

(grey arrows) and AD (black arrows) cells. The arrowheads are showing the A_{th} values for WT (grey arrowheads) and AD (black arrowheads) cells. (**b**) The average amplitudes of small sEPSCs (left) and small sIPSCs (right) were both not significantly altered in the AD group. (**c**) The average amplitude of large sEPSCs was unchanged (left), while that of large sIPSCs was significantly reduced (right) in the AD group.

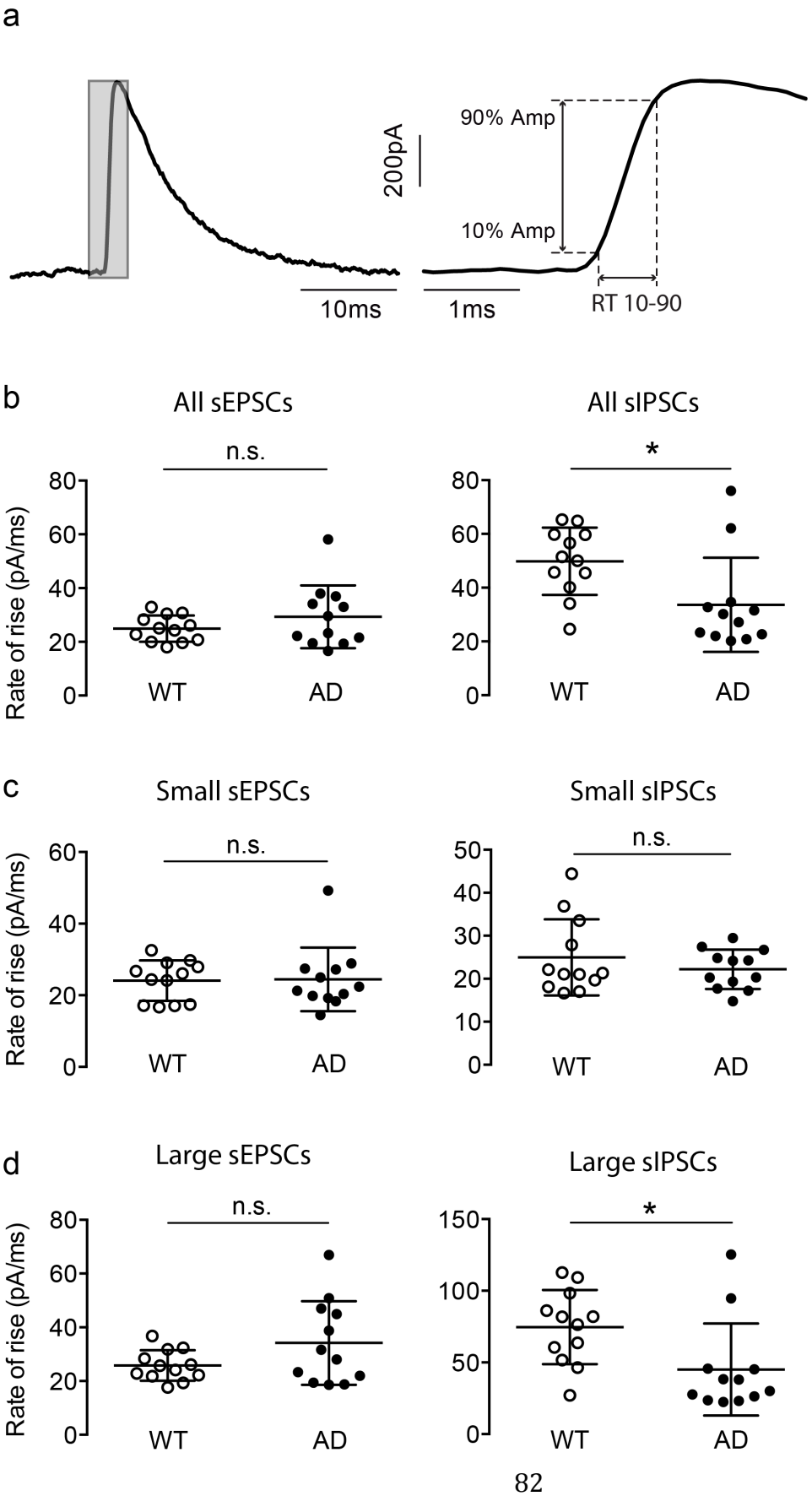
a
90% Amp
200pA
10% Amp
10ms
1ms
RT 10-90
b
All sEPSCs
All sIPSCs
n.s.
*
Rate of rise (pA/ms)
WT
AD
c
Small sEPSCs
Small sIPSCs
n.s.
n.s.
d
Large sEPSCs
Large sIPSCs
n.s.
*

Figure 4. The analysis of rate of rise revealed a significant decrease only in the large sIPSCs of AD pyramidal cells. (**a**) The rate of rise was calculated as the ratio between the increase in current and the rise time (RT) from 10% (10% Amp) to 90% (90% Amp) of the peak. (**b**) The average rate of rise of all sEPSCs was unchanged (left), while that of all sIPSCs was reduced (right) in the AD group. (**c**) The average rate of rise of either small sEPSCs (left) or small sIPSCs (right) was not altered in the AD group. (**d**) The average rate of rise of large sEPSCs remained constant (left), while that of large sIPSCs was significantly reduced (right) in the AD group.

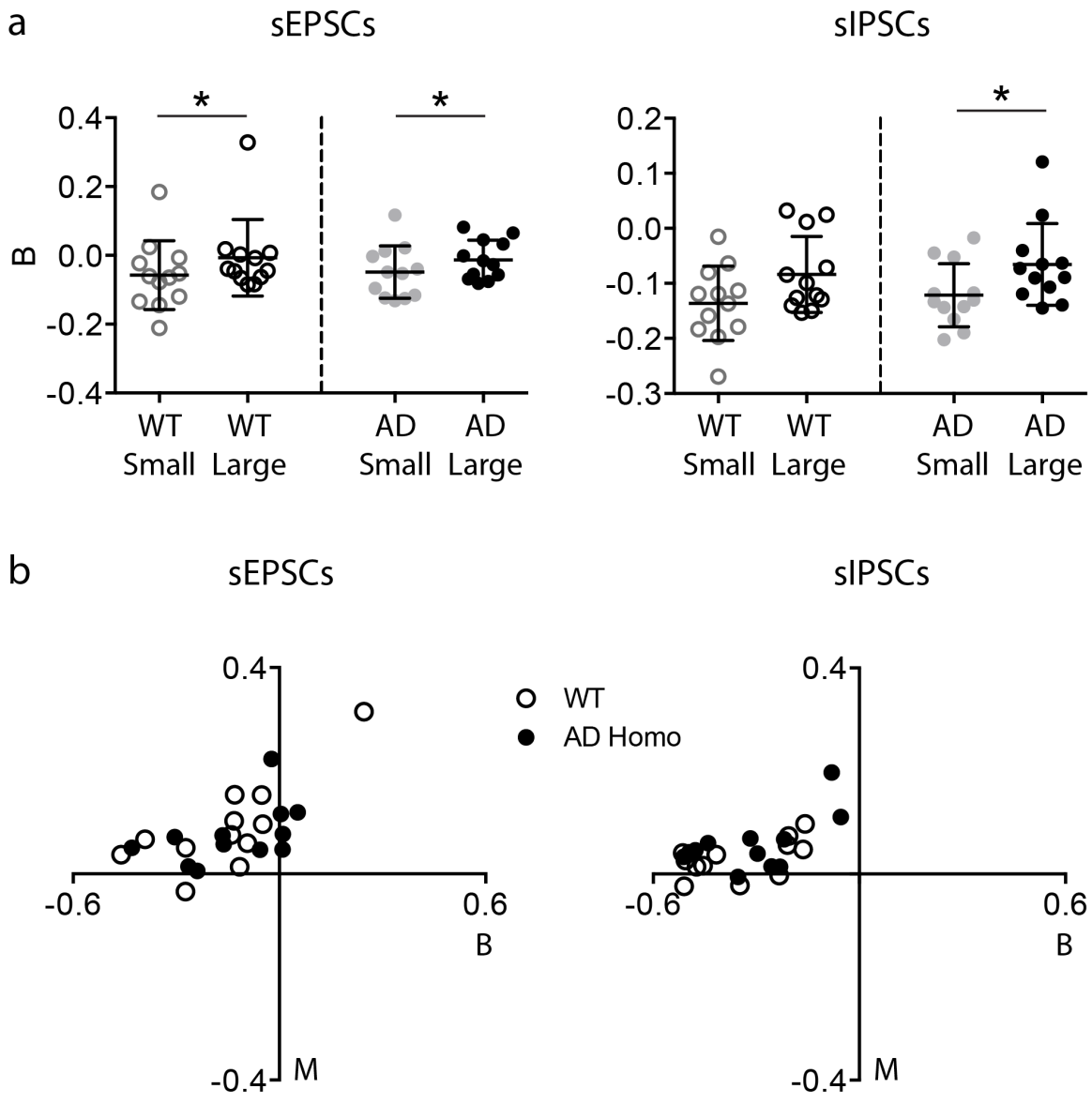

Figure 5. The analysis of burstiness (*B*) and memory (*M*) showed different firing patterns of small and large events. (**a**) Left, the burstiness of large sEPSCs was significantly closer to 0 (indicating a Poisson process) than that of small sEPSCs for both WT and AD pyramidal cells. Right, the burstiness of large sIPSCs was significantly closer to 0 than that of small sIPSCs for AD cells, but not for WT cells. (**b**) The distribution of *B* and *M* values calculated with all sEPSCs (left) and sIPSCs (right) from each cell in a *B*-*M* plane showed negative B values, indicating

regular firing pattern, and close-to-zero M values, indicating little memory in both WT and AD pyramidal cells.

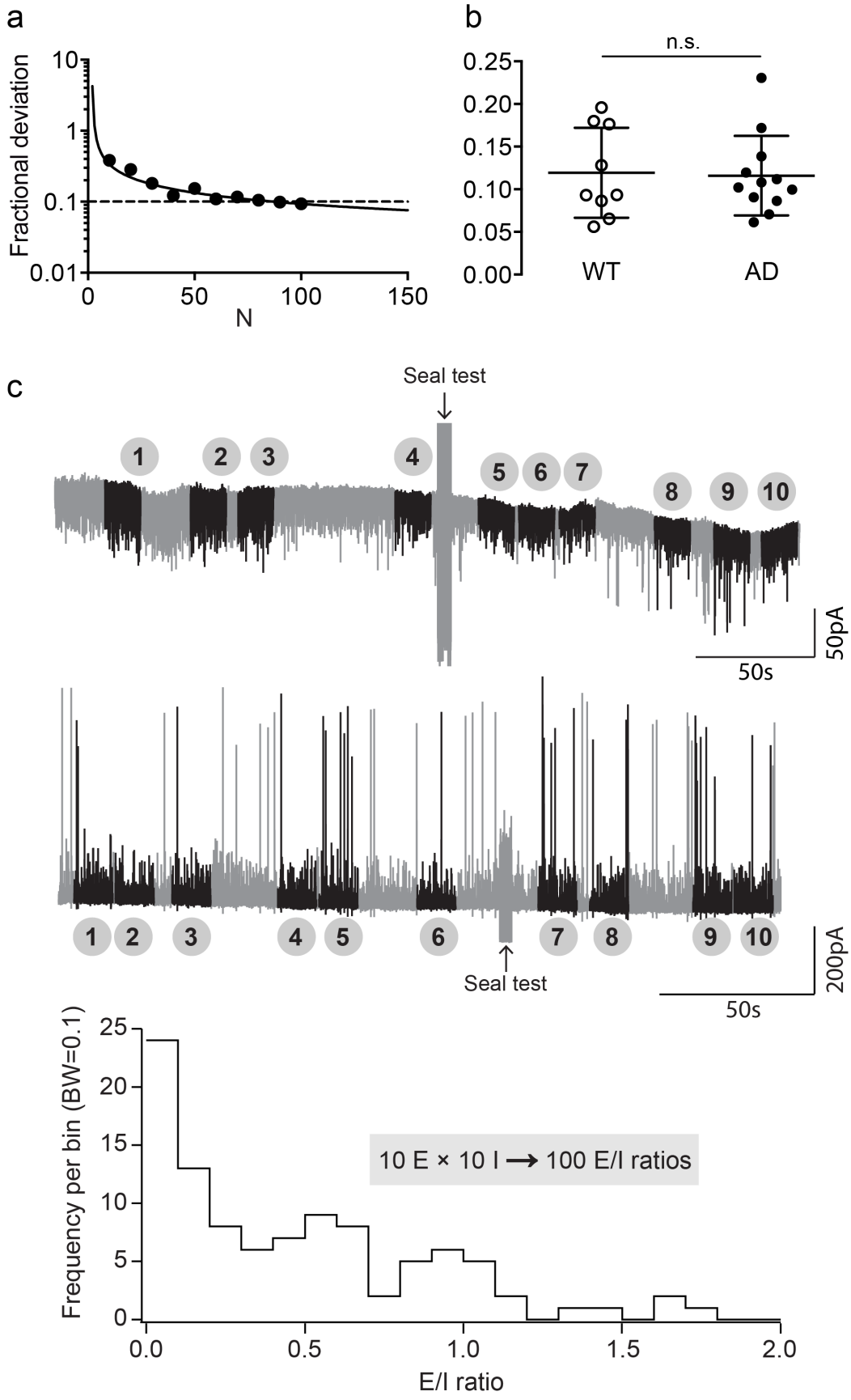
a
Fractional deviation
10
1
0.1
0.01
0
50
100
150
N
b
n.s.
0.25
0.20
0.15
0.10
0.05
0.00
WT
AD
c
Seal test
1
2
3
4
5
6
7
8
9
10
50pA
50s
1
2
3
4
5
6
7
8
9
10
Seal test
200pA
50s
Frequency per bin (BW=0.1)
25
20
15
10
5
0
0.0
0.5
1.0
1.5
2.0
E/I ratio
10 E × 10 I → 100 E/I ratios

Figure 6. A new approach to determine the E/I ratio can predict the real E/I value of each cell with high accuracy. (**a**) The fractional deviation of the sample mean from the real population mean decreases with the increase of sample size (N). The curve shows deviations calculated with the mean (μ) and standard deviation (σ) of 100 samples (N=100), and the 10 dots are deviation values calculated with the μ and σ of N=10, 20, …, 100 samples, from left to right. (**b**) When acquiring 100 E/I ratios, for both WT and AD cells, the fractional deviation reaches a low value (~12%), and it is not significantly different in the two groups. (**c**) Randomly selecting 10 segments of 15 sec from the raw recording traces of sEPSCs (top) and sIPSCs (middle) can yield 100 E/I ratios when crossing over the 10 phasic E and 10 phasic I charges (bottom).

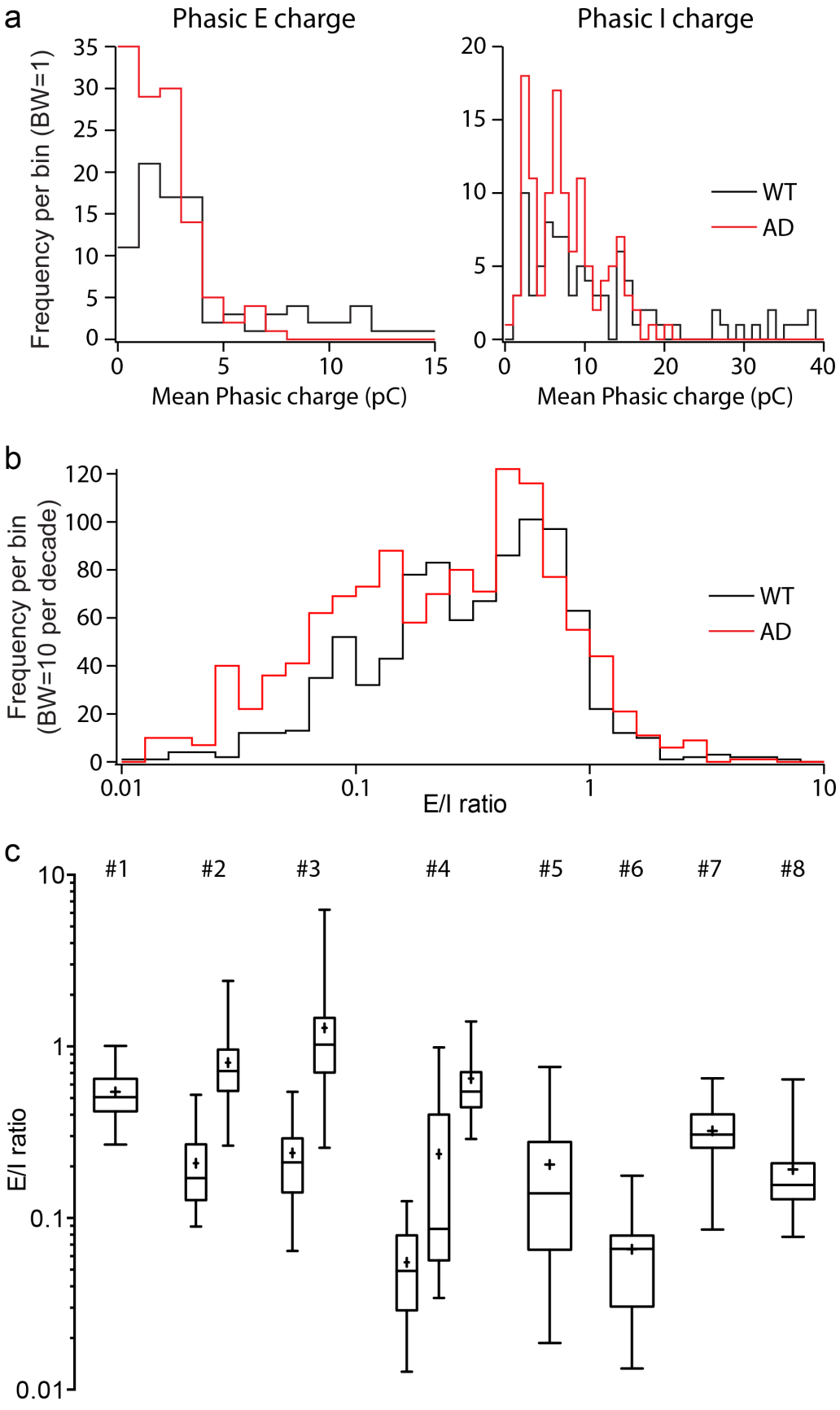
a
Phasic E charge
Phasic I charge
Frequency per bin (BW=1)
Mean Phasic charge (pC)
Mean Phasic charge (pC)
WT
AD
b
Frequency per bin (BW=10 per decade)
E/I ratio
WT
AD
c
#1
#2
#3
#4
#5
#6
#7
#8
E/I ratio

Figure 7. The E/I ratios calculated with the new approach showed a tendency of reduction in the AD group. (**a**) Histogram of phasic E (left) and phasic I (right) charges showed a reduction in both E and I in AD pyramidal cells (10 E and 10 I values for each cell). (**b**) Histogram of E/I ratio showed a shift to the left in the AD group, however the E/I was not significantly altered according to a nested two-way ANOVA test. (**c**) The E/I values for the AD group showed large variations among the 100 values in each cell (shown as each bar), among different cells in each animal (shown as each #), and among different animals.

References

Anderson LL, Hawkins NA, Thompson CH, Kearney JA, George AL (2017) Unexpected Efficacy of a Novel Sodium Channel Modulator in Dravet Syndrome. Sci Rep 7:1–9.

Bakker A, Krauss GL, Albert MS, Speck CL, Jones LR, Stark CE, Yassa MA, Bassett SS, Shelton AL, Gallagher M (2012) Reduction of Hippocampal Hyperactivity Improves Cognition in Amnestic Mild Cognitive Impairment. Neuron 74:467–474.

Bartley AF, Dobrunz LE (2015) Short-term plasticity regulates the excitation/inhibition ratio and the temporal window for spike integration in CA1 pyramidal cells. Eur J Neurosci 41:1402–1415.

Busche MA, Eichhoff G, Adelsberger H, Abramowski D, Wiederhold K-H, Haass C, Staufenbiel M, Konnerth A, Garaschuk O (2008) Clusters of Hyperactive Neurons Near Amyloid Plaques in a Mouse Model of Alzheimer's Disease. Science (80-) 321:1686–1689.

Busche MA, Konnerth A (2016) Impairments of neural circuit function in Alzheimer's disease. Philos Trans R Soc London - Ser B Biol Sci 371:1–10.

Buzsáki G, Wang X-J (2012) Mechanisms of gamma oscillations. Annu Rev Neurosci 35:203–225.

Cardin JA, Carlén M, Meletis K, Knoblich U, Zhang F, Deisseroth K, Tsai L-H, Moore CI (2009) Driving fast-spiking cells induces gamma rhythm and controls sensory responses. Nature 459:663–667.

Cheng IH, Scearce-Levie K, Legleiter J, Palop JJ, Gerstein H, Bien-Ly N, Puoliväli J, Lesné S, Ashe KH, Muchowski PJ, Mucke L (2007) Accelerating amyloid-beta fibrillization reduces oligomer levels and functional deficits in Alzheimer disease mouse models. J Biol Chem 282:23818–23828.

Cho KKA, Hoch R, Lee AT, Patel T, Rubenstein JLR, Sohal VS (2015) Gamma rhythms link prefrontal interneuron dysfunction with cognitive inflexibility in Dlx5/6(+/-) mice. Neuron

85:1332–1343.

Cissé M, Halabisky B, Harris J, Devidze N, Dubal DB, Sun B, Orr A, Lotz G, Kim DH, Hamto P, Ho K, Yu G-Q, Mucke L (2011) Reversing EphB2 depletion rescues cognitive functions in Alzheimer model. Nature 469:47–52.

Cruikshank SJ, Lewis TJ, Connors BW (2007) Synaptic basis for intense thalamocortical activation of feedforward inhibitory cells in neocortex. Nat Neurosci 10:462.

Eckblad JW (1991) How Many Samples Should Be Taken? Bioscience 41:346–348.

Fernandez F, Morishita W, Zuniga E, Nguyen J, Blank M, Malenka RC, Garner CC (2007) Pharmacotherapy for cognitive impairment in a mouse model of Down syndrome. Nat Neurosci 10:411.

Ferri CP, Prince M, Brayne C, Brodaty H, Fratiglioni L, Ganguli M, Hall K, Hasegawa K, Hendrie H, Huang Y, Jorm A, Mathers C, Menezes PR, Rimmer E, Scazufca M (2005) Global prevalence of dementia: a Delphi consensus study. Lancet 366:2112–2117.

Frederiksen K, Lu D, Yang J, Jensen HS, Bastlund JF, Larsen PH, Liu H, Crestey F, Dekermendjian K, Badolo L, Laursen M, Hougaard C, Yang C, Svenstrup N, Grunnet M (2017) A small molecule activator of Nav1.1 channels increases fast-spiking interneuron excitability and GABAergic transmission in vitro and has anti-convulsive effects in vivo. Eur J Neurosci 46:1887–1896.

Freund TF, Katona I (2007) Perisomatic inhibition. Neuron 56:33–42.

Games D, Adams D, Alessandrini R, Barbour R, Berthelette P, Blackwell C, Carr T, Clemens J, Donaldson T, Gillespie F (1995) Alzheimer-type neuropathology in transgenic mice overexpressing V717F beta-amyloid precursor protein. Nature 373:523–527.

Glykys J, Mody I (2007) The main source of ambient GABA responsible for tonic inhibition in the mouse hippocampus. J Physiol 582:1163–1178.

Gogolla N, LeBlanc JJ, Quast KB, Südhof TC, Fagiolini M, Hensch TK (2009) Common circuit defect of excitatory-inhibitory balance in mouse models of autism. J Neurodev Disord

1:172–181.

Goh K-I, Barabási A-L (2008) Burstiness and memory in complex systems. EPL (Europhysics Lett 81:48002.

Götz J, Ittner LM (2008) Animal models of Alzheimer's disease and frontotemporal dementia. Nat Rev Neurosci 9:532–544.

Götz J, Streffer JR, David D, Schild A, Hoerndli F, Pennanen L, Kurosinski P, Chen F (2004) Transgenic animal models of Alzheimer's disease and related disorders: histopathology, behavior and therapy. Mol Psychiatry 9:664–683.

Harris JA, Devidze N, Verret L, Ho K, Halabisky B, Thwin MT, Kim D, Hamto P, Lo I, Yu G-Q, Palop JJ, Masliah E, Mucke L (2010) Transsynaptic progression of amyloid-β-induced neuronal dysfunction within the entorhinal-hippocampal network. Neuron 68:428–441.

Hazra A, Gu F, Aulakh A, Berridge C, Eriksen JL, Žiburkus J (2013) Inhibitory Neuron and Hippocampal Circuit Dysfunction in an Aged Mouse Model of Alzheimer's Disease Dickey CA, ed. PLoS One 8:e64318.

Hsiao K, Chapman P, Nilsen S, Eckman C, Harigaya Y, Younkin S, Yang F, Cole G (1996) Correlative Memory Deficits, Abeta Elevation, and Amyloid Plaques in Transgenic Mice. Science (80-) 274:99–103.

Hsieh H, Boehm J, Sato C, Iwatsubo T, Tomita T, Sisodia S, Malinow R (2006) AMPAR Removal Underlies Aβ-Induced Synaptic Depression and Dendritic Spine Loss. Neuron 52:831–843.

Isaacson JS, Scanziani M (2011) How inhibition shapes cortical activity. Neuron 72:231–243.

Jacobs HIL, Van Boxtel MPJ, Jolles J, Verhey FRJ, Uylings HBM (2012) Parietal cortex matters in Alzheimer's disease: An overview of structural, functional and metabolic findings. Neurosci Biobehav Rev 36:297–309.

Jacobs HIL, Van Boxtel MPJ, Uylings HBM, Gronenschild EHBM, Verhey FR, Jolles J (2011) Atrophy of the parietal lobe in preclinical dementia. Brain Cogn 75:154–163.

Kamenetz F, Tomita T, Hsieh H, Seabrook G, Borchelt D, Iwatsubo T, Sisodia S, Malinow R (2003) APP Processing and Synaptic Function. Neuron 37:925–937.

Kehrer C, Maziashvili N, Dugladze T, Gloveli T (2008) Altered excitatory-inhibitory balance in the NMDA-hypofunction model of schizophrenia. Front Mol Neurosci 1:6.

Klausberger T, Roberts JDB, Somogyi P (2002) Cell type- and input-specific differences in the number and subtypes of synaptic GABA(A) receptors in the hippocampus. J Neurosci 22:2513–2521.

LaFerla FM, Green KN (2012) Animal models of Alzheimer disease. Cold Spring Harb Perspect Med 2:a006320-.

Lam AD, Deck G, Goldman A, Eskandar EN, Noebels J, Cole AJ (2017) Silent hippocampal seizures and spikes identified by foramen ovale electrodes in Alzheimer's disease. Nat Med 23:678–680.

Mayeux R, Stern Y (2012) Epidemiology of Alzheimer disease. Cold Spring Harb Perspect Med 2:a006239-.

Nakazono T, Lam TN, Patel AY, Kitazawa M, Saito T, Saido TC, Igarashi KM (2017) Impaired In Vivo Gamma Oscillations in the Medial Entorhinal Cortex of Knock-in Alzheimer Model. Front Syst Neurosci 11:1–13.

Nilsson P, Saito T, Saido TC (2014) New mouse model of Alzheimer's. ACS Chem Neurosci 5:499–502.

Noebels J (2011) A perfect storm: Converging paths of epilepsy and Alzheimer's dementia intersect in the hippocampal formation. Epilepsia 52 Suppl 1:39–46.

Nyíri G, Freund TF, Somogyi P (2001) Input-dependent synaptic targeting of alpha(2)-subunit-containing GABA(A) receptors in synapses of hippocampal pyramidal cells of the rat. Eur J Neurosci 13:428–442.

Palop JJ, Chin J, Bien-Ly N, Massaro C, Yeung BZ, Yu G-Q, Mucke L (2005) Vulnerability of dentate granule cells to disruption of arc expression in human amyloid precursor protein

transgenic mice. J Neurosci 25:9686–9693.

Palop JJ, Chin J, Roberson ED, Wang J, Thwin MT, Bien-Ly N, Yoo J, Ho KO, Yu G-Q, Kreitzer A, Finkbeiner S, Noebels JL, Mucke L (2007) Aberrant excitatory neuronal activity and compensatory remodeling of inhibitory hippocampal circuits in mouse models of Alzheimer's disease. Neuron 55:697–711.

Palop JJ, Jones B, Kekonius L, Chin J, Yu G-Q, Raber J, Masliah E, Mucke L (2003) Neuronal depletion of calcium-dependent proteins in the dentate gyrus is tightly linked to Alzheimer's disease-related cognitive deficits. Proc Natl Acad Sci U S A 100:9572–9577.

Palop JJ, Mucke L (2009) Epilepsy and cognitive impairments in Alzheimer disease. Arch Neurol 66:435–440.

Palop JJ, Mucke L, Roberson ED (2011) Quantifying biomarkers of cognitive dysfunction and neuronal network hyperexcitability in mouse models of Alzheimer's disease: depletion of calcium-dependent proteins and inhibitory hippocampal remodeling. Methods Mol Biol 670:245–262.

Perez C, Ziburkus J, Ullah G (2016) Analyzing and Modeling the Dysfunction of Inhibitory Neurons in Alzheimer's Disease Cymbalyuk G, ed. PLoS One 11:e0168800.

Rissman RA, Mobley WC (2011) Implications for treatment: GABAA receptors in aging, Down syndrome and Alzheimer's disease. J Neurochem 117:no-no.

Roberson ED, Halabisky B, Yoo JW, Yao J, Chin J, Yan F, Wu T, Hamto P, Devidze N, Yu G-Q, Palop JJ, Noebels JL, Mucke L (2011) Amyloid-β/Fyn-induced synaptic, network, and cognitive impairments depend on tau levels in multiple mouse models of Alzheimer's disease. J Neurosci 31:700–711.

Saito T, Matsuba Y, Mihira N, Takano J, Nilsson P, Itohara S, Iwata N, Saido TC (2014) Single App knock-in mouse models of Alzheimer's disease. Nat Neurosci 17:661–663.

Saito T, Matsuba Y, Yamazaki N, Hashimoto S, Saido TC (2016) Calpain Activation in Alzheimer's Model Mice Is an Artifact of APP and Presenilin Overexpression. J Neurosci

36:9933–9936.

Sasaguri H, Nilsson P, Hashimoto S, Nagata K, Saito T, De Strooper B, Hardy J, Vassar R, Winblad B, Saido TC (2017) APP mouse models for Alzheimer's disease preclinical studies. EMBO J 36:e201797397.

Scarmeas N, Honig LS, Choi H, Cantero J, Brandt J, Blacker D, Albert M, Amatniek JC, Marder K, Bell K, Hauser WA, Stern Y (2009) Seizures in Alzheimer disease: who, when, and how common? Arch Neurol 66:992–997.

Scharfman HE (2012) "Untangling" Alzheimer's disease and epilepsy. Epilepsy Curr 12:178–183.

Schleiss M, Smith JA, Schleiss M, Smith JA (2016) Two Simple Metrics for Quantifying Rainfall Intermittency: The Burstiness and Memory of Interamount Times. J Hydrometeorol 17:421–436.

Schmitt HP (2005) On the paradox of ion channel blockade and its benefits in the treatment of Alzheimer disease. Med Hypotheses 65:259–265.

Serrano-Pozo A, Frosch MP, Masliah E, Hyman BT (2011) Neuropathological alterations in Alzheimer disease. Cold Spring Harb Perspect Med 1:a006189.

Sohal VS (2012) Insights into cortical oscillations arising from optogenetic studies. Biol Psychiatry 71:1039–1045.

Sohal VS, Zhang F, Yizhar O, Deisseroth K (2009) Parvalbumin neurons and gamma rhythms enhance cortical circuit performance. Nature 459:698–702.

Sturchler-Pierrat C, Abramowski D, Duke M, Wiederhold K-H, Mistl C, Rothacher S, Ledermann B, Burki K, Frey P, Paganetti PA, Waridel C, Calhoun ME, Jucker M, Probst A, Staufenbiel M, Sommer B (1997) Two amyloid precursor protein transgenic mouse models with Alzheimer disease-like pathology. Proc Natl Acad Sci 94:13287–13292.

Thomson AM, Bannister AP, Hughes DI, Pawelzik H (2000) Differential sensitivity to Zolpidem of IPSPs activated by morphologically identified CA1 interneurons in slices of rat

hippocampus. Eur J Neurosci 12:425–436.

Verret L, Mann EO, Hang GB, Barth AMI, Cobos I, Ho K, Devidze N, Masliah E, Kreitzer AC, Mody I, Mucke L, Palop JJ (2012) Inhibitory interneuron deficit links altered network activity and cognitive dysfunction in Alzheimer model. Cell 149:708–721.

Walsh DM, Klyubin I, Fadeeva J V., Cullen WK, Anwyl R, Wolfe MS, Rowan MJ, Selkoe DJ (2002) Naturally secreted oligomers of amyloid β protein potently inhibit hippocampal long-term potentiation in vivo. Nature 416:535–539.

Wehr M, Zador AM (2003) Balanced inhibition underlies tuning and sharpens spike timing in auditory cortex. Nature 426:442–446.

Williams SR, Buhl EH, Mody I (1998) The dynamics of synchronized neurotransmitter release determined from compound spontaneous IPSCs in rat dentate granule neurones *in vitro*. J Physiol 510:477–497.

Yan X-X, Cai Y, Shelton J, Deng S-H, Luo X-G, Oddo S, Laferla FM, Cai H, Rose GM, Patrylo PR (2012) Chronic temporal lobe epilepsy is associated with enhanced Alzheimer-like neuropathology in 3×Tg-AD mice. PLoS One 7:e48782.

Chapter IV

Novel Analysis Based on *in vivo* Local Field Potential Recordings Revealed Sleep Disturbances in Aged App^{NL-F} Mice

4.1 Summary

A large fraction of Alzheimer's disease (AD) patients show aberrant brain activities that mostly resembles complex partial seizures, and an estimated 10 to 20% develop overt seizures. Especially, these abnormal network activities usually start in early stages of the disease and may contribute to the emergence of AD symptoms such as cognitive decline. Since clinical seizures are not reported in most AD cases, it remains difficult to monitor the occurrence of epileptiform activities that take place in deep temporal structures. With the advantage of various mouse models of AD, we can now examine the altered network activities associated with other hallmarks of the disease, such as amyloid β plaque deposition. Using the App^{NL-F} mouse model, which has fewer artificial phenotypes compared to other existing models, we have examined the network activities through *in vivo* LFP recordings in hippocampal CA1 pyramidal cell layer. Together with monitoring the physical activities, we have applied a novel method to determine different sleep/awake states of mice objectively. Our results showed that the sleep cycles were disrupted in 11 m old NL-F homozygous mice, but not at a younger age. At the same age, we have also observed spikes emerging during prolonged sharp wave ripples (SWRs), indicating possible transition of SWRs into epileptiform discharges. Taken together, our studies could have

caught a critical period in the disease progression when plaque accumulation, sleep disturbances and changes in network activities take place and lead to further cognitive decline.

4.2 Introduction

4.2.1 Epilepsy and AD

In AD patients, aberrant network activities that mostly resemble those found in complex partial seizures were observed in early stages of the disease and may contribute to the emergence of AD symptoms such as cognitive decline(Palop and Mucke, 2009; Noebels, 2011; Bakker et al., 2012; Scharfman, 2012; Chin and Scharfman, 2013; Born, 2015; Vossel et al., 2017). Epilepsy with clinical seizures are particularly more prevalent in familial and sporadic AD patients at younger ages, while overt seizures are not reported in most AD cases(Rao et al., 2009; Scarmeas et al., 2009; Vossel et al., 2013; Born, 2015; Sarkis et al., 2016). The non-motor seizures are easily missed because the symptoms can overlap with cognitive features of AD, such as amnestic spells, speech arrest, amnestic wandering, or sensory phenomena, many of which are typical phenotypes of focal hippocampal, so called complex partial, seizures(Vossel et al., 2017). To distinguish the epileptic events from AD symptoms, one needs the support of epileptiform activity on EEG (electroencephalograph). However, it remains difficult to study potential epileptiform activities in patients with conventional EEG electrodes because the aberrant activities take place in deep temporal structures. With extended monitoring using scalp EEG and/or EMG (magnetoencephalography), Vossel *et al*. revealed that the incidence of subclinical epileptiform activity in AD patients was significantly higher than age-matched controls, and individuals with epileptiform discharges showed faster global cognitive decline(Vossel et al., 2016). Horváth *et al*. have described more sensitive sleep EEG detection settings to monitor epileptiform discharges in AD patients, which revealed that 82% of epileptiform discharges occurred during sleep, mainly related to non-REM sleep(Horváth et al., 2017). Also, another recent study using foramen ovale electrodes positioned adjacent to the mesial temporal lobe (mTL) revealed clinically silent hippocampal seizures and epileptiform

spikes during sleep, a period especially important for memory consolidation, which may further increase their impact on the disease progression(Lam et al., 2017).

4.2.2 Epileptiform network activities in mouse models of AD

With the advantage of transgenic mouse models of AD (see **Chapter II** for details), it is possible for us to study the link between seizures and AD. The 1st generation of mouse models use the approach of overexpressing mutant or wild-type human amyloid precursor protein (hAPP) with powerful exogenous promoters, sometimes together with the overexpression of other AD-related proteins(Sasaguri et al., 2017). Many hAPP-overexpressing mouse models of AD display hypersynchronous network activities and epileptiform discharges, and spontaneous seizures(Born, 2015). For example, non-convulsive seizures were observed in hAPPJ20 mice(Palop et al., 2007; Verret et al., 2012), while infrequent tonic-clonic seizures were observed in Tg2576 mice(Westmark et al., 2008) and APP23 mice(Lalonde et al., 2005) (both models overexpressing hAPP carrying the Swedish mutations under different promoters), which may contribute to the increased sudden death often observed in these models.

An impairment of *in vivo* gamma oscillations in hippocampus and parietal cortex was revealed in a number of studies using different mouse models of AD(Verret et al., 2012; Gillespie et al., 2016; Iaccarino et al., 2016). Specifically, in hAPPJ20 mice, EEG recordings revealed that spontaneous epileptiform discharge occur primarily during reduced gamma oscillation activity, and an inverse correlation was found between the intensity of gamma oscillation and the spike rate(Verret et al., 2012). Furthermore, exploratory behavior was associated with increased gamma activity and fewer spikes in these mice(Verret et al., 2012). Various studies have demonstrated that gamma oscillation depends on the synaptic activity of parvalbumin-positive GABAergic interneurons (PV INs) and enhances cognitive functions(Mann and Paulsen, 2007;

Cardin et al., 2009; Sohal et al., 2009; Korotkova et al., 2010). PV IN dysfunction caused by reduced levels of voltage-gated sodium channel subunit Nav1.1 contributes to abnormalities in oscillatory rhythms, network synchrony, and cognition in hAPPJ20 mice and possibly in AD patients(Verret et al., 2012).

It is essential to examine the epileptiform activities in the new generation of mouse models that use a gene knock-in approach (APP-KI models), because the artificially high levels of Aβ, APP, and its various cleavage products in the hAPP-overexpressing models make it difficult to untangle the individual contribution of Aβ to seizure activities. It has been found that in the APP/TTA model, which overexpress hAPP with Swedish and London mutations, overall tgAPP suppression but not a specific Aβ reduction with γ-secretase inhibitor could reduce epileptiform discharge and normalize other electrical abnormalities found in these animals(Born et al., 2014). These results indicate that elevated levels of APP, not Aβ, play an important role in the development and maintenance of epileptiform activities. Also, since Aβ reduction alone did not reduce epileptiform activities, it is possible that the overproduction of one or more of other APP cleavage products contributed to the abnormalities. Moreover, with the critical role of APP in cortical development, overproduction of APP throughout the development of transgenic mice could have disrupted synapse and circuit development(Priller et al., 2006; Young-Pearse et al., 2007; Zheng and Koo, 2011; Hoe et al., 2012). For example, tgAPP suppression during post-natal development (P1-P42) delayed the onset of epileptiform activities in the APP/TTA mice, suggesting that overloading the brain with APP during the developmental period accelerates the progression of epileptiform activities(Born et al., 2014).

To date, there are only very few studies on network abnormalities in the APP-KI mouse models. In 5 m-old App^{NL-F} mice, under urethane-anesthesia, abnormal gamma oscillations were observed in the entorhinal cortex, including reduced theta-gamma coupling and impaired phase-

locking of layer 2/3 pyramidal cell spiking activities (Nakazono et al., 2017). A 2016 paper showed that there was no change in the overall Nav1.1 level in either APP-overexpressing (APP23) or *App*$^{NL-F}$ mice brain homogenates, suggesting that Nav1.1 downregulation may be a phenotype unique to the hAPPJ20 mice(Saito et al., 2016). Yet the fraction of PV INs in brain homogenates may be too small to detect changes in this specific population of interneurons. Therefore, a PV IN specific reduction of Nav1.1 may still be present in *App*$^{NL-F}$ mice. Our patch-clamp recordings from cortical pyramidal cells and subsequent rigorous analyses on the spontaneous inhibitory postsynaptic currents (sIPSCs) are consistent with this possibility (See **Chapter III**), and it is necessary to further examine if there are alterations at the network level, such as epileptiform discharges in the *App*$^{NL-F}$ mice.

4.2.3 Sharp wave ripples and epileptiform discharge in AD

Sharp wave ripples (SWRs) are highly synchronous population activities found in the mammalian brain. They are associated with NREM sleep and consummatory behaviors such as immobility, drinking, eating and grooming(Buzsáki et al., 1983; Buzsáki, 1984; Suzuki and Smith, 1987). SWRs consist of two components: sharp waves (SPWs), which are large amplitude deflections (40-100 ms) in CA1 stratum radiatum, and often associated “ripples”, which are short-lived fast oscillations (110-200 Hz) observed in the local field potential (LFP) in CA1 stratum pyramidale(O’Keefe, 1976; Buzsáki et al., 1983, 1992; Buzsáki, 1986; Suzuki and Smith, 1987, 1988a, 1988b). SWRs usually consist of 3-9 ripple waves, which can be characterized by the duration (ms) and amplitude (μV)(Buzsáki, 2015). So far, SWRs have been observed in the hippocampus of every mammalian species investigated, including humans(Bragin et al., 1999a; Le Van Quyen et al., 2010). Research has established the important role of SWRs in transferring compressed hippocampal presentation to other brain

regions and supporting memory consolidation, while selective disruption of SWRs interferes with memory(Buzsáki, 2015).

SWRs are the most synchronous events in the mammalian brain with a high excitatory gain. Therefore, even minor perturbations in the hippocampal circuits can turn SWRs into pathological events. Increased synchrony can cause SPWs to manifest as spikes, while ripples can turn into pathological high frequency oscillations (PHFOs, 200-500 Hz, 10-100 ms in duration)(Bragin et al., 1999b; Staba and Bragin, 2011; Staba et al., 2012). Interictal epileptiform discharges (IEDs) are often coupled with PHFOs, but both of them can occur independently(Alvarado-Rojas et al., 2015). In temporal lobe epilepsy (TLE) patients and animal models of TLE, IEDs may contribute to the cognitive impairments other than being a byproduct of the disease(Holmes and Lenck-Santini, 2006; Shatskikh et al., 2006; Kleen et al., 2010). Since epileptic activities are one of the early symptoms in AD patients, altered SWRs may contribute to memory decline in the disease, and treatment of IEDs and PHFOs may prevent cognitive decline in AD patients with epilepsy.

4.2.4 Disturbed sleeping patterns in AD

Besides progressive decline in cognitive functions such as loss of memory and language difficulties, sleep disturbance is a common behavioral symptom in AD as well, which is highly disruptive with a significant impact on patients and caregivers(Prinz et al., 1982b; Bliwise, 2004; Lim et al., 2014; Musiek et al., 2015; Peter-Derex et al., 2015). Changes in sleep are common in the normal aging process, with characteristics such as increasing sleep fragmentation, greater tendency for nighttime awakenings and daytime sleep, while dementia leads to further deterioration of sleep patterns(Bliwise, 1993). Alterations in the sleep-wake cycle may be one of the earliest symptoms in preclinical AD(Lim et al., 2014), and AD patients with sleep disturbances seem to have a more severe cognitive decline(Vitiello and Prinz, 1989; McCurry et

al., 2000). Sleep cycle also in turn regulates the level of Aβ deposition, which is demonstrated in mouse models of AD. A study on the amount of soluble Aβ levels in the brain interstitial fluid across the sleep-wake cycle in young Tg2576 mice showed approximately 25% higher levels of extracellular Aβ during wakefulness compared to sleep; furthermore, chronic sleep restriction led to a two-fold increase in plaque burden in both Tg2576 and APP/PS1 models(Kang et al., 2009).

Different stages in a normal sleep cycle work together to stabilize and enhance certain types of memories. In general, declarative memories (such as episodic memories of personal experience) are enhanced by NREM (non-rapid eye movement) sleep while procedural memories (such as memories for skills and habits) are enhanced by REM (rapid eye movement) sleep(Maquet, 2001; Walker and Stickgold, 2006). Symptoms of sleep disturbances in AD patients in general are qualitatively similar to those seen in the normal aging population but much more severe, yet REM sleep shows specific alterations with a significantly lower proportion in the total sleep time in AD(Prinz et al., 1982a, 1982b; Vitiello et al., 1990; Moe et al., 1995; Bombois et al., 2010). REM sleep is physiologically different from other sleep phases, which is distinguished by rapid movement of eyes and accompanies numerous physiological changes. In the Tg2576 mouse model of AD, amyloid plaque deposition was observed in brain regions critical for the generation of REM sleep, and these mice had prominent sleep and circadian abnormalities(Wisor et al., 2005; Zhang et al., 2005). In the APP/PS1 model, the disruption of sleep cycle began at the time of plaque deposition, and worsened as the deposition expanded to other areas(Roh et al., 2012). Therefore, there may be a link between Aβ plaque deposition and sleep disturbances observed both in AD patients and mouse models, and we will study possible sleep alterations in the App^{NL-F} mice at different time points during a critical period for the initial accumulation of Aβ plaque deposits.

4.2.5 Determination of sleep stages in mice

In order to study the sleep patterns in mice, it is important to reliably determine the sleep/awake states through monitoring of the brain and physical activities of the animals. In the studies described in the previous section, researchers were using polysomnographic analysis with commercially available software, which assesses the state of the animals based on EEG recordings (over the frontal and the parietal bone) and EMG recordings (usually in the neck musculature) (Zhang et al., 2005; Kang et al., 2009; Roh et al., 2012). Numerous algorithms exist to separate sleep stages and awake periods in mice, yet they are using sophisticated methods and require more or less subjective judgment(Brankačk et al., 2010; Fisher et al., 2013; Kreuzer et al., 2015; Lampert et al., 2015; Funato et al., 2016; Yaghouby and Sunderam, 2016). Here in the App^{NL-F} mice, we are using a novel approach for the automatic determination of sleep/awake stages, which is relatively simple and requires no subjective thresholds (Molnár et al., 2017). Our algorithm combines the information from the *in vivo* LFP recordings and the physical activities of the animals, and enables us to reliably determine the NREM and REM sleep as well as the awake states in mice.

4.3 Materials and Methods

4.3.1 Animal use

All animal use was approved by the UCLA Chancellor's Committee on Animal Welfare. App^{NL-F} mice were originally obtained from the research group led by Dr. Takaomi C. Saido at the Laboratory for Proteolytic Neuroscience, RIKEN Brain Science Institute, Saitama, Japan(Nilsson et al., 2014; Saito et al., 2014). Wild-type control mice (WT) were aged C57Bl/6 mice from our own wild type colonies. Mice were housed under the care of the Division of Laboratory Animal Medicine (DLAM) of University of California, Los Angeles (UCLA). Mice were maintained in a 12

h light/dark cycle with ad libitum access to food and water. All experiments were done during the light cycle.

4.3.2 Surgery

Surgeries were performed under aseptic conditions on male *App*$^{NL-F}$ mice (homozygous and heterozygous) and aged matched WT controls as previously described(Barth et al., 2014). Briefly, mice were fixed with ear bars on a standard stereotaxic frame (Stoelting Co.) under anesthesia by isoflurane inhalation (2-2.5% isoflurane in 100% O_2 at 1.25-1.5 L/min) with a vaporizer (Patterson Scientific). Body temperature was maintained with a circulating heating pad, and artificial tears ointment (Rugby) was put on the eyes. 5 mg/kg lidocaine was injected under the skin close to where incisions would be made for local numbness; and 5 mg/kg carprofen was given under skin on the back to prevent inflammation. The scalp was treated with betadine and 70% ethanol for 3 times before making an incision. The cranium was exposed with through a small midline scalp incision. Three openings were made on the cranium with aseptic drill heads (Fine Science Tool No. 19007-07; 0.7 mm diameter): Two for the recording electrodes (PlasticsOne, 127 um diameter) were made with locations as follows: from Bregma, -1.9 mm caudal, ±1.5 mm lateral; the third for the reference electrode was made above the cerebellum. The two recording electrodes were guided down through the openings with a micromanipulator on the stereotaxic system. When reaching the top of the brain, they were moved down synchronously for another 1.3 mm to reach bilateral hippocampal CA1 stratum pyramidale. With the micromanipulator holding the electrodes, the skull surface was covered with a thin layer of cyanoacrylates-based glue (Super Glue, Loctite), and then dental cement (Ortho-Jet, Lang Dental Manufacturing Co Inc.) was used to attach the electrode sockets to the skull while covering the part of cranium without scalp. Lastly a custom-made plastic protection hat was placed around the electrode sockets and fixed with dental cement as well.

Right after surgery another 5 mg/kg lidocaine and 5 mg/kg carprofen was injected under the skin on the neck and back, respectively. The animal was returned to home cage with food and water on a heating pad. The mouse was continuously monitored until recover, and then returned to the animal room. For the next 2 consecutive days, 5 mg/kg carprofen was administered under the skin on the back.

4.3.3 In vivo local field potential and video recordings

Mice were allowed to recover from surgery for at least a week, and were transiently anesthetized with isoflurane right before connected to the recording system. Local field potential (LFP) recordings were performed in awake, freely moving animals for at least 3 full days (6 light-dark cycles minimum) in cylindrical containers (Carlisle No. 10768; 0.3 m diameter, 0.3 m tall). LFPs were recorded with a custom-made miniature dual headstage connected to the electrode sockets on the animal's head, then wired to an electrical commutator (Dragonfly Inc.). The signals from the commutator were fed through a 16-channel amplifier (A-M Systems Model 3500) with a gain of 100 and low-pass filtered at 300 Hz, next to a National Instrument A/D board, sampled at 2048 S^{-1} per channel. Continuous data acquisition was done using IgorPro 6 NIDAQ tool (Wavematrix).

The activities of animals were monitored by an infrared USB camera that was mounted above the recording setup and provided a top view of the mouse habitat. Activities were recorded continuously with an open source software iSpy (DeveloperInABox), which calculates in real time the percentage deviation between consecutive frames and generates a text file (activity data) containing time-stamped information on the percentages of frame-to-frame deviation values. The threshold for movement detection of the software was set to 80.

4.3.4 Data analysis and determination of sleep cycles

All LFP recordings were stored as .bin files, and activities extracted from videos as .xml text files. Files were then loaded by a customized Igor procedure, which can automatically divide the LFPs and activity files into 12 h episodes (Light cycle: 6AM-6PM; Dark cycle: 6PM-6AM). Data analyses on LFP recordings were done using custom written procedures in IgorPro 6.37 (Wavematrics) with its built-in functions for RMS (root mean square) measurement, FIR (finite impulse response) filtering, FFT (fast Fourier transform), Hilbert amplitude, continuous wavelet transform, etc.

The objective determination of sleep cycles relies on the ratio among δ, θ, and ϒ component objectively detected in the LFPs recorded from hippocampal CA1 pyramidal cell layer, together with the activities of the animals obtained from the activity files generated by the iSpy software. The method was described in a previous SfN poster (Molnár et al., 2017). Firstly, raw signals (sampled at 2048 s^{-1} and low-pass filtered at 300 Hz) were filtered in the δ band (1-4 Hz), θ band (5-12 Hz), and ϒ band (30-120 Hz). Filtering was done with a FIR filter with 4001 coefficients. The band-pass filtered traces were used for calculating the RMS values of δ and ϒ bands for the initial determination of NREM (non-rapid eye movement) epochs(Brankačk et al., 2010). Briefly, the RMS of ϒ and δ filtered waves were plotted for continuous 12 h (44,300 s) periods, and the all-point histograms of $ϒ_{RMS}/δ_{RMS}$ were plotted. These histograms had bimodal distributions and were best fitted with two Gaussians. The Gaussian with the smaller mean and variance was used for the initial identification of the NREM periods, generating NREM binary files with NREM epochs designated as 1. The NREM binary files were further corrected through convoluting suprathreshold $γ_{RMS}$ events and the percent of γ activity during the initial NREM events. To separate REM (rapid eye movement) and AWAKE epochs outside of the NREM

periods, the RMS of θ and δ filtered traces were calculated for continuous 12 h periods. Again, the all-point histogram of $\theta_{RMS}/\delta_{RMS}$ showed bimodal distribution and could be best fitted with two Gaussians. The threshold for separation was determined as the intersection of the two Gaussians(Ashman et al., 1994), and events above the threshold were categorized as REM. Finally, the separation of NREM, REM, and AWAKE was refined with the activity (Act) files: original REM segments (from the $\theta_{RMS}/\delta_{RMS}$ separation) where the Act > median Act were reclassified as AWAKE; original AWAKE segments (from $\Upsilon_{RMS}/\delta_{RMS}$ separation) where the Act < median Act were reclassified as REM. In this way, the NREM, REM, and AWAKE periods were separated while no subjective thresholds were used.

4.4 Results

4.4.1 Disturbed sleeping cycles were observed in 11 m-old, but not 7.5 m-old App$^{NL-F/NL-F}$ mice.

We have implanted bilaterally into CA1 stratum pyramidale in 7 m-old *App$^{NL-F/NL-F}$* (DOB: 10/31/16) and 7.5 m-old WT mice (DOB: 10/15/16). All surgeries were done on the same day (06/05/17). Also recordings from 3 WT mice aged 6-8 m used for previous projects in the lab were used as controls in the sleep cycle analysis. After recovery (10 days), mice were connected to the long-term recording setup and LFP and video recordings were continuously acquired for 5 days. About 3.5 months later, the animals were connected again for 5 days of LFP and activity recordings. At the time of the first recording, the mice were at ~7.5 m of age; while at the second recording, they were at ~11 m old. In this way, we could catch an important period for pathological progression in these mice, because according to our DAB stain analysis on the AD homozygous mice, they began to accumulate extensive plaque deposition in the hippocampus around 8-12 m (see **Chapter II Fig. 2.1**).

Indeed, when we objectively separated different states, namely NREM (non-rapid eye movement), REM (rapid eye movement), and AWAKE, of the animals with objective criteria implemented through automated Igor programs (see **Method**), we found that astounding changes had happened during the 3.5 m between the first and second recordings in one of the NL-F homozygous mice. **Fig. 4.1** shows the hourly fraction (%) of time spent in NREM and REM during three consecutive light and dark (with horizontal grey bars below) cycles in WT (**Fig. 4.1a;** N=4 mice; age = 6-8 m) and an *App*$^{NL-F/NL-F}$ mouse at 7.5 m (**Fig. 4.1b**) and 11 m (**Fig. 4.1c**) of age. Firstly, there was a significant increase in the percent time spent in NREM sleep during the dark cycle (6PM-6AM) in the homozygous mouse at 11 m-old (Dark cycle: average time spent in NREM=22.5% vs. 21.3% vs. 41.8%; WT vs. 7.5 m homo vs. 11 m homo), indicating that this mouse spent more time sleeping during their active phases as they aged. The percent time in NREM during the light cycle (6AM-6PM) did not alter between the two recordings (Light cycle: average time spent in NREM=45.4% vs. 57.1% vs. 55.1%; WT vs. 7.5 m vs. 11 m). Secondly, the ratio of REM sleep to the total sleep time (REM/TST) in both the dark and the light cycle were reduced in the second recording (Light cycle: REM/TST=1:6.1 vs. 1:5.4 vs. 1:7.1; Dark cycle: REM/NREM=1:6.6 vs. 1:6.1 vs. 1:10.1; in WT, 7.5 m homo, and 11 m homo, respectively), indicating less time spent in REM during the entire sleep cycle with the disease progression.

Both NREM and REM sleep are important for the consolidation of different types of memories(Maquet, 2001; Walker and Stickgold, 2006). Our results in 11 m-old *App*$^{NL-F}$ mice showing increased time in NREM sleep during the dark cycle is consistent with more daytime nap in AD patients(Bliwise, 1993; Horvath et al., 2017); while decreased percentage of REM sleep is consistent with human research as well, given that REM sleep is specifically affected in AD patients compared to normal elderly(Prinz et al., 1982a, 1982b; Vitiello et al., 1990; Moe et al., 1995; Bombois et al., 2010) . Moreover, the sleep disruptions we have observed emerged

during an important pathological stage when Aβ deposition started to accumulate in hippocampal CA1 pyramidal cell layer. Considering the reciprocal interactions between sleep disturbances and amyloid plaque deposition, on one hand the Aβ deposits may worsen the sleep cycle imbalance; on the other hand the sleep disruptions may accelerate Aβ deposition and contribute to the disease progression and later-on overt clinical symptoms such as cognitive decline.

4.4.2 Sharp wave ripples evolving into spikes were discovered in 11 m-old App$^{NL-F/NL-F}$ mice.

When we filtered the raw LFP recordings from hippocampal CA1 pyramidal cell layer between 120-180 Hz, we found SWRs that typically lasted ~50 ms in the WT mouse (**Fig. 4.2a**). In our LFP recordings at the second time point, when the *App*$^{NL-F/NL-F}$ mouse was 11 m old, we have observed SWRs with abnormally long durations (~200 ms) in the filtered trace (**Fig. 4.2b**, black line) as well as highly synchronous strong oscillations in bilateral CA1 LFPs (**Fig. 4.2b**, blue and red lines). These prolonged SWR episodes could be an early sign of highly synchronous SWRs turning into pathological events such as epileptiform discharges under even minor perturbations during disease progression. Indeed, spikes were observed in bilateral CA1 either after a seemingly normal SWR (**Fig. 4.2c**) or appearing alone (**Fig. 4.2d**), and they could later recruit more and more neurons into these synchronous discharges eventually leading to overt seizures. Specifically, this transition happened during a critical period, when extensive plaque deposition starts to expand from the cortex to the hippocampal layers (see Chapter II **Fig. 2.1**), including stratus radiatum from where the sharp waves originate and stratum pyramidale from where ripples were observed in our recordings. Moreover, in the 11 m-old homozygous mouse, spikes were mostly detected during reduced physical activities in the light cycle (inactive phase) (**Fig. 4e**), which was highly likely the NREM sleep. This is consistent with the research in AD patients by Lam *et al*. where they detected clinically silent hippocampal seizures and epileptiform spikes

during sleep(Lam et al., 2017) and research by Horváth *et al*. showing that 82% of epileptiform discharges occurred during sleep, mainly related to non-REM sleep(Horváth et al., 2017).Given the important role of NREM sleep in memory consolidation, especially for declarative memories(Maquet, 2001; Walker and Stickgold, 2006), the appearance of single spikes and later-on more severe epileptiform activities could substantially disrupt information processing and lead to further cognitive decline.

4.5 Discussion

Here in the App^{NL-F} mice, we have done long-term (>3 days) recordings of both LFP in CA1 pyramidal cell layer and the activities of the animals. Combining information from the LFPs (mainly the ratios among δ, θ, and ϒ band oscillations) and the activity files, we have developed a reliable novel method to determine different states of mice, namely REM sleep, NREM sleep and AWAKE, which allowed us to examine potential sleep disturbances in these AD mice at different ages during the disease progression. Results indicated that at 7.5 m of age, the homozygous $App^{NL-F/NL-F}$ mouse showed similar sleep cycles as control WT, while at 11 m of age the same mouse exhibited disrupted sleep cycles with more NREM sleep during the active phases and less REM sleep within the total sleep time. We have also discovered prolonged SWR episodes with spikes in between in the homozygous mouse at 11 m of age. These episodes could be the early transition of SWRs to epileptiform discharges, which are prominent in various mouse models of AD as well as in AD patients.

The pathological changes we have seen from the *in vivo* LFPs in the aged homozygous AD mouse, including sleep disturbances, altered SWRs, and subsequent spikes, have mutual interplay with other symptoms in AD, such as amyloid plaque deposition and cognitive decline. Firstly, AD patients with sleep disturbances seem to have a more severe cognitive

decline(Vitiello and Prinz, 1989; McCurry et al., 2000); in turn, sleep cycle regulates the level of Aβ deposition in mouse models of AD, where chronic sleep restriction led to a two-fold increase in plaque burden(Kang et al., 2009). Secondly, under pathological conditions, ripples could turn into PHFOs or strongly synchronous epileptic spikes(Bragin et al., 1999b; Staba and Bragin, 2011; Staba et al., 2012), and epileptiform discharges in the brain may contribute to the deterioration of cognitive functions on themselves without overt seizures(Buzsáki et al., 1991). Thirdly, Aβ burden in the medial prefrontal cortex is shown to lead to NREM sleep fragmentation (Roh et al., 2012), which may impair SWRs that are associated with NREM sleep, and then lead to memory decline. All of these and other interconnected changes in the brain may affect each other and contribute to the clinical symptoms observed in AD.

Although so far we have only finished the analyses on one homozygous mouse and an age-matched controls at two different time points, the results are promising. There are more recordings waiting to be analyzed, and also recordings from even older *App*$^{NL-F}$ homozygous and heterozygous mice (over 2 y old). We have recorded when the animal was 7.5 m old and then 3 months later and observed prominent changes in sleep and SWRs, and we could perform further recordings later to see whether there are more alterations occurring with the disease progression.

4.6 Acknowledgements

I would like to give my gratitude to Dr. László Molnár and Dr. Istvan Mody for developing the method for sleep cycle analysis. I would like to thank Dr. Isabella Ferando and Nadia Cusini for showing me the mouse surgery techniques and setting up the *in vivo* recording system. Also I want to thank Reyes Main Lazaro for his expertise in animal care.

Figures

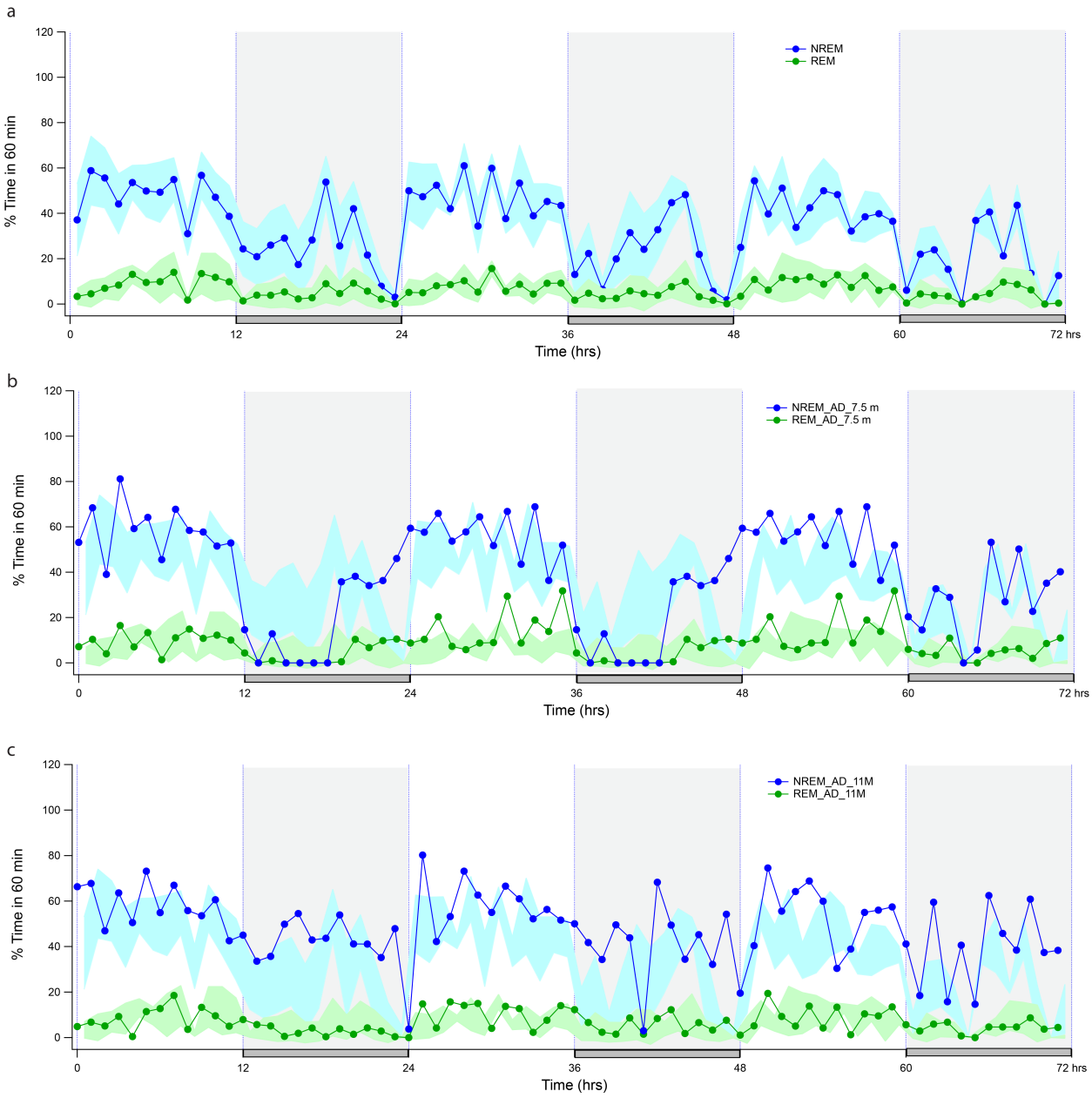

Figure 4.1: Percent time spent in NREM sleep (blue) and REM sleep (green) in WT (N=4 mice; age=6-8 m) (**a**), and the *App*$^{NL\text{-}F/NL\text{-}F}$ mouse at 7.5 m (**b**) and 11 m (**c**) of age.

Data is presented as the mean (solid circles) of percent time spent in each state calculated every 60 min over 3 full days (72 hrs). Grey bars under the horizontal axis indicate dark cycles

(6PM-6AM). Colored bands in **a** indicate the SD for the 4 WT mice, which are shown in **b** and **c** as well for the comparison between the WT mice and the *App*$^{NL\text{-}F/NL\text{-}F}$ mouse.

a

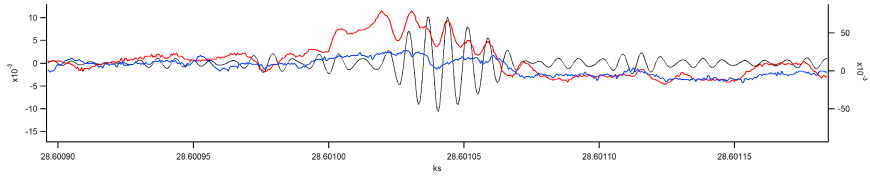
x10^-3
x10^-3
28.60090
28.60095
28.60100
28.60105
28.60110
28.60115
ks

b

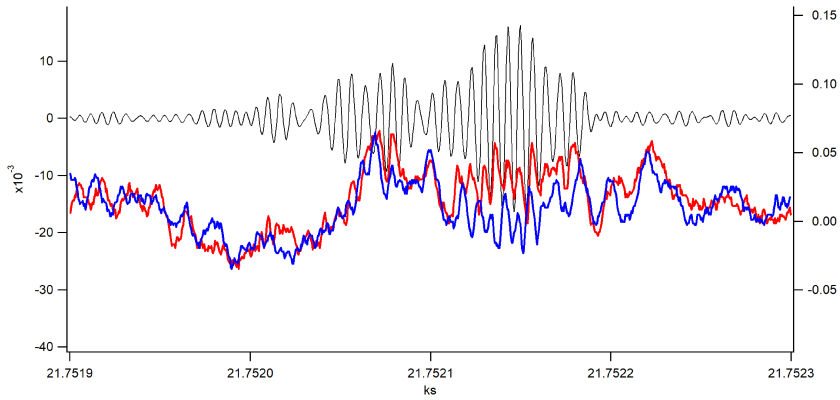
x10^-3
21.7519
21.7520
21.7521
21.7522
21.7523
ks

c

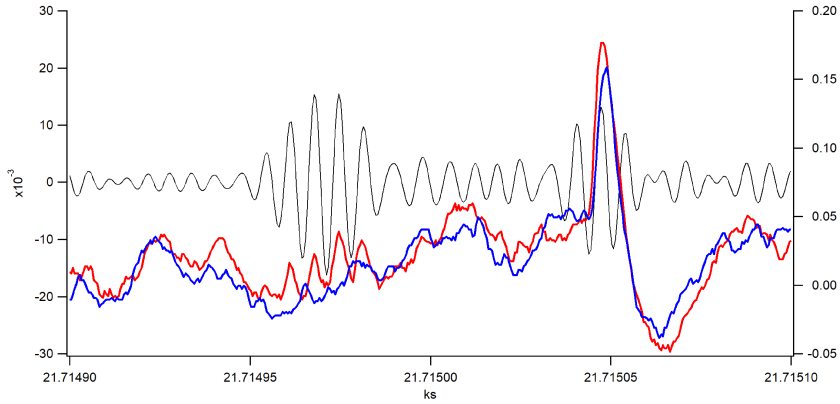
x10^-3
21.71490
21.71495
21.71500
21.71505
21.71510
ks

d

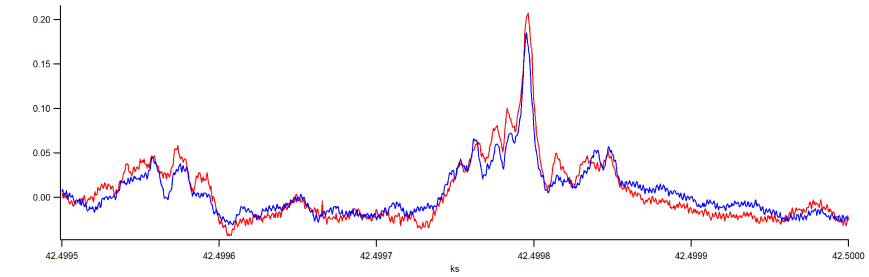
42.4995
42.4996
42.4997
42.4998
42.4999
42.5000
ks

e

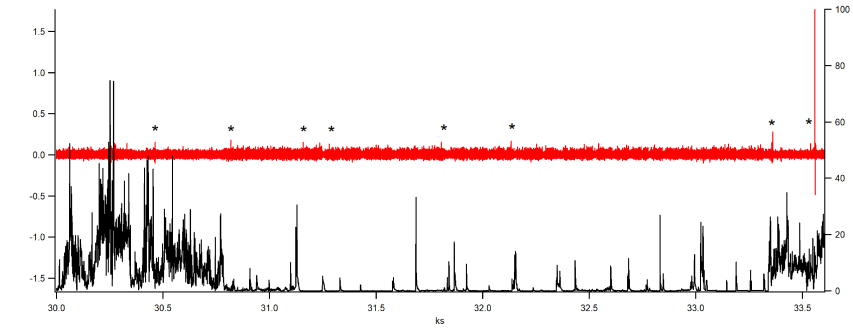
30.0
30.5
31.0
31.5
32.0
32.5
33.0
33.5
ks

Figure 4.2: Sharp wave ripples (SWRs) in the 11.5 m-old WT mouse (**a**) and altered SWRs and spikes in the 11 m-old *App*$^{NL\text{-}F/NL\text{-}F}$ mouse (**b-e**). (**a-d**) Blue and red lines show the two-channel raw LFPs from bilateral hippocampal CA1 stratum pyramidale. (**a-c**) Black lines show the 120-150 Hz filtered traces from one channel, indicting the occurrence of SWRs. Notice the high synchrony between the two channels in (**b-d**).

(**a**) Normal SWRs detected in the WT mouse that lasted around 50 ms. (**b**) Prolonged SWRs in the 11 m-old homozygous mouse that lasted about 200 ms. (**c**) SWRs followed by a spike in the 11 m-old homozygous mouse. (**d**) Example of a spike detected in bilateral hippocampal CA1 recordings in the 11 m-old homozygous mouse. (**e**) The spikes occurring during reduced activity in the light cycle in the 11 m-old homozygous mouse. Red line: raw LFP recording; Black line: activity level of the animal; Asterisks: detected spikes.

Bibliography

Alvarado-Rojas C, Huberfeld G, Baulac M, Clemenceau S, Charpier S, Miles R, Menendez De La Prida L, Le Van Quyen M (2015) Different mechanisms of ripple-like oscillations in the human epileptic subiculum. Ann Neurol 77:281–290.

Ashman KM, Bird CM, Zepf SE (1994) Detecting Bimodality in Astronomical Datasets.

Bakker A, Krauss GL, Albert MS, Speck CL, Jones LR, Stark CE, Yassa MA, Bassett SS, Shelton AL, Gallagher M (2012) Reduction of Hippocampal Hyperactivity Improves Cognition in Amnestic Mild Cognitive Impairment. Neuron 74:467–474.

Barth AMI, Ferando I, Mody I (2014) Ovarian cycle-linked plasticity of δ-GABAA receptor subunits in hippocampal interneurons affects Î^3 oscillations in vivo. Front Cell Neurosci 8:222.

Bliwise DL (1993) Sleep in normal aging and dementia. Sleep 16:40–81.

Bliwise DL (2004) Sleep disorders in Alzheimer's disease and other dementias. Clin Cornerstone 6 Suppl 1A:S16-28.

Bombois S, Derambure P, Pasquier F, Monaca C (2010) Sleep disorders in aging and dementia. J Nutr Health Aging 14:212–217.

Born HA (2015) Seizures in Alzheimer's disease. Neuroscience 286:251–263.

Born HA, Kim J-Y, Savjani RR, Das P, Dabaghian YA, Guo Q, Yoo JW, Schuler DR, Cirrito JR, Zheng H, Golde TE, Noebels JL, Jankowsky JL (2014) Genetic suppression of transgenic APP rescues Hypersynchronous network activity in a mouse model of Alzeimer's disease. J Neurosci 34:3826–3840.

Bragin a, Engel J, Wilson CL, Fried I, Buzsáki G (1999a) High-frequency oscillations in human brain. Hippocampus 9:137–142.

Bragin A, Engel J, Wilson CL, Fried I, Mathern GW (1999b) Hippocampal and entorhinal cortex high-frequency oscillations (100--500 Hz) in human epileptic brain and in kainic acid--treated rats with chronic seizures. Epilepsia 40:127–137.

Brankačk J, Kukushka VI, Vyssotski AL, Draguhn A (2010) EEG gamma frequency and sleep–wake scoring in mice: Comparing two types of supervised classifiers.

Buzsáki G (1984) Long-term changes of hippocampal sharp-waves following high frequency afferent activation. Brain Res 300:179–182.

Buzsáki G (1986) Hippocampal sharp waves: Their origin and significance. Brain Res 398:242–252.

Buzsáki G (2015) Hippocampal sharp wave-ripple: A cognitive biomarker for episodic memory and planning. Hippocampus 25:1073–1188.

Buzsáki G, Horvath Z, Urioste R (1992) High-Frequency Network Oscillation in the Hippocampus Author (s): György Buzsáki , Zsolt Horváth , Ronald Urioste , Jamille Hetke and Kensall Wise Published by : American Association for the Advancement of Science Stable URL : http://www.jstor.org/stabl. Science (80-) 256:1025–1027.

Buzsáki G, Hsu M, Slamka C, Gage FH, Horváth Z (1991) Emergence and propagation of interictal spikes in the subcortically denervated hippocampus. Hippocampus 1:163–180.

Buzsáki G, Lai-Wo S. L, Vanderwolf CH (1983) Cellular bases of hippocampal EEG in the behaving rat. Brain Res Rev 6:139–171.

Cardin JA, Carlén M, Meletis K, Knoblich U, Zhang F, Deisseroth K, Tsai L-H, Moore CI (2009) Driving fast-spiking cells induces gamma rhythm and controls sensory responses. Nature 459:663–667.

Chin J, Scharfman HE (2013) Shared cognitive and behavioral impairments in epilepsy and Alzheimer's disease and potential underlying mechanisms. Epilepsy Behav 26:343–351.

Fisher SP, Black SW, Schwartz MD, Wilk AJ, Chen TM, Lincoln WU, Liu HW, Kilduff TS, Morairty SR (2013) Longitudinal analysis of the electroencephalogram and sleep phenotype in the R6/2 mouse model of Huntington's disease. Brain 136:2159–2172.

Funato H et al. (2016) Forward-genetics analysis of sleep in randomly mutagenized mice. Nature 539:378–383.

Gillespie AK, Jones EA, Lin Y-H, Carr JS, Frank LM, Huang Correspondence Y, Karlsson MP, Kay K, Yoon SY, Tong LM, Nova P, Huang Y (2016) Apolipoprotein E4 Causes Age-Dependent Disruption of Slow Gamma Oscillations during Hippocampal Sharp-Wave Ripples.

Hoe HS, Lee HK, Pak DTS (2012) The upside of APP at synapses. CNS Neurosci Ther 18:47–56.

Holmes GL, Lenck-Santini P-P (2006) Role of interictal epileptiform abnormalities in cognitive impairment. Epilepsy Behav 8:504–515.

Horváth A, Szűcs A, Barcs G, Kamondi A (2017) Sleep EEG Detects Epileptiform Activity in Alzheimer's Disease with High Sensitivity Lebowitz B, ed. J Alzheimer's Dis 56:1175–1183.

Horvath A, Szucs A, Csukly G, Sakovics A, Stefanics G, Kamondi A (2017) EEG and ERP biomarkers of Alzheimer's disease: A critical review. Front Biosci Landmark 23:183–220.

Iaccarino HF, Singer AC, Martorell AJ, Rudenko A, Gao F, Gillingham TZ, Mathys H, Seo J, Kritskiy O, Abdurrob F, Adaikkan C, Canter RG, Rueda R, Brown EN, Boyden ES, Tsai L-H (2016) Gamma frequency entrainment attenuates amyloid load and modifies microglia. Nature 540:230–235.

Kang J-E, Lim MM, Bateman RJ, Lee JJ, Smyth LP, Cirrito JR, Fujiki N, Nishino S, Holtzman DM (2009) Amyloid-beta dynamics are regulated by orexin and the sleep-wake cycle. Science 326:1005–1007.

Kleen JK, Scott RC, Holmes GL, Lenck-Santini PP (2010) Hippocampal interictal spikes disrupt cognition in rats. Ann Neurol 67:250–257.

Korotkova T, Fuchs EC, Ponomarenko A, von Engelhardt J, Monyer H (2010) NMDA receptor ablation on parvalbumin-positive interneurons impairs hippocampal synchrony, spatial representations, and working memory. Neuron 68:557–569.

Kreuzer M, Polta S, Gapp J, Schuler C, Kochs EF, Fenzl T (2015) Sleep scoring made easy - Semi-automated sleep analysis software and manual rescoring tools for basic sleep

research in mice. MethodsX 2:232–240.

Lalonde R, Dumont M, Staufenbiel M, Strazielle C (2005) Neurobehavioral characterization of APP23 transgenic mice with the SHIRPA primary screen. Behav Brain Res 157:91–98.

Lam AD, Deck G, Goldman A, Eskandar EN, Noebels J, Cole AJ (2017) Silent hippocampal seizures and spikes identified by foramen ovale electrodes in Alzheimer's disease. Nat Med 23:678–680.

Lampert T, Plano A, Austin J, Platt B (2015) On the identification of sleep stages in mouse electroencephalography time-series. J Neurosci Methods 246:52–64.

Le Van Quyen M, Staba R, Bragin A, Dickson C, Valderrama M, Fried I, Engel J (2010) Large-Scale Microelectrode Recordings of High-Frequency Gamma Oscillations in Human Cortex during Sleep. J Neuropsychiatry Clin Neurosci 30:7770–7782.

Lim MM, Gerstner JR, Holtzman DM (2014) The sleep–wake cycle and Alzheimer's disease: what do we know? Neurodegener Dis Manag 4:351–362.

Mann EO, Paulsen O (2007) Role of GABAergic inhibition in hippocampal network oscillations. Trends Neurosci 30:343–349.

Maquet P (2001) The role of sleep in learning and memory. Science 294:1048–1052.

McCurry SM, Reynolds CF, Ancoli-Israel S, Teri L, Vitiello M V. (2000) Treatment of sleep disturbance in Alzheimer's disease. Sleep Med Rev 4:603–628.

Moe K, Vitiello M, Larsen L, Prinz P (1995) Symposium: Cognitive processes and sleep disturbances: Sleep/wake patterns in Alzheimer's disease: relationships with cognition and function. J Sleep Res 4:15–20.

Molnár L, Ferando I, Mody I. Determination of awake and sleep stages using objective detection criteria and analyses of long-term continuous intrahippocampal LFP recordings and video activity measures in mice. Program No. 346.14. 2017 Neuroscience Meeting Planner. Washington, DC: Society for Neuroscience, 2017. Online.

Musiek ES, Xiong DD, Holtzman DM (2015) Sleep, circadian rhythms, and the pathogenesis of

Alzheimer disease. Exp Mol Med 47:e148.

Nakazono T, Lam TN, Patel AY, Kitazawa M, Saito T, Saido TC, Igarashi KM (2017) Impaired In Vivo Gamma Oscillations in the Medial Entorhinal Cortex of Knock-in Alzheimer Model. Front Syst Neurosci 11:1–13.

Nilsson P, Saito T, Saido TC (2014) New mouse model of Alzheimer's. ACS Chem Neurosci 5:499–502.

Noebels J (2011) A perfect storm: Converging paths of epilepsy and Alzheimer's dementia intersect in the hippocampal formation. Epilepsia 52 Suppl 1:39–46.

O'Keefe J (1976) Place units in the hippocampus of the freely moving rat. Exp Neurol 51:78–109.

Palop JJ, Chin J, Roberson ED, Wang J, Thwin MT, Bien-Ly N, Yoo J, Ho KO, Yu G-Q, Kreitzer A, Finkbeiner S, Noebels JL, Mucke L (2007) Aberrant excitatory neuronal activity and compensatory remodeling of inhibitory hippocampal circuits in mouse models of Alzheimer's disease. Neuron 55:697–711.

Palop JJ, Mucke L (2009) Epilepsy and cognitive impairments in Alzheimer disease. Arch Neurol 66:435–440.

Peter-Derex L, Yammine P, Bastuji H, Croisile B (2015) Sleep and Alzheimer's disease. Sleep Med Rev 19:29–38.

Priller C, Thomas B, Gerda M, Krebs B, Kretzschmar HA, Herms J (2006) Synapse Formation and Function Is Modulated by the Amyloid Precursor Protein. J Neurosci 26:7212–7221.

Prinz PN, Pekind ER, Vitaliano PP, Raskind MA, Eisdorfer C, Zemcuznikov HN, GERBER CJ (1982a) Changes in the Sleep and Waking EEGs of Nondemented and Demented Elderly Subjects. J Am Geriatr Soc 30:86–92.

Prinz PN, Vitaliano PP, Vitiello M V, Bokan J, Raskind M, Peskind E, Gerber C (1982b) Sleep, EEG and mental function changes in senile dementia of the Alzheimer's type. NeurobiolAging 3:361–370.

Rao SC, Dove G, Cascino GD, Petersen RC (2009) Recurrent seizures in patients with dementia: frequency, seizure types, and treatment outcome. Epilepsy Behav 14:118–120.

Roh JH, Huang Y, Bero AW, Kasten T, Stewart FR, Bateman RJ, Holtzman DM (2012) Disruption of the sleep-wake cycle and diurnal fluctuation of β-amyloid in mice with Alzheimer's disease pathology. Sci Transl Med 4:150ra122.

Saito T, Matsuba Y, Mihira N, Takano J, Nilsson P, Itohara S, Iwata N, Saido TC (2014) Single App knock-in mouse models of Alzheimer's disease. Nat Neurosci 17:661–663.

Saito T, Matsuba Y, Yamazaki N, Hashimoto S, Saido TC (2016) Calpain Activation in Alzheimer's Model Mice Is an Artifact of APP and Presenilin Overexpression. J Neurosci 36:9933–9936.

Sarkis RA, Dickerson BC, Cole AJ, Chemali ZN (2016) Clinical and Neurophysiologic Characteristics of Unprovoked Seizures in Patients Diagnosed With Dementia. J Neuropsychiatry Clin Neurosci 28:56–61.

Sasaguri H, Nilsson P, Hashimoto S, Nagata K, Saito T, De Strooper B, Hardy J, Vassar R, Winblad B, Saido TC (2017) APP mouse models for Alzheimer's disease preclinical studies. EMBO J 36:e201797397.

Scarmeas N, Honig LS, Choi H, Cantero J, Brandt J, Blacker D, Albert M, Amatniek JC, Marder K, Bell K, Hauser WA, Stern Y (2009) Seizures in Alzheimer disease: who, when, and how common? Arch Neurol 66:992–997.

Scharfman HE (2012) "Untangling" Alzheimer's disease and epilepsy. Epilepsy Curr 12:178–183.

Shatskikh TN, Raghavendra M, Zhao Q, Cui Z, Holmes GL (2006) Electrical induction of spikes in the hippocampus impairs recognition capacity and spatial memory in rats. Epilepsy Behav 9:549–556.

Sohal VS, Zhang F, Yizhar O, Deisseroth K (2009) Parvalbumin neurons and gamma rhythms enhance cortical circuit performance. Nature 459:698–702.

Staba RJ, Bragin A (2011) High-frequency oscillations and other electrophysiological biomarkers of epilepsy: underlying mechanisms. Biomark Med 5:545–556.

Staba RJ, Ekstrom AD, Suthana NA, Burggren A, Fried I, Engel J, Bookheimer SY (2012) Gray matter loss correlates with mesial temporal lobe neuronal hyperexcitability inside the human seizure-onset zone. Epilepsia 53:25–34.

Suzuki SS, Smith GK (1987) Spontaneous EEG spikes in the normal hippocampus. I. Behavioral correlates, laminar profiles and bilateral synchrony. Electroencephalogr Clin Neurophysiol 67:348–359.

Suzuki SS, Smith GK (1988a) Spontaneous EEG spikes in the normal hippocampus. II. Relations to synchronous burst discharges. Electroencephalogr Clin Neurophysiol 69:532–540.

Suzuki SS, Smith GK (1988b) Spontaneous EEG spikes in the normal hippocampus. III. Relations to evoked potentials. Electroencephalogr Clin Neurophysiol 69:541–549.

Verret L, Mann EO, Hang GB, Barth AMI, Cobos I, Ho K, Devidze N, Masliah E, Kreitzer AC, Mody I, Mucke L, Palop JJ (2012) Inhibitory interneuron deficit links altered network activity and cognitive dysfunction in Alzheimer model. Cell 149:708–721.

Vitiello M V, Prinz PN (1989) Alzheimer's disease. Sleep and sleep/wake patterns. Clin Geriatr Med 5:289–299.

Vitiello M V, Prinz PN, Williams DE, Frommlet MS, Ries RK (1990) Sleep disturbances in patients with mild-stage Alzheimer's disease. J Gerontol 45:M131-8.

Vossel KA, Beagle AJ, Rabinovici GD, Shu H, Lee SE, Naasan G, Hegde M, Cornes SB, Henry ML, Nelson AB, Seeley WW, Geschwind MD, Gorno-Tempini ML, Shih T, Kirsch HE, Garcia PA, Miller BL, Mucke L (2013) Seizures and Epileptiform Activity in the Early Stages of Alzheimer Disease. JAMA Neurol 70:1158.

Vossel KA, Ranasinghe KG, Beagle AJ, Mizuiri D, Honma SM, Dowling AF, Darwish SM, Van Berlo V, Barnes DE, Mantle M, Karydas AM, Coppola G, Roberson ED, Miller BL, Garcia

PA, Kirsch HE, Mucke L, Nagarajan SS (2016) Incidence and impact of subclinical epileptiform activity in Alzheimer's disease. Ann Neurol 80:858–870.

Vossel KA, Tartaglia MC, Nygaard HB, Zeman AZ, Miller BL (2017) Epileptic activity in Alzheimer's disease: causes and clinical relevance. Lancet Neurol 16:311–322.

Walker MP, Stickgold R (2006) Sleep, memory, and plasticity. Annu Rev Psychol 57:139–166.

Westmark CJ, Westmark PR, Beard AM, Hildebrandt SM, Malter JS (2008) Seizure susceptibility and mortality in mice that over-express amyloid precursor protein. Int J Clin Exp Pathol 1:157–168.

Wisor JP, Edgar DM, Yesavage J, Ryan HS, McCormick CM, Lapustea N, Murphy GM (2005) Sleep and circadian abnormalities in a transgenic mouse model of Alzheimer's disease: a role for cholinergic transmission. Neuroscience 131:375–385.

Yaghouby F, Sunderam S (2016) SegWay: A simple framework for unsupervised sleep segmentation in experimental EEG recordings. MethodsX 3:144–155.

Young-Pearse TL, Bai J, Chang R, Zheng JB, Loturco JJ, Selkoe DJ (2007) A Critical Function for β-Amyloid Precursor Protein in Neuronal Migration Revealed by In Utero RNA Interference. J Neurosci 27:14459–14469.

Zhang B, Veasey SC, Wood MA, Leng LZ, Kaminski C, Leight S, Abel T, Lee VM-Y, Trojanowski JQ (2005) Impaired rapid eye movement sleep in the Tg2576 APP murine model of Alzheimer's disease with injury to pedunculopontine cholinergic neurons. Am J Pathol 167:1361–1369.

Zheng H, Koo EH (2011) Biology and pathophysiology of the amyloid precursor protein. Mol Neurodegener 6:27.

Chapter V

Novel Insights into the Behavioral Analysis of Mice Subjected to the Forced-swim test

OPEN

Citation: Transl Psychiatry (2015) 5, e551; doi:10.1038/tp.2015.44

www.nature.com/tp

ORIGINAL ARTICLE

Novel insights into the behavioral analysis of mice subjected to the forced-swim test

L Chen[1,2], GC Faas[2], I Ferando[2] and I Mody[2,3]

The forced-swim test (FST) is one of the most widely used rodent behavioral assays, in which the immobility of animals is used to assess the effectiveness of antidepressant drugs. However, the existing, and mostly arbitrary, criteria used for quantification could lead to biased results. Here we believe we uncovered new confounding factors, revealed new indices to interpret the behavior of mice and propose an unbiased means for quantification of the FST.

Translational Psychiatry (2015) **5,** e551; doi:10.1038/tp.2015.44; published online 14 April 2015

INTRODUCTION

Major depressive disorder is a key public health concern. The results of the first Global Burden of Disease study in 1990 revealed a group of disorders that primarily cause nonfatal burden, quantified by years lived with disability and disability-adjusted life years.[1] According to data from the Global Burden of Disease study 2010,[2–4] mental and substance disorders accounted for 7.4% of disability-adjusted life years, and they were the leading cause (22.9%) of years lived with disability worldwide.[4] Within the mental and substance disorders group, major depressive disorder contributed most of the disability-adjusted life years and years lived with disability, with a global point prevalence of 4.7%.[5] From 1990 to 2010, the contribution of major depressive disorder increased by 37% to both disability-adjusted life years[3] and years lived with disability.[2] Also, major depressive disorder was predicted to be the second leading contributor to the burden of diseases by 2020.[6]

Clinically, depression is a heterogeneous disorder in humans, and it is difficult to model the psychological aspect of the disease in animals.[7] There are just a limited number of tests available for detecting a 'depressed' phenotype in rodents;[7–9] among those, the forced-swim test (FST) is one of the most widely used tests across laboratories for assessing symptoms of depression. FST was originally introduced by Porsolt *et al.* in rats[10,11] and mice[12] for the screening of antidepressants. In this test, if treatment with a drug reduced behavioral immobility,[10,12,13] thought of as a measure of despair, the drug could be considered as an 'antidepressant'.[10–12] The advantages of the FST consist of its ease of use, reliability across different laboratories and trials and the ability to detect a broad spectrum of antidepressants.[14,15] However, the test also has some drawbacks, such as its unreliability in the detection of the effects of selective 5-HT reuptake inhibitors (selective serotonin reuptake inhibitors), which is a major group of antidepressant drugs.[13] Another important question is how to interpret the immobility of the animals in the FST. Researchers have been arguing that immobility is largely dependent on learning and memory in the rat FST,[14,16] but only limited research has been done on the role of cognitive processes in the mouse FST. As the FST was originally developed for rats, a species much better adapted to water than mice, some technical issues remain related to using mice in FST, a species for which the test remains to be adequately adapted.[7,8] In Porsolt's original FST for rats, the animals will go through two exposures.[10,11] The first exposure was to induce a stable level of immobility, and the second exposure was to quantify the immobility after drug or vehicle treatment, whereas for reasons yet unclear, mice show a sufficiently stable level of immobility during the last 4 min of a 6-min swim test.[13] Also, particularly in mice, the immobility may be influenced by factors other than a variation in emotional state,[17] which renders the interpretation of the results dependent on the strain of mice,[18–20] the water temperature[21,22] or possibly other factors. Despite the disadvantages inherent to carrying out FST in mice and the inability to really measure depression, the test is still widely used as some quantification of depressive behavior. The ability and potential to modify mice genetically, thus enabling better insights into molecular mechanisms underlying mental disorders, has created a demand for better adapting the test to this rodent species. To date, almost 40 strains of mice have been generated with a depression or antidepressant-related phenotype.[7]

Over the years, researchers have made modifications to the FST to enhance its sensitivity, specificity and reliability.[15,17,23–25] In this study, we set out to determine whether it is possible to quantify some of the factors affecting the behavior of mice. First, we revealed buoyancy as a confounding factor in the FST. We also devised new unbiased quantitative measurements of the behavior of mice, including developing a systematic way to determine the latency to immobility, and discovering an oscillatory pattern of behaving mice in the FST.

MATERIALS AND METHODS

Animals

All animal use was approved by the UCLA Chancellor's Animal Research Committee. All mice used for the FST were on C57BL/6J background and were obtained directly from Jackson Labs or bred in the UCLA animal

[1]Molecular, Cellular and Integrative Physiology Interdepartmental Ph.D. Program, University of California Los Angeles, Los Angeles, CA, USA; [2]Department of Neurology, The David Geffen School of Medicine at UCLA, University of California Los Angeles, Los Angeles, CA, USA and [3]Department of Physiology, The David Geffen School of Medicine at UCLA, University of California Los Angeles, Los Angeles, CA, USA. Correspondence: Professor I Mody or Dr GC Faas, Department of Neurology, The David Geffen School of Medicine at UCLA, University of California Los Angeles, 635 Charles Young Drive S, NRB1 575D, Los Angeles, CA 90095, USA.
E-mail: mody@ucla.edu or gfaas@ucla.edu
Received 8 October 2014; revised 21 January 2015; accepted 26 January 2015

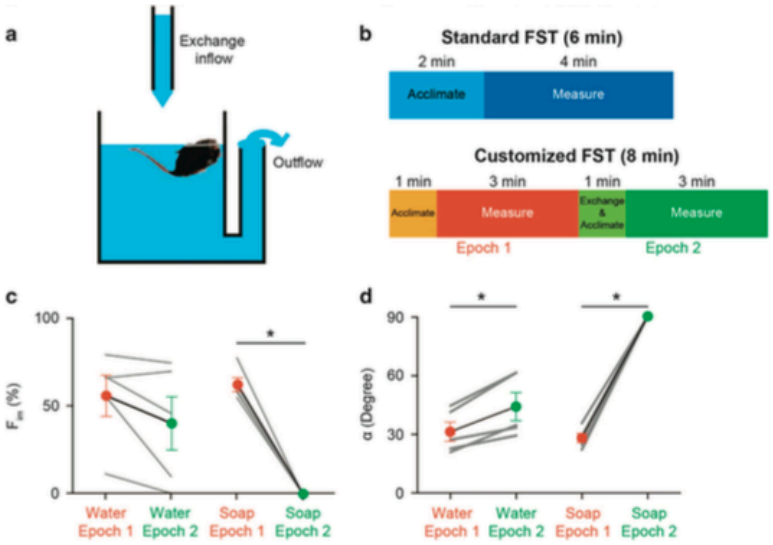

Figure 1. Customized setup for liquid exchange in the FST. (**a**) The diagram of the customized setup, showing the exchange inflow of the new liquid and the outflow of the original liquid in the container. (**b**) Two experiment protocols for the standard FST (6 min) and customized FST (8 min). (**c** and **d**) Exchanging water for 1 l of water ($n = 5$) or 0.5% soap solution ($n = 5$) using the customized setup. Fraction of total immobile time (F_{im}) (**c**) and angles (α) (**d**) of the animals both changed significantly after exchanging water for soap solution, going from epoch 1 (orange) to epoch 2 (green). The gray lines show the changes in individual mice from epoch 1 to epoch 2, and the colored filled circles show the averaged data in each epoch. FST, forced-swim test.

facilities. Mice were kept in the vivarium on a 12-h light/dark cycle with free access to water and food. Calbindin knockout (*Calb1*$^{-/-}$) mice weighing between 32 and 43 g (male, 62–70 weeks old) were used for the customized 8-min FSTs (see below). Alpha5 subunit containing $GABA_A$ receptor knockout heterozygous (*Gabra5*$^{+/-}$) mice (male and female, 10–13 weeks old) were used for some of the standard 6-min FSTs. For all other FSTs, wild-type (WT) mice weighing between 20 and 25 g (male, 10–18 weeks old) were used.

Standard 6-min FST

All 6-min FSTs were carried out using C57BL/6J mice (male and female, 8–70 weeks old, 20–43 g, see Animals section). The animals swam in standard 2 l glass beakers (diameter 13.1 cm) filled with water to 4.5 cm from the top so that the animals could neither touch the bottom with their tails, nor escape from the top. Before each test, the container was thoroughly cleaned. Water temperature was kept between 23 °C and 26 °C.[10–12,17] At the start of each test, an animal was gently picked up by its tail from the home cage and rapidly placed into the middle of the container. At the time the animal was placed in the water, the recording time was started and the duration of each standard FST was set to 6 min (for a customized FST, see below). The entire FST session was videotaped for later analysis (Figure 1b). After the test, the animal was removed from the water, dried with a towel and put into a warm cage (temperature of bedding 31–33 °C) for 15 min before returning to their home cage. All animals were first-time swimmers and none were used for multiple FSTs.

Customized 8-min FST

For the customized FST, the setup for the FST was adapted for liquid exchange (Figure 1a). The container was made of transparent plexiglass. It was designed to be large enough (diameter 14.6 cm, height 27.9 cm) so that the animals could neither touch the bottom with their tails, nor escape from the top. To keep the level of water constant in the container during a liquid exchange, a thick (diameter 2.6 cm) vertical plastic pipe was connected to the container at its side, making a communicating vessel structure with the container, so that any excess liquid above 21.0 cm from the bottom could flow out. A 1.0-cm diameter plastic inflow pipe was fixed above the container to allow the exchange of solutions. The inflow was positioned above the center of the container so that the incoming liquid would not disturb the swimming animals, as mice swim along the edge of the container. In this manner, the entire process of exchanging all of the 3 l capacity of the container could be done within 30 s (Figure 1b). In contrast to the 6-min FST with 2 min of acclimatization and 4 min for quantification, the 8-min FST had two swim epochs. In epoch 1, mice swam in water for 4 min. After this, epoch 2 started with a liquid exchange lasting < 30 s. After a total duration of 4 min for epoch 2, the animals were removed form the water and dried with a towel and put into a warm cage (temperature of bedding 31–33 °C) for 15 min before returning to their home cage. All the animals were first-time swimmers and none were used for multiple FSTs.

Analysis

(1) Definition of immobility. All FST videos were scored by one individual in a double-mask manner. The scores were assigned as '0' for immobility and '1' for mobility with a time resolution of 0.1 s. A mouse was considered immobile when floating and/or making only necessary movements to keep the balance of its body or to keep its head above the water.[10–13] According to the current standard of general FST analyses, latency to immobility (t_{lat}) was defined as the time from start to the first bout of immobility lasting longer than 1 s,[13] unless otherwise stated. Fractions of total immobile time (F_{im}) were calculated as the total immobile time divided by the total swimming time used to calculate the immobility.

(2) Scoring of the FSTs. For the standard FST (6 min), the first 2 min were considered a time for the animals to explore and acclimate to the environment. For the full 6 min, mobility/immobility were scored, but for the calculation of F_{im}, only the data of the last 4 min were used (F_{im} = total immobile time during the last 4 min/240 s). For the calculations involving the calculation of t_{lat}, data of all 6 min were used.

For the customized FST (8 min), the first 1 min at the start of each epoch was considered a time for the animals to explore and acclimate to the environment. In each epoch, the full 4 min mobility/immobility were scored, but for the calculation of F_{im}, only the data of the last 3 min were used (F_{im} = total immobile time during the last 3 min/180 s). For the calculations involving the calculation of t_{lat}, data of all 4 min in each epoch were used.

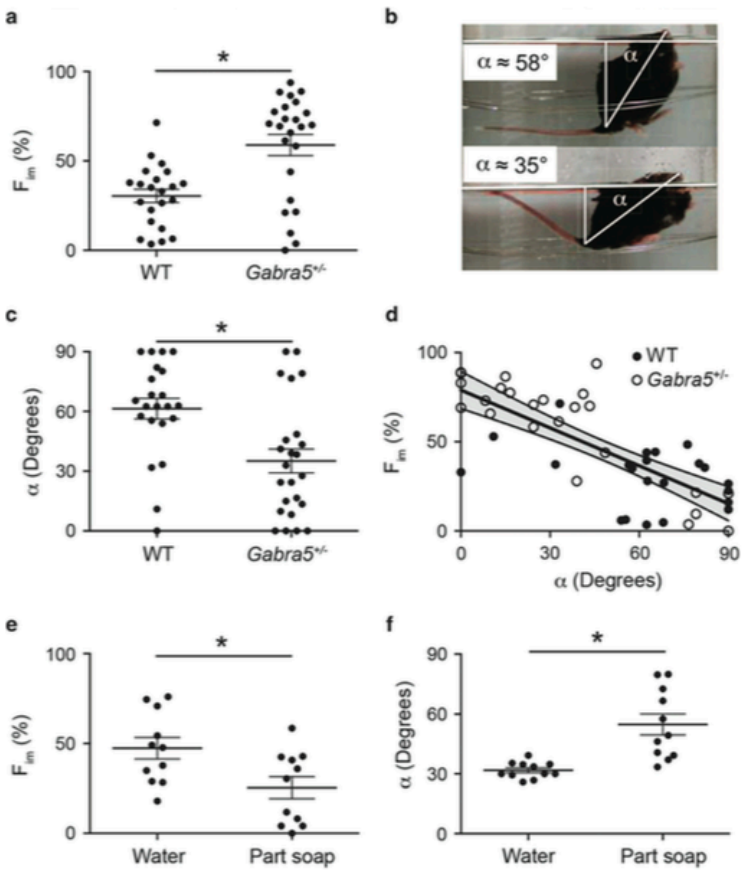

Figure 2. Strong inverse correlation between body posture angle in water and immobility. (**a**) Significant difference in the fractions of total immobile time (F_{im}) of WT ($n=22$) and *Gabra5*$^{+/-}$ ($n=24$) mice. (**b**) Two immobile mice with different angles (α) in water. White lines indicate how the angles were measured. Pictures of mice were taken in experiments shown in **e** and **f**. (**c**) Significant difference in α of WT and *Gabra5*$^{+/-}$ mice. (**d**) F_{im} plotted as a function of α shows a strong inverse correlation between α and F_{im}. (**e** and **f**) Significant difference in F_{im} (**e**) and α (**f**) of mice with water (Water, $n=11$) or 1% soap solution (Part soap, $n=11$) applied to their caudal areas. WT, wild-type.

(3) Angle during immobility. We defined the angle (α) of an immobile mouse with respect to the water surface. After the acclimatization period (2 min for standard FST, 1 min for each epoch of the customized FST), one frame was taken out from each video at the first moment when the mouse stopped swimming and was in full profile view. The angle α was determined using the depth of the base of the tail and the distance between the intersection of the body with the water and the base of the tail (white lines, Figure 2b).

(4) Defining new thresholds for screening the first critical immobility. The durations of bouts of immobility (t_{im}) were taken from the entire swim session of each mouse. The cumulative probability of the immobility durations ($\Phi(t_{im})$) was fitted with two cumulative normal distributions with the following equation:

$$\Phi(t_{im}) = A_1 \int_{-\infty}^{t_{im}} \frac{1}{\sqrt{2\pi\sigma_1^2}} e^{-(t_{im}-\mu_1)^2/2\sigma_1^2} + A_2 \int_{-\infty}^{t_{im}} \frac{1}{\sqrt{2\pi\sigma_2^2}} e^{-(t_{im}-\mu_2)^2/2\sigma_2^2},$$

where $A_1+A_2=1$.

In the equation, t_{im} is the duration of each bout of immobility; A, μ and σ are the amplitudes, means and standard deviations, respectively, of the two normal distributions. The distributions were fitted using the NORM.DIST function in Microsoft Office Excel 2011.

To make sure that the $\Phi(t_{im})$ of t_{im} can be fitted with two rather than one normal distribution, we did a F-test to validate whether two normal distributions fit the data significantly better than a single distribution. For the F-test, we fitted the $\Phi(t_{im})$ curves with both one and two normal distributions. When fitting with one distribution, $A_1=1$ and $A_2=0$ in the equation shown above. The *F*-values were calculated with the following equation:

$$F = \frac{\left(\frac{RSS_1 - RSS_2}{p_2 - p_1}\right)}{\left(\frac{RSS_2}{n - p_2}\right)},$$

in which RSS_1 and RSS_2 are the residual sums of squares from fitting with one and two normal distributions, respectively; p_1 and p_2 are the number of parameters used for fitting with one and two normal distributions, respectively; and n is the number of points used for fitting. According to the equation of the normal distribution, $p_1=2$ and $p_2=5$.

We then performed the F-test and calculated *P*-values were using the F.DIST function in Microsoft Office Excel 2011. As an example, for the mouse

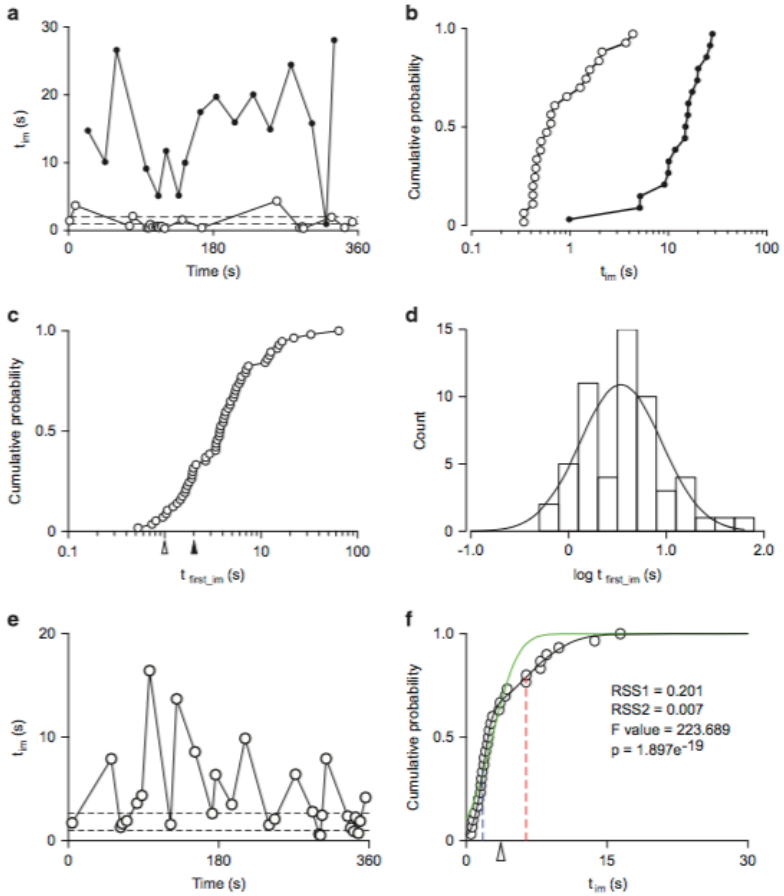

Figure 3. The distribution of the durations of bouts of immobility (t_{im}). (**a**) Examples of one mouse with longer t_{im}s (filled circles) and the other with shorter t_{im}s (open circles) during the entire swim session of 6 min. The t_{im}s are plotted against the time at which the immobility occurred. The two dashed lines show the traditional arbitrary thresholds of 1 s and 2 s for screening the first bout of immobility. (**b**) Cumulative probability of the t_{im}s of the two mice shown in **a**. (**c**) Cumulative probability of the t_{first_im}s of 57 mice used in the 6-min FST. The open and filled triangles show the traditional arbitrary thresholds of 1 s and 2 s, respectively, for the calculation of t_{iat}. (**d**) The histogram of the log values of all the t_{first_im}s shown in **c**. The histogram follows a log-normal distribution. (**e**) Immobility durations of a mouse (t_{im}) plotted against the time at which the immobility occurred during the 6-min FST. The two dashed lines show the traditional arbitrary thresholds of 1 s and 2 s for screening the first bout of immobility. (**f**) Cumulative probability of the t_{im}s shown in **a**. The open circles are fitted with either two normal distributions (black line) or one normal distribution (green line). The residual sum of squares (RSS) when fitting with one or two distributions are RSS1 = 0.201 and RSS2 = 0.007, respectively. The *F*-value calculated with RSS1 and RSS2 is 223.689 ($P = 1.897e^{-19}$). When fitting with two normal distributions, the blue dashed line is the mean of the first distribution, the red dashed line is the mean of the second distribution and the open triangle shows the new threshold (t_c) for screening the first critical immobility calculated as the weighted mean of the two distributions. FST, forced-swim test; t_c, critical threshold.

shown in Figure 3f, when we were fitting the $\Phi(t_{im})$ curve with one normal distribution (Figure 3f, green line), the RSS was RSS1 = 0.201, whereas the RSS decreased to RSS2 = 0.007 when fitting with two normal distributions (Figure 3f, black line). Accordingly, the *F*-value calculated from RSS1 and RSS2 was 223.689, and the *P*-value we got from the F-test was $1.897e^{-19}$, which means that two distributions fit the $\Phi(t_{im})$ curve significantly better than one distribution for this mouse.

Of the 68 mice used in our tests, only in 7 mice (~10%) two normal distributions failed to fit the data significantly better than a single normal distribution. Therefore, there are two distinct populations in the distributions of t_{im}s in 90% of the swim tests.

When fitting $\Phi(t_{im})$ with two normal distributions, the new threshold (t_c, critical threshold) for screening the first critical immobility was defined as a weighted mean as follows:

$$t_c = A_1 \times \mu_1 + A_2 \times \mu_2$$

In the equation, A and μ are the amplitudes and means, respectively, of the two normal distributions. For the seven cases with a single distribution, $t_c = \mu_1$ was used as the threshold value.

The new latency to immobility (t_{iat}) was then calculated as the latency to the first bout of immobility that was longer than t_c.

(5) Oscillations in swimming probability. The oscillations were determined using the Morlet wavelet transforms (Figures 4b and c) on the summed probability of being mobile (P_{mob}) plots (Figure 4a) after smoothing by a

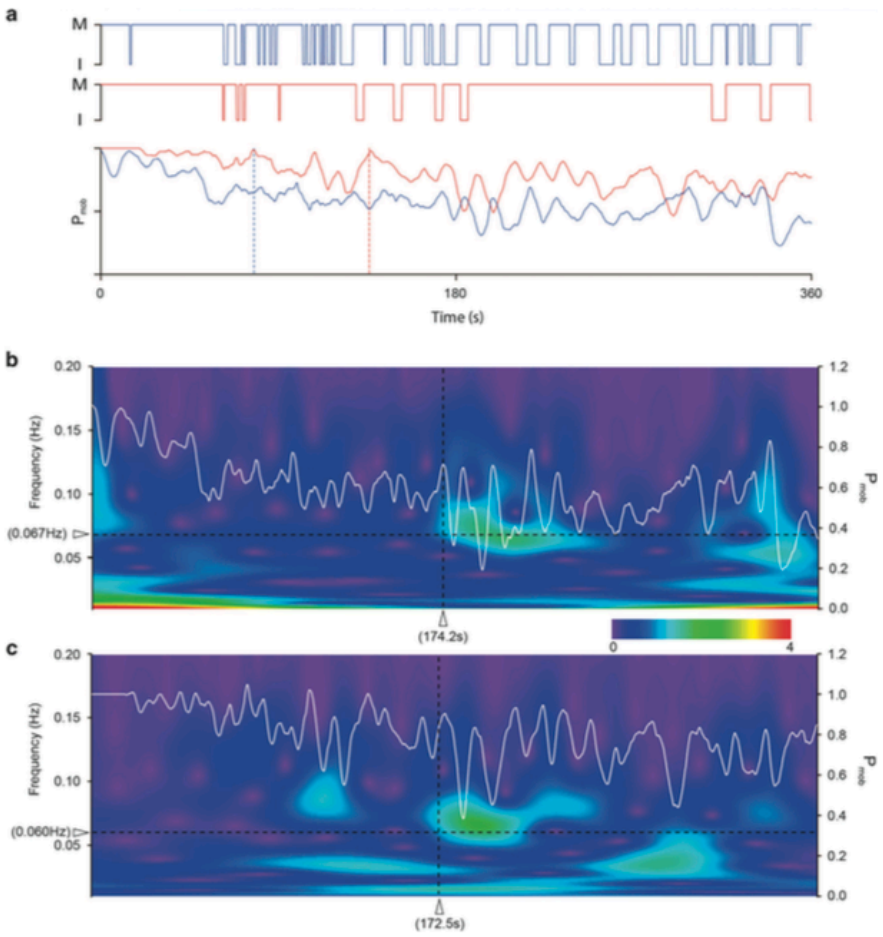

Figure 4. Probability of being mobile (P_{mob}) plots. (**a**) Probability of being mobile (P_{mob}) over the entire swim test shown in Figures 2e and f. The top two plots represent the binary states (M for mobile; I for immobile) of two individual mice with water (blue lines, top plot) or 1% soap solution (red lines, middle plot) applied to their caudal areas. The blue and red lines in the bottom plot represent the averages of the behavior, which is P_{mob}, of 11 mice in each group. The blue and red dashed lines show the averaged t_{lat}s calculated with t_cs obtained for each mouse in the two groups. (**b** and **c**) Morlet wavelet transform of the P_{mob} plots shown in **a**, where color intensity indicates amplitude of a certain frequency component (y axis) as a function of time (x axis) of the P_{mob} plots. The rainbow color bar shows the corresponding color scale for the oscillation amplitudes in arbitrary units. A strong 'oscillation' in the swimming probability (green areas indicating a repeated stop-and-swim behavior with a certain frequency) with a comparable average frequency (0.060 and 0.067 Hz) occurred at similar times (174.2 s and 172.5 s) in the P_{mob} plots of mice regardless whether water (**b**) or 1% soap solution (**c**) was applied to their caudal areas. Even if the animals would have similar oscillating behavior, if they were out of phase with each other, the oscillating behavior would not appear in the averages, that is, the P_{mob} plots. t_c, critical threshold; t_{lat}, latency to immobility.

fourth order Savitzky–Golay algorithm (Igor 64, WaveMetrics, Lake Oswego, OR, USA).

Statistics

All the results are expressed as mean ± s.e.m. Statistical differences between control groups and experimental groups were determined by unpaired two-tailed Mann–Whitney test unless otherwise stated. $P < 0.05$ was considered to be statistically significant.

Equipment

The behavior of mice during the swim test was recorded using a Casio Exilim camera (Dover, NJ, USA). The software used for scoring was Etholog (Eduardo B. Ottoni, University of São Paulo, São Paulo, Brazil). The Morlet wavelet transform was done in Igor Pro 6 (WaveMetrics). All other data analyses were done in Microsoft Excel for Mac 2011 and Prism 6 (GraphPad, La Jolla, CA, USA). Johnson's baby head-to-toe wash (Johnson & Johnson, Skillman, NJ, USA) was mixed with warm tap water (23–26 °C) to make a mild 0.5–1% soap solution. This soap solution was used in certain swim tests to reduce surface tension of the water, diminishing air trapped in the fur. Consequently the total buoyancy of animals in a soap solution will be decreased.

RESULTS

For research not specifically described here, WT and α5 subunit containing $GABA_A$ receptor heterozygous (*Gabra5*$^{+/-}$)

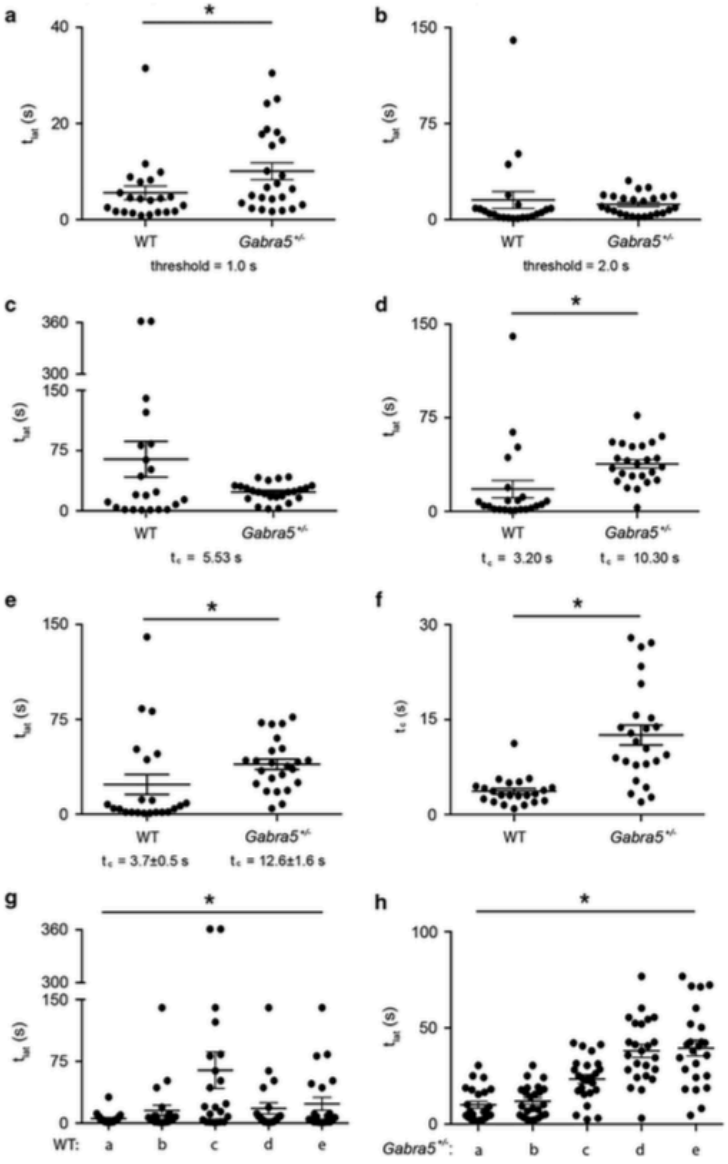

Figure 5. Thresholds for screening the first critical immobility. Latency to immobility (t_{lat}) in WT ($n = 22$) vs *Gabra5*$^{+/-}$ ($n = 24$) mice calculated with different thresholds. (**a**) Using the traditional threshold of 1 s for all the mice. (**b**) Using the traditional threshold of 2 s for all the mice. (**c**) Using a single t_c for all the mice. (**d**) Using a different t_c for each group of mice. (**e**) Using individual t_cs obtained for each mouse in a given group. (**f**) Significant difference between the individual t_cs of the two groups of mice. (**g** and **h**) Comparing t_{lat}s calculated with different thresholds for WT (**g**) and *Gabra5*$^{+/-}$ (**h**) mice. WT, wild-type; t_c, critical threshold.

mice were used in a standard 6-min FST (See Materials and Methods). There was a significant difference between the fractions of total immobile time (F_{im}) of WT and *Gabra5*$^{+/-}$ mice ($F_{im\_WT} = 30.4 \pm 3.7\%$ vs $F_{im\_Gabra5+/-} = 58.9 \pm 5.9\%$, $P = 0.0010$, Figure 2a). However, we also observed remarkable differences in the animals' floating postures, which we quantified by measuring the angles formed between the surface of the water and the animals' axis while immobile (α, Figure 2b, See Materials and Methods). In WT mice, α was significantly larger than in *Gabra5*$^{+/-}$ mice ($\alpha_{WT} = 61 \pm 5°$ vs $\alpha_{Gabra5+/-} = 35 \pm 6°$, $P = 0.0028$, Figure 2c). Furthermore, α inversely correlated with F_{im} ($F_{im} = -0.7(\pm 0.1)\alpha + 79.0(\pm 5.2)$, $P < 0.0001$, $R^2 = -0.57$, Figure 2d), indicating that mice with

narrower angles swam less than those with wider angles. These results indicate that the different outcomes of the FST for *Gabra5*$^{+/-}$ and WT animals are conceivably not caused by a difference in emotional/behavioral state (for example, depression or helplessness), but by physical properties that also underlie the differences in α.

The major upward force supporting an animal in water is buoyancy, which should be reflected by the floating angles during immobility. A wider α corresponds to a larger part of the body being submerged, that is, the animal is less buoyant as it needs more supporting force provided by the displaced water, and vice versa. The inverse correlation between F_{im} and α may mean that buoyancy of mice could be a confounding factor in the FST.

To investigate this potential confound, we manipulated the buoyancy of mice by altering the air trapped in their fur, a key factor for keeping them afloat in water.[26–28] Less air should be trapped in fur when reducing the surface tension of water with surfactants. Hence, soap may be used to decrease the animal's buoyancy.

A mild soap solution (1%) was gently rubbed onto the caudal areas (about 1/3 of body length) of the animals. Mice in the control group were treated similarly, but with water (0% soap solution). Soap-treated animals had significantly lower F_{im} ($F_{im\_water} = 47.4 \pm 6.0\%$ vs $F_{im\_soap} = 25.4 \pm 6.1\%$, $P = 0.0471$, Figure 2e) and larger α ($\alpha_{water} = 32 \pm 1°$ vs $\alpha_{soap} = 55 \pm 5°$, $P < 0.0001$, Figure 2f), indicating that a decrease in buoyancy increases the animals' urge to swim.

To change buoyancy during the FST, we designed a customized setup for liquid exchange (Figure 1a) and devised a customized 8-min FST protocol (Figure 1b; See Materials and Methods). At the half-time point of the customized FST, we exchanged water for either water (control) or a low concentration (0.5%) soap solution. Adding soap eliminated immobility ($F_{im\_epoch1} = 56.2 \pm 3.6\%$ vs $F_{im\_epoch2} = 0.0 \pm 0.0\%$, $P < 0.0001$, paired two-tailed *t*-test, Figure 1c) making it impossible to measure α (as previously defined; See Materials and Methods). In the mild soap solution, animals assumed a vertical body posture, completely lost their ability to float and consequently were forced to swim constantly. For continuously swimming mice, it was impossible to exactly measure α, but as all these mice were almost straight down in the water we estimated α to be 90°. Therefore, adding soap solution significantly increased α ($\alpha_{epoch1} = 28 \pm 2°$ vs $\alpha_{epoch2} = 90 \pm 0°$, $P < 0.0001$, paired two-tailed *t*-test, Figure 1d). These results support the notion that buoyancy has confounded the results of the example experiment between *Gabra5*$^{+/-}$ and WT animals described above. Or, in more general terms, it shows that buoyancy can affect the outcome of the FST.

In the FST, the latency to first immobility (t_{lat}) is also considered a key measure for quantifying the state of 'behavioral despair' of the animal.[29–33] Traditionally, t_{lat} is the delay to the first bout of immobility lasting longer than 1 s[13,33] or sometimes 2 s.[30,31] As far as we can tell, no reason is ever given why this exact threshold of 1 or 2 s has been chosen. Hence, this threshold of 1 or 2 s is entirely arbitrary, despite the fact that it can determine the final conclusion reached (see below). To address this, we started a systematic study of the durations of immobility (t_{im}) of all the mice used in the standard FST in water. We observed that different mice have very different distributions of t_{im}s (Figures 3a and b): for some (for example, Figures 3a and b; open circles), most of the stops were shorter than 1 s, whereas for others (for example, Figures 3a and b; filled circles), most of the stops were much longer than the 1 or 2 s threshold. We then analyzed the very first stops of all the mice we used for standard 6-min FSTs and observed that the cumulative probability plot of the duration of the first bouts of immobility (t_{first_im}s, Figure 3c) shows a wide distribution ($n = 57$ mice), with most t_{first_im}s longer than 1 or 2 s. The histogram of the t_{first_im} values follows a log-normal distribution (mean = 0.5 ± 0.1 log(s), s.d. = 0.4 ± 0.1 log(s), $R^2 = 0.65$, corresponding to a mean of $3.2^{\times}/_{\div}1.3$ s, Figure 3d). The wide distribution of the t_{first_im}s may indicate that all t_{im}s during a given FST in a single animal may be equally dispersed. Indeed, we found that in a given animal, the t_{im}s greatly vary during the FST (Figures 3a and e). We further discovered that the cumulative probability of the t_{im}s of a single mouse could be best fitted with the sum of two normal distributions, or in a few cases (7/68) with one normal distribution (Figure 3f; See Materials and Methods). Thus, it appears that most mice (61/68) have distinct short and long t_{im}s. To account for the highly variable t_{im}s, we propose that the threshold for screening the first critical immobility (t_c) should be objectively determined by taking into account the means and fractional contributions of the two distributions (See Materials and Methods).

To apply and test this objective method for determining t_c, we compared the effects of using different t_cs to calculate t_{lat} of WT and *Gabra5*$^{+/-}$ (Hets) mice in the standard FST (Figure 5, See Materials and Methods). Using the customary and arbitrary threshold of 1 s for all mice, there was a significant difference in the t_{lat}s between the two groups ($t_{lat\_WT} = 5.6 \pm 1.4$ s vs $t_{lat\_Hets} = 10.1 \pm 1.7$ s, $P = 0.0231$, Figure 5a). However, this significance was not there when we chose the equally arbitrary threshold of 2 s ($t_{lat\_WT} = 15.3 \pm 6.6$ s vs $t_{lat\_Hets} = 11.9 \pm 1.7$ s, $P = 0.0760$, Figure 5b). Also, the latencies of the WT mice were significantly different when calculated with the two commonly used thresholds of 1 and 2 s ($P = 0.0313$). Therefore, choosing arbitrary thresholds is utterly unreliable for calculating t_{lat}. Next, we applied our systematic and unbiased method to define the critical thresholds (t_c, See Materials and Methods). First, we used the distribution of all the t_{im}s taken from all the mice in both groups, and got a single t_c of 5.53 s for all the animals. Using this t_c, the t_{lat}s in the two groups were not significantly different ($t_{lat\_WT} = 64.3 \pm 22.2$ s vs $t_{lat\_Hets} = 23.4 \pm 2.3$ s, $P = 0.9172$, Figure 5c). Then, we calculated t_cs for each group separately ($t_{c\_WT} = 3.20$ s, $t_{c\_Hets} = 10.30$ s) by using the distribution of all the t_{im}s from each group of animals. Using these two t_cs, the t_{lat}s in the two groups became significantly different ($t_{lat\_WT} = 17.9 \pm 6.9$ s vs $t_{lat\_Hets} = 38.1 \pm 3.4$ s, $P < 0.0001$, Figure 5d). We noticed that t_{c_WT} and t_{c_Hets} have a considerably large difference, so we then wanted to statistically test whether there is a difference between the t_cs of the two groups. To do this, we used the distribution of the t_{im}s of each mouse and determined an individual t_c for each animal. We calculated the new latencies using individual t_cs, and the t_{lat}s were significantly different between the two groups ($t_{lat\_WT} = 23.5 \pm 7.8$ s vs $t_{lat\_Hets} = 39.5 \pm 4.1$ s, $P < 0.0001$, Figure 5e). Moreover, we did find a significant difference in the t_cs between the two groups ($t_{c\_individual\_WT} = 3.7 \pm 0.5$ s vs $t_{c\_individual\_Hets} = 12.6 \pm 1.6$ s, $P < 0.0001$, Figure 5f). Therefore, the new determination of t_c introduced by us can reflect important differences between the behavior of mice during the FST. Since various thresholds for both of the two groups yielded significantly different t_{lat} values ($P < 0.0001$, Friedman test, Figures 5g and h), the critical measurement of t_{lat} using objectively determined t_cs should be used to determine the differences in t_{lat}.

In the current quantification of the FST, all measured criteria (for example, F_{im} and t_{lat}) reflect the activities of the animals as single stationary values applied to the entire duration of the FST. But why not quantify FST behavior as it continuously changes during the test? Such a continuous quantification of behavior has been used before for the FST[34] in rats, using kicking frequency as a readout. We devised a continuous FST behavior plot (Figure 4a) that for a given subject marks two binary states (mobile and immobile) plotted against time (resolution = 0.1 s, top two plots, Figure 4a). The group behavior can be expressed by averaging the states of all animals at every time point, resulting in the probability of being mobile (P_{mob}) as a function of time (bottom plot, Figure 4a). The plots are from the same mice shown in Figures 2e and f. Consistent with their overall activity, mice partially treated with

soap had a higher P_{mob} throughout the test. The plots reveal that the animals started out being mobile, changing their states more frequently at first, but later becoming immobile for longer periods, resulting in a lower P_{mob}.

More thorough analysis of the P_{mob} plots revealed similar synchronous behaviors in the two groups. There was an oscillation in P_{mob} plots in both groups regardless of the treatment (Figures 4b and c), occurring at comparable times (174.2 s and 172.5 s, Figures 4b and c) after the start of the FST, with strong behavioral alternations (controls: 0.067 ± 0.004 Hz and part soap: 0.060 ± 0.004 Hz, $P = 0.263$), indicating that the animals change their mobile/immobile states with a cycle of 15 – 17 s. Notably, these analogous temporal sequences in behavior were present in both groups despite differences in their static behavioral measures (Figures 2e and f). Furthermore, the onset of this oscillatory swimming behavior must be fairly synchronous between the animals otherwise it would disappear in the averaged signal. Also, since the oscillatory behaviors start in both P_{mob} plots at around 173 s, all the animals appear to have a similar 'waiting time' before starting the stop-and-go swimming behavior.

DISCUSSION

We addressed some pitfalls in the measurements currently used for the FST in mice. First, we uncovered buoyancy as a confounding factor in the quantification of immobility, and we propose that buoyancy of mice should be quantified to account for its impact on the interpretation of the FST. Second, we devised a systematic analysis of t_{im}s in individual mice, defining an objective t_c for the calculation of t_{lat}. Last, we conceived a new analysis for the temporal profile during FST behavior. Our new findings will help obtain more quantifiable results and will provide better insights into the complex behavior patterns of mice during the FST.

According to our findings, buoyancy of mice, reflected by the measured angle α, is a confounding factor in FST. As buoyancy partly results from air trapped in the fur, it will be affected by fur characteristics that help trap air, such as the amount of surface lipids, the length of the fur and so on.[35–38] As shown here, the animals' buoyancy could be accounted for by angle measurements and should be considered when interpreting FST results as various drugs or treatments may alter the factors responsible for trapping air in the animal's fur. We have also shown a large individual variability in the t_c that defines immobility. Therefore, we propose that t_c should henceforth be objectively defined for each animal subjected to the FST as a new variable for the test. This value should then be used for an unbiased determination of the latency to immobility (t_{lat}) to uncover potential differences in behavior that would have previously gone unnoticed. Interestingly, we have discovered some distinct oscillatory patterns in the swimming behavior of mice during the FST. These results may indicate the presence of an invariant intrinsic biological clock that influences swimming patterns in mice, providing ground for further exciting investigations.

CONFLICT OF INTEREST

The authors declare no conflict of interest.

ACKNOWLEDGMENTS

This work was supported by the National Institutes of Health (NIH) grants NS030549 and MH076994, and the Coelho Endowment to IM and Scholarship No. 2011632034 from the China Scholarship Council to LC.

REFERENCES

1 Murray CJ, Lopez AD. Quantifying disability: data, methods and results. *Bull World Health Organ* 1994; **72**: 481–494.
2 Vos T, Flaxman AD, Naghavi M, Lozano R, Michaud C, Ezzati M *et al.* Years lived with disability (YLDs) for 1160 sequelae of 289 diseases and injuries 1990-2010: a systematic analysis for the Global Burden of Disease Study 2010. *Lancet* 2012; **380**: 2163–2196.
3 Murray CJL, Vos T, Lozano R, Naghavi M, Flaxman AD, Michaud C *et al.* Disability-adjusted life years (DALYs) for 291 diseases and injuries in 21 regions, 1990-2010: a systematic analysis for the Global Burden of Disease Study 2010. *Lancet* 2012; **380**: 2197–2223.
4 Whiteford Ha, Degenhardt L, Rehm J, Baxter AJ, Ferrari AJ, Erskine HE *et al.* Global burden of disease attributable to mental and substance use disorders: findings from the Global Burden of Disease Study 2010. *Lancet* 2013; **382**: 1575–1586.
5 Ferrari AJ, Somerville AJ, Baxter AJ, Norman R, Patten SB, Vos T *et al.* Global variation in the prevalence and incidence of major depressive disorder: a systematic review of the epidemiological literature. *Psychol Med* 2013; **43**: 471–481.
6 Murray C, Lopez A. Alternative projections of mortality and disability by cause 1990–2020: Global Burden of Disease Study. *Lancet* 1997; **349**: 1498–1504.
7 Cryan JF, Mombereau C. In search of a depressed mouse: utility of models for studying depression-related behavior in genetically modified mice. *Mol Psychiatry* 2004; **9**: 326–357.
8 Cryan JF, Holmes A. The ascent of mouse: advances in modelling human depression and anxiety. *Nat Rev Drug Discov* 2005; **4**: 775–790.
9 Cryan JF, Slattery DA. Animal models of mood disorders: recent developments. *Curr Opin Psychiatry* 2007; **20**: 1–7.
10 Porsolt RD, Le Pichon M, Jalfre M. Depression: a new animal model sensitive to antidepressant treatments. *Nature* 1977; **266**: 730–732.
11 Porsolt RD, Anton G, Blavet N, Jalfre M. Behavioural despair in rats: a new model sensitive to antidepressant treatments. *Eur J Pharmacol* 1978; **47**: 379–391.
12 Porsolt RD, Bertin A, Jalfre M. Behavioral despair in mice: a primary screening test for antidepressants. *Arch Int Pharmacodyn Ther* 1977; **229**: 327–336.
13 Castagné V, Moser P, Roux S, Porsolt RD. Rodent models of depression: forced swim and tail suspension behavioral despair tests in rats and mice. *Curr Protoc Pharmacol* 2010; **Chapter 5**: Unit 5.8.
14 Borsini F, Meli A. Is the forced swimming test a suitable model for revealing antidepressant activity ? *Psychopharmacology (Berl)* 1988; **94**: 147–160.
15 Cryan J, Markou A, Lucki I. Assessing antidepressant activity in rodents: recent developments and future needs. *Trends Pharmacol Sci* 2002; **6147**: 238–245.
16 West AP. Neurobehavioral studies of forced swimming: the role of learning and memory in the forced swim test. *Prog Neuropsychopharmacol Biol Psychiatry* 1990; **14**: 863–877.
17 Petit-Demouliere B, Chenu F, Bourin M. Forced swimming test in mice: a review of antidepressant activity. *Psychopharmacology (Berl)* 2005; **177**: 245–255.
18 Lucki I, Dalvi A, Mayorga A. Sensitivity to the effects of pharmacologically selective antidepressants in different strains of mice. *Psychopharmacology (Berl)* 2001; **155**: 315–322.
19 Võikar V, Kõks S, Vasar E, Rauvala H. Strain and gender differences in the behavior of mouse lines commonly used in transgenic studies. *Physiol Behav* 2001; **72**: 271–281.
20 David DJP, Renard CE, Jolliet P, Hascoët M, Bourin M. Antidepressant-like effects in various mice strains in the forced swimming test. *Psychopharmacology (Berl)* 2003; **166**: 373–382.
21 Arai I, Tsuyuki Y, Shiomoto H, Satoh M, Otomo S. Decreased body temperature dependent appearance of behavioral despair in the forced swimming test in mice. *Pharmacol Res* 2000; **42**: 171–176.
22 Taltavull JF, Chefer VI, Shippenberg TS, Kiyatkin EA. Severe brain hypothermia as a factor underlying behavioral immobility during cold-water forced swim. *Brain Res* 2003; **975**: 244–247.
23 Lucki I. The forced swimming test as a model for core and component behavioral effects of antidepressant drugs. *Behav Pharmacol* 1997; **8**: 523–532.
24 Cryan J, Lucki I. Antidepressant-like behavioral effects mediated by 5-Hydroxytryptamine(2C) receptors. *J Pharmacol Exp Ther* 2000; **295**: 1120–1126.
25 Bourin M, Fiocco AJ, Clenet F. How valuable are animal models in defining antidepressant activity? *Hum Psychopharmacol* 2001; **16**: 9–21.
26 Esher RJ, Wolfe JL, Layne JN. Swimming behavior of rice rats (Oryzomys palustris) and cotton rats (Sigmodon hispidus). *J Mammal* 1978; **59**: 551–558.
27 Fish FE. Comparison of swimming kinematics between terrestrial and semiaquatic opossums. *J Mammal* 1993; **74**: 275–284.
28 Santori RT, Vieira MV, Rocha-Barbosa O, Magnan-Neto JA, Gobbi N. Water Absorption of the Fur and Swimming Behavior of Semiaquatic and Terrestrial Oryzomine Rodents. *J. Mammal.* 2008; **89**: 1152–1161.
29 Sunal R, Gumusel B, Kayaalp SO. Effect of changes in swimming area on results of 'behavioral despair test'. *Pharmacol Biochem Behav* 1994; **49**: 891–896.
30 Koponen E, Rantamäki T, Voikar V, Saarelainen T, MacDonald E, Castrén E. Enhanced BDNF signaling is associated with an antidepressant-like behavioral response and changes in brain monoamines. *Cell Mol Neurobiol* 2005; **25**: 973–980.

31 Rantamäki T, Hendolin P, Kankaanpää A, Mijatovic J, Piepponen P, Domenici E *et al.* Pharmacologically diverse antidepressants rapidly activate brain-derived neurotrophic factor receptor TrkB and induce phospholipase-Cgamma signaling pathways in mouse brain. *Neuropsychopharmacology* 2007; **32**: 2152–2162.
32 Lutter M, Krishnan V, Russo SJ, Jung S, McClung CA, Nestler EJ. Orexin signaling mediates the antidepressant-like effect of calorie restriction. *J Neurosci* 2008; **28**: 3071–3075.
33 Castagné V, Porsolt RD, Moser P. Use of latency to immobility improves detection of antidepressant-like activity in the behavioral despair test in the mouse. *Eur J Pharmacol* 2009; **616**: 128–133.
34 Warden MR, Selimbeyoglu A, Mirzabekov JJ, Lo M, Thompson KR, Kim S-Y *et al.* A prefrontal cortex-brainstem neuronal projection that controls response to behavioural challenge. *Nature* 2012; **492**: 428–432.
35 Chen W, Kelly MA, Opitz-Araya X, Thomas RE, Low MJ, Cone RD. Exocrine gland dysfunction in MC5-R-deficient mice: Evidence for coordinated regulation of exocrine gland function by melanocortin peptides. *Cell* 1997; **91**: 789–798.
36 Chen HC, Smith SJ, Tow B, Elias PM, Farese RV. Leptin modulates the effects of acyl CoA:diacylglycerol acyltransferase deficiency on murine fur and sebaceous glands. *J Clin Invest* 2002; **109**: 175–181.
37 Westerberg R, Tvrdik P, Undén A-B, Månsson J-E, Norlén L, Jakobsson A *et al.* Role for ELOVL3 and fatty acid chain length in development of hair and skin function. *J Biol Chem* 2004; **279**: 5621–5629.
38 Lin M-H, Hsu F-F, Miner JH. Requirement of fatty acid transport protein 4 for development, maturation, and function of sebaceous glands in a mouse model of ichthyosis prematurity syndrome. *J Biol Chem* 2013; **288**: 3964–3976.